Finite Element Modeling and Vibration Simulation of a 5-MW 61.5-Meter Composite Wind Turbine Blade for Debonding Damage Inference

by

Junbo Yang

A thesis submitted in partial fulfillment of the requirements for the degree of

Master of Science

in

STRUCTURAL ENGINEERING

Department of Civil and Environmental Engineering
University of Alberta

ABSTRACT

The renewable and clean energy industry highly relies on wind turbine blades (WTBs) to generate electricity from wind. However, WTBs can suffer from a variety of damage, including spar cap-shear web debonding, which can lead to crack initiation and propagation, and in turn, cause wind turbine structural collapse. As such, this study focuses on spar cab-shear web debonding by comparing the dynamic behaviors of WTBs with and without debonding via finite element simulations, aiming to shed light on vibration-based damage detection for WTBs. Specifically, this study performed debonding and vibration simulations of the 61.5 m 5-MW blade developed by the National Renewable Energy Laboratory (NREL) in the United States. The objectives of this study are two-fold: (1) to identify the hotspot for cap-web debonding and demonstrate the crack-propagation behavior with an existing crack in the hotspot under increasing aerodynamic loads; (2) to investigate and compare the vibration behaviors of wind turbine blades with and without debonding damage (via free vibration and impact load analysis) to better inform future development of vibration-based diagnostic techniques. It is found that the cap-web connection within a 9-10.25 m span of the studied WTB is more vulnerable to debonding damage and thus determined as the debonding hotspot. The vibration simulation results indicate that the cap-web debonding is less likely to be uncovered by vibration signals, particularly via free vibration testing. However, when impact load testing is used for WTB with relatively large debonding cracks, adequate hitting points and signal collection points (i.e., near crack) can reveal the hidden damage. It is found that when the hitting point is closer to the potential debonding location, more signal discrepancy between the defective WTB and the intact WTB can be observed. Since it is possible to have debonding damage at the following 4 locations in the transverse direction, i.e., within the connection joints between the shear webs and the spar cap located at LE-BOT, LE-TOP, TE-BOT, TE-TOP (herein, LE, TE, BOT, and TOP refer to the leading edge, trailing edge, bottom surface, and top surface of the WTB, respectively), hitting points in impact load tests (e.g., flapwise on the BOT or TOP surfaces, edgewise on the LE or TE) should be located at those 4 locations in the transverse direction. In the spanwise direction, the hitting points within the debonding area, particularly around 10.25 m from the WTB root, are found to be effective for damage detection. Furthermore, the signal collection points should be as close as possible to the hitting points. Such pre-knowledge regarding the debonding hotspot, the relative effectiveness of vibrations methods, and the impact and vibration signal collection points can potentially increase the effectiveness of vibration-based detection techniques for cap-web debonding in practical applications.

ACKNOWLEDGEMENTS

I can eventually accomplish this thesis, which likely means the termination of my graduate program, but it is a new starting point for the next stage in my life. Therefore, I sincerely appreciate every single person or thing during my graduate program in this short acknowledgment.

Firstly, I want to express my sincere appreciation to my most respected supervisor Dr. Yong Li, for his significant help regarding my research. He always uses his professional knowledge, broadened perspective, and explicit logical thinking to help me overcome every obstacle. Also, he shows well-rounded solicitude for his students. The most valuable thing I learned from Dr. Li during my graduate program is his life advice from the research work and the subtle influence of his excellent personality on me. He can perceive my weaknesses and give providential suggestions, especially telling me to be down-to-earth and not to advance rashly. Moreover, he knows my character and would like to discuss his brilliant business ideas with me. I will always cherish this learning experience with Dr. Li.

My sincere gratitude also goes to my co-supervisor Dr. Samer Adeeb. I am also very grateful to all the members of Dr. Li's research group for their help, support, and encouragement, especially Bowen Zeng, whom I can say is my best friend in the research group. I will always remember how he covered me whenever I had problems, even at midnight—best wishes for his career and life in the future.

I must thank my family and friends for their tremendous understanding, unconditional support, careful and meticulous consideration, and endless love. They always give me the strength and courage to move forward. Without them, it would be impossible for me to complete my M.Sc study.

This thesis is dedicated to the younger self of two years ago. I did not waste morn than seven hundred days and nights because of me and the significant guys who traveled alongside me.

TABLE OF CONTENTS

LIST OF TABLES

LIST OF FIGURES

LIST OF ABBREVIATIONS

WTB	Wind Turbine Blade
FEM	Finite Element Method
NREL	National Renewable Energy Laboratory
CanREA	Canadian Renewable Energy Association
VAWT	Vertical Axis Wind Turbine
HAWT	Horizontal Axis Wind Turbine
UGE	Formerly Urban Green Energy
MWh	Megawatt-Hours
kWh	Kilowatt-Hours
CFD	Computational Fluid Dynamics
DTU	Technical University of Denmark
TSR	Tip Speed Ratio
BEM	Blade Element Momentum
AoA	Attack of Angle
GA	Genetic Algorithm
ANN	Artificial Neural Network
ECGA	Extended Compact Genetic Algorithm
FBG	Fiber Bragg Grating
AE	Acoustic Emission

EMD	Empirical Mode Decomposition
FFT	Fast Fourier Transformation
DNN	Deep Neural Network
HMM	Hidden Markov Model
EP	Epoxy Adhesives
PU	Polyurethane Adhesive
MMA	Methyl Methacrylate Adhesives
VE	Vinyl Ester Adhesives
ASTM	American Society for Testing and Materials
LEFM	Linear Elastic Fracture Mechanics
EPFM	Elasto-Plastic Fracture Mechanics
VCCT	Virtual Crack Closure Technique
XFEM	Extended Finite Element Method
CZM	Cohesive Zone Method
TSL	Traction Separation Law
MAXS	Maximum Nominal Stress Criterion
MAXE	Maximum Nominal Strain Criterion
QUADS	Quadratic Nominal Stress Criterion
QUADE	Quadratic Nominal Strain Criterion

BK	Benzeggagh and Kenane
DOWEC	Dutch Offshore Wind Energy Converter
SW	Shear Web
GFRP	Glass Fiber-reinforced Plastic
CFRP	Carbon Fiber-reinforced Plastic
UTS	Ultimate Tensile Strength (longitudinal direction)
UCS	Ultimate Compressive Strength (longitudinal direction)
UD	Uni-directional
LE	Leading Edge
TE	Trailing Edge
REINF	Reinforcement
CM	Center Mass
FVA	Free Vibration Analysis
ILA	Impact Load Analysis

LIST OF SYMBOLS

E	Kinetic energy
m	Air mass
v	Airspeed
$\dot{V}$	Wind volume flow rate derived from the moving air in speed v
A	The wind volume flow passing through a cross-section area
$\dot{m}$	Mass flow rate
ρ	Air density
P	Power where the mass flow passing through a specific area during a unit of time
v_1	Wind speed before the energy converter
v_2	Wind speed after the energy converter
F	The corresponding force exerted by the converter to counter the airflow thrust
v'	Air velocity present in the converter’s flow plane
c_p	Power coefficient
λ	Tip speed ratio
Ω	Rotational velocity of wind turbine blades
r	Rotor radius

V_w	Wind speed to calculate tip speed ratio
C_{opt}	Optimum chord length
n	Blade quantity
C_L	Lift coefficient
V_r	Local resultant air velocity
U	Wind speed to calculate C_{opt}
U_{wd}	Design wind speed
α_{AOA}	Attack of angle
F_L	Lift force
F_D	Drag force
F_R	Resultant force formed by F_L and F_D
Re	Reynolds number
C_D	Drag coefficient
ρ	Free stream density
U_{rel}	Relative wind velocity
c	Chord length
v_k	Kinematic viscosity

μ	Dynamic viscosity
θ	Twist angle or pitch angle
ϕ	Angle of rotor plane rotation, or relative wind angle
t/c	Thickness to chord ratio
T , $T_{\max}$	Traction, and maximum traction to initiate damage in CZM
δ_C	Maximum separation to initiate damage in CZM
G_c	Energy release rate
k_c	Cohesive stiffness
n, s, t	The normal, in-plane-shear, and out-of-plane shear (tear) directions in damage initiation criteria for CZM
ε , ε_{max}	Strain and maximum strain with a given constitutive thickness $t = 1$
G_n, G_s, G_t	The fracture energy in normal, shear and tear directions
$G_{c,n}$, $G_{c,s}$, $G_{c,t}$	The critical energy release rate in normal, shear and tear directions
α_c	The empirical coefficient in power law for CZM
η	The exponential factor in BK law for CZM
E_1, E_2	Young's modulus in the first (longitudinal) and second (transverse) material directions
G_{12}	Shear modulus
v_{12}	Poisson's ratio

t_n, t_s, t_t	Traction stress vector in the direction of the normal, in-plane shear (shear-I), and out-of-plane shear (shear-II)
F_n, F_t , M_m	The aerodynamic force normal to the rotor plane, force tangential to the rotor plane, and pitching moment (respect to the pitching axis)
ξ_i	Conversed structural damping in ABAQUS
α, β	Rayleigh damping factors
ω_i	Natural Frequencies of selected modes for damping ratio transversion

CHAPTER 1: INTRODUCTION

1.1 Introduction

Increasing energy demand to meet social and economic development has significantly contributed to greenhouse gas (GHG) emissions due to overusing and consuming fossil fuels in recent decades, contributing to the escalating severity of the global warming issue. To fight climate change, renewable energy (e.g., wind energy) has been promoted worldwide, which gives rise to the growing need for large-scale onshore or offshore wind farms and micro-wind turbines in the community. In Canada, wind energy is now the lowest-cost new power source and has been the largest renewable energy source for a decade [1], [2]. The never-ending kinetic energy stored in the wind can be converted to electric power by modern wind turbine systems with low cost and high efficiency [3]. For a modern wind turbine system, almost 15–20% of the cost of production is attributed to the blades [4], [5]. However, wind turbine blades (WTBs) are subject to variable wind-induced vibration under harsh working environments, thus, are susceptible to damage for various reasons. Blade failure is the most common root cause of the structural collapse of wind turbine systems [6].

Among various damages observed in WTBs [7]–[9], debonding is one of the most prevalent damage types, which commonly occurs at adhesive joints in wind turbine blades [10], [11], such as the spar cap-shear web or blade shell-shear web connections, and top/bottom blade skin connections at the trailing/leading edge [12]. In particular, the debonding failure at the spar cap-shear web adhesive connections is of particular concern primarily for the following two reasons. Firstly, the spar cap-shear web forms the “box” structure to reduce the unsupported length of the blade skin and provide extra strength for the entire blade structure. Debonding damage, if any, will weaken the adhesive strength and decrease the structural integrity of a wind turbine blade [13]–[15]. Secondly, debonding damage will likely lead to crack initiation and propagation at adhesive connections between the spar cap and shear webs, being the root cause of the structural collapse, as evidenced by many previous comprehensive full-scale tests. For example, Yang [16] loaded a 40 m wind turbine blade until the structural collapse, which indicated that debonding at the adhesive joints between the spar cap and shear webs was the initial damage, leading to a more extensive crack propagation to a final collapse. Similar observations were made in other studies [13], [17], [18]. Therefore, inspecting this critical type of debonding damage is significant in ensuring blades' safety and preventing unexpected disasters.

Among different damage detection technologies, the vibration method is the mainstream technique appropriate for inspecting hidden damage (e.g., delamination, spar cap-shear web debonding) on the operational WTBs, because it is relatively easy to implement and non-destructive [19]. For example, DoliNski [20] successfully used the vibrometry method and finite element simulation to localize and visualize the delamination damages inside the blade structure. Hoell [21] proposed autoregressive model coefficients as a vibration-based damage indicator to monitor the trailing edge debonding on the wind turbine blades. Ulriksen [22] used vibration analysis to extract the dynamic properties of a 34-meter blade and localize the trailing edge debonding damage by investigating the modal shapes and wavelet characteristics. However, limited studies on spar cap-shear web debonding damage [14], [16] can be found in the literature. Dynamic properties or characteristics of wind turbine blades under various health conditions (e.g., different debonding scenarios) have not been studied systematically, which undermines the effectiveness of vibration-based blade diagnosis (e.g., free vibration, hammer impact testing) to some extent.

1.2 Research questions

This paper revolves around the debonding problem of the wind turbine blade, mainly aiming to answer the following two questions:

(1) Where is the wind turbine blade's most critical region for the cap-web debonding? How will an existing crack in this critical region propagate?

(2) Is free vibration or impact load testing technique effective for cap-web debonding monitoring? How to select the signal collection points for sensor installation and the impact load points to improve the efficiency of vibration-based techniques for debonding inference and contribute to the practical inspections?

1.3 Research objective and methodology

This study aims to shed light on vibration-based damage detection for WTBs, with particular attention paid to the testing methods (e.g., free vibration and impact load testing) and the signal collection (or sensor installation), which is the root cause of cost-effectiveness and monitoring efficiency.

To accomplish this goal, this study will perform finite element-based debonding and vibration simulations on the NREL 61.5 m 5-MW blade, to better understand the vibration behaviors of the composite wind turbine blade with and without debonding damage. Such knowledge will be used to guide the development of vibration-based diagnostic techniques for effective debonding detection and severity assessment of wind turbine blades. To be specific, the objectives of this study are two-fold: (1) to identify the hotspot for cap-web debonding and demonstrate the crack-propagation behavior with an existing crack in the hotspot under increasing aerodynamic loads; (2) to investigate and compare the vibration behaviors of wind turbine blades with and without debonding damage (via free vibration and impact load analysis) to inform the development of vibration-based diagnostic techniques. The pre-knowledge includes the debonding hotspots, the relative effectiveness of vibrations methods, and the impact and vibration collection points and directions, which can potentially increase the effectiveness in practical applications to infer cap-web debonding damage (e.g., reducing unnecessary sensor placement) [19].

1.4 Organization of thesis

This thesis is divided into six chapters as follows (see Figure 1.1). Following the introduction in CHAPTER #1, CHAPTER #2 presents a comprehensive literature review by introducing relevant aspects ranging from the background of wind energy to the fundamental concept and analysis methods of debonding in WTBs. A reliable blade model is necessary to investigate WTB with debonding further. Therefore, a finite element model of the 5-MW blade provided by NREL (National Renewable Energy Laboratory in the United States) is rebuilt in ABAQUS, as detailed in CHAPTER #3. In CHAPTER #4, aerodynamic loads are applied to the blade to find the most critical regions (hotspots) vulnerable to cap-web debonding and determine how a pre-existing crack in this region will propagate. Finally, in CHAPTER #5, free vibration and impact load testing are simulated to evaluate the dynamic responses of the 5-MW blade under different debonding conditions, aiming to increase the knowledge, which can potentially inform the development of vibration-based diagnostic techniques for effective debonding detection and severity assessment of wind turbine blades. In the end, the thesis is concluded with conclusions and discussions about limitations for future research.

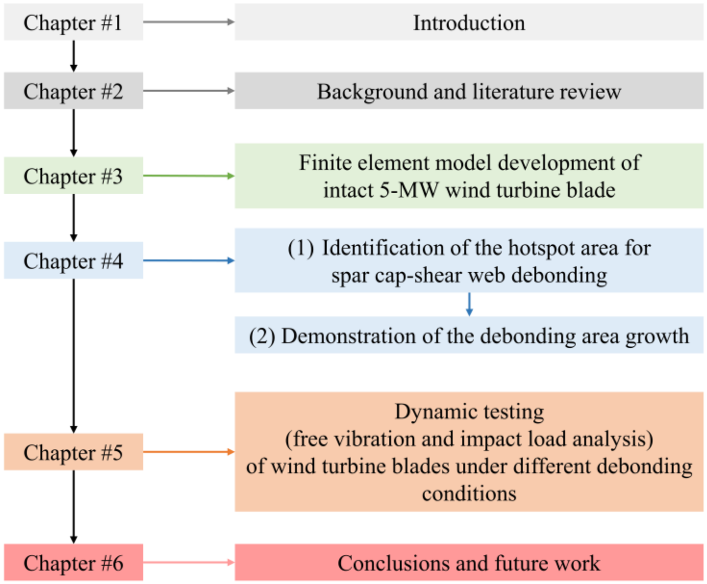

Figure 1-1: Organization of the thesis

CHAPTER 2: LITERATURE REVIEW

2.1 Introduction

The main task of this thesis is to study the dynamics of a wind turbine blade with and without spar cap-shear web debonding damage to inform damage detection based on dynamic-based techniques, including free vibration and impact load testing. Therefore, in CHAPTER #2, it is necessary to introduce the research background of wind energy and review relevant aspects related to the research work conducted in this thesis.

2.2 Background and fundamentals of wind turbines

2.2.1 Wind energy significance

The overuse and consumption of fossil fuels in recent decades have contributed to the escalating severity of the global warming issue. As a clean, carbon-free substitute for conventional power generation, wind energy has been widely utilized by energy-short countries worldwide. In Canada, wind energy is now the lowest-cost new power source and has been the largest renewable energy source for a decade [1], [2]. In eight states in the US, wind energy now accounts for 25% of the electricity generated [23]. In 2021, wind energy coupled with solar energy, for the first time, produced a record ten percent of the world's electricity [24].

The never-ending kinetic energy stored in the wind will be converted to electric power by wind turbine systems or other energy transformation machines. Wind energy has gradually occupied the leading position in the renewable energy industry by taking advantage of its economic, unlimited, and environmentally benign qualities. Perry [25] proposed that wind energy is a well-established technology with the most expansion growth and promising commercial development among all renewable energy. The development of wind energy also provides solid economic returns. Susan [26] used a professional economic model to conclude that the wind energy project would increase a country's economic activity.

On a more authoritative scale, the US Department of Energy [3] admits that wind power is cost-effective and is a stable supplement for an extended period. Wind energy's price has significantly decreased over the past ten years. It was cost-competitive compared to the United States solar energy and natural gas. More importantly, it will present many employment opportunities as an emerging industry. According to the Wind Vision Report [27], more than 600,000 jobs will be available by 2050, including jobs in basic manufacturing and maintenance and those held by persons qualified to research wind power. The paradox of social employment might potentially be partially resolved. A nation may also become energy independent and reduce the reliance on energy imports, like bulk oil, with the growth of renewable energy. Renewable energy will be the predominant power supplement in the future. CanREA (Canadian Renewable Energy Association) proposed that wind energy would be a significant booster for achieving net-zero greenhouse gas emissions by 2050 [28].

2.2.2 Wind energy development

The wind blows the propeller-like blades on the turbine rotor, which then spins the generator to export electricity. This wind-power extraction technology has developed over thousands of years. Initially, in the 1st century, the ancients invented windmills and windwheels to power machines. They assembled the original power-conversion machines from wood and cloth covers. During that underdevelopment period, wind wheels gave people significant efficiency in grinding corn and pumping water [29].

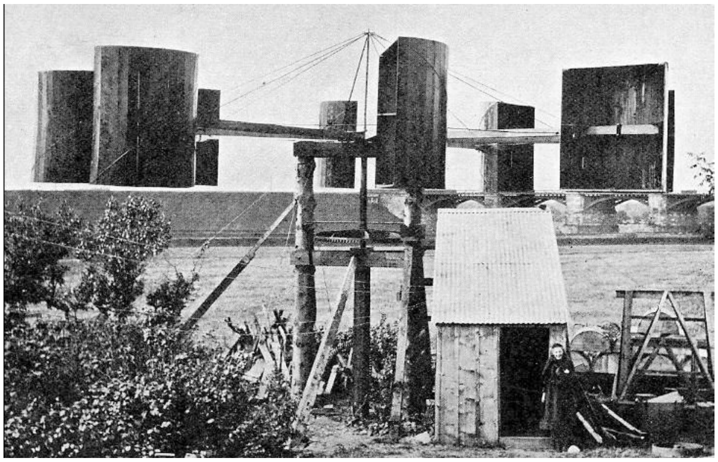

Figure 2-1: The first wind turbine by Blyth [30]

In 1887, Prof. James Blyth [30] created the first wind turbine, which was considered a turning point in wind power development. It was a vertical axis wind turbine (VAWT), as shown in Figure

2-1. This 10-meter-high, cloth cover wind turbine could generate excessive power to illuminate the town’s main street.

One year later, Charles Brush [31] created another wind power system in the US for electricity supplement (Figure 2-2 (a)). In the following decades, many windmills were constructed for mechanical or electrical purposes. Despite these small machines having a limited power generating range, with a maximum of 25 kW, they promote wind energy development to a higher level. In 1941, the first over 1-MW wind turbine (Figure 2-2 (b)) was built by P. Putnam in Vermont [32]. His significant progress in power generation contributed to abundant electrocortical supplements for the local grid.

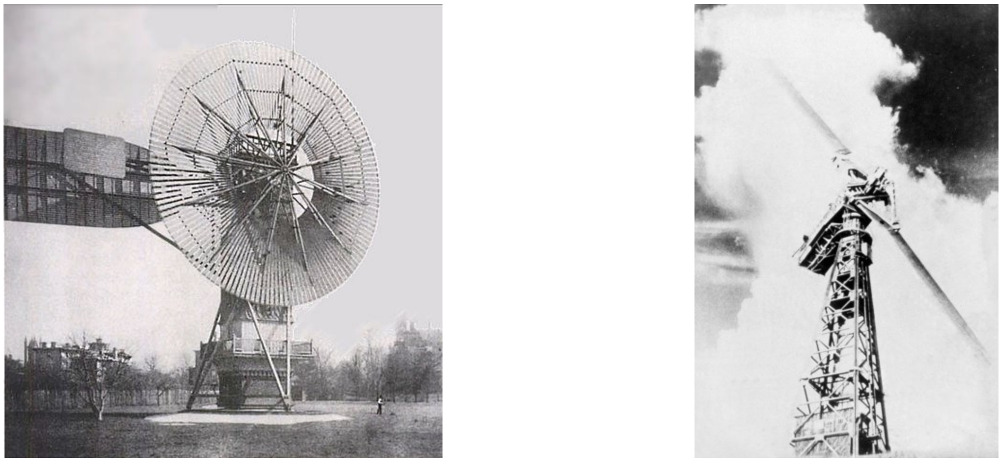

(a) Bruth’s wind turbine in 1888 [31] (b) Smith-Putnam wind turbine [32]

Figure 2-2: Two marked wind turbines

Another evolutive tendency was the number of blades. In 1957, Johannes built a horizontal axis wind turbine (HAWT) with a 24-meter diameter and three blades [33], the same as blade design in today’s wind power industry (e.g., Figure 2-3). After a long time of practice and lessons learned, three was the most optimized number of blades for a modern wind turbine, which could balance the power-generated efficiency and construction costs.

Figure 2-3: Modern 3-blade wind turbine [34]

After decades of wind energy development, natural wind feeding and standalone wind turbine tower cannot fulfill the increasing electrical demand. Therefore, researchers developed wind farms to pursue a more effective and more significant amount of energy generation. In 1975, over 4,000 homes benefited from the first wind farm built in the US and embraced enough electricity provided. From 1980 to 2000, many wind farms were constructed in the US and worldwide, contributing to the increase in wind power generation. By the end of 2000, these nations had the following installed wind power capacity: Portugal had 111 MW, Austria had 69 MW, France had 63 MW, and Finland had 39 MW [35]. Due to the rising number of wind farms, the worldwide wind power capacity has reached 17,400 megawatts.

Due to energy scarcity and global warming, the idea of renewable energy gained traction among national leaders in the 21st century. Throughout the first 20 years of the 21st century, wind power has developed fastest as a widely used type of renewable energy (Figure 2-4) [36]. The horizontal axis wind turbine (HAWT) is the most prevalent type of modern wind turbine and tends to be standardized, with three blades.

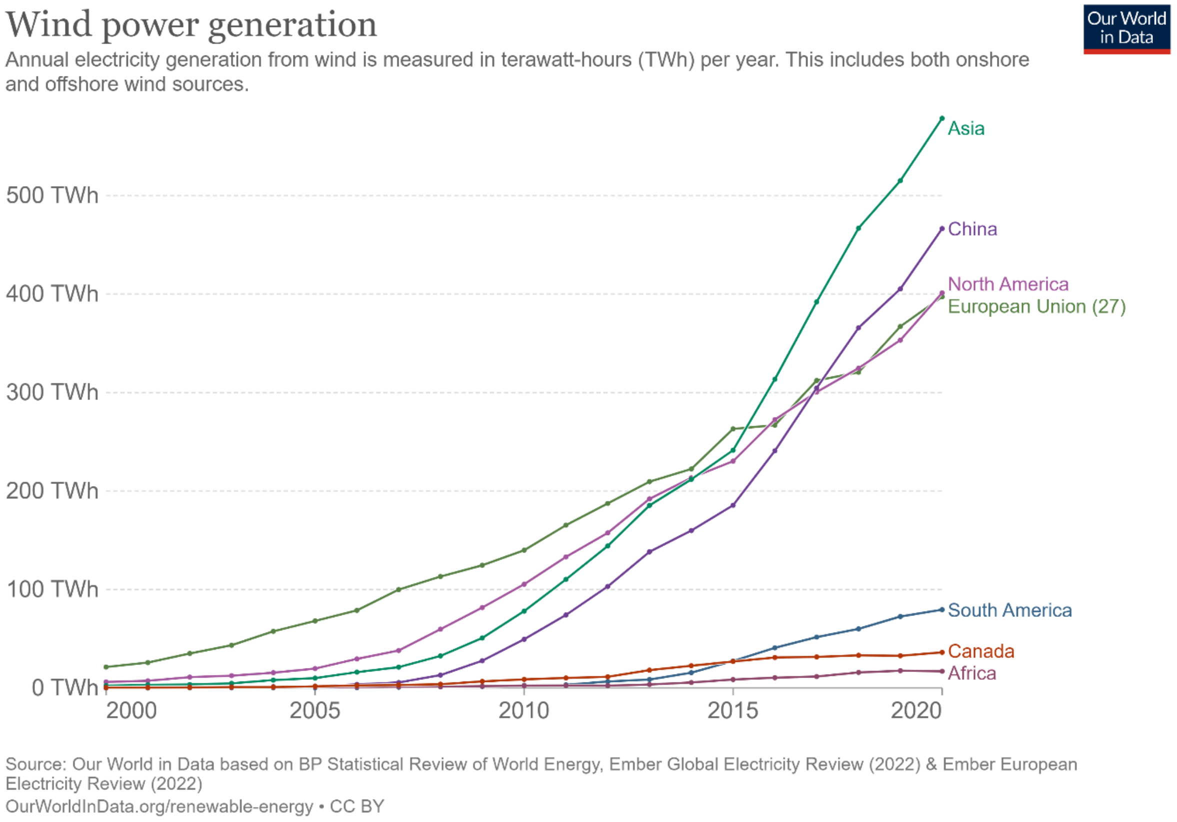

Source: Our World in Data based on BP Statistical Review of World Energy, Ember Global Electricity Review (2022) & Ember European Electricity Review (2022)
OurWorldInData.org/renewable-energy • CC BY

Figure 2-4: The development of wind power generation from 2020 to 2021 [36]

This increasing trend of wind energy development significantly reduces wind power costs. In 2013, in the United States, the median Levelized cost of wind energy was $0.06/kWh, only 15% of what it was in the 1980s [33]. As a result of precipitation over the last century, the onshore wind power generating technology has matured and expanded into the offshore wind farm industry.

The efficiency of wind power collection mainly depends on the geographical location and wind resources. The limited wind resource restricts the onshore wind turbine size, degrading the return on investment. Maximum estimates of 3 to 4-MW turbines are appropriate for the onshore wind turbine [37]. Nevertheless, the offshores' size could be over 10-MW and 200 meters high at resourceful wind farms. Additionally, offshore wind turbines have limitless ocean space, making their wind farms superior to inland turbines constrained by various topographic features. As expected by Philipp [38] from the National Renewable Energy Laboratory (NREL), offshore wind plants would domain the wind energy industry and achieve a significantly larger size, with 1,100

MW for fixed-bottom and 600 MW for floating by 2035 (Figure 2-5). These satisfied designs could provide a promising cost of energy reduction levels of 27% (onshore) and 17% - 35% (floating and fixed-bottom offshore). By 2050, according to the Wind Vision Report [27], well-developed wind power could provide a nation with a domestic energy supply chain. Wind power also has a bright foreground to develop, leading other renewables to achieve a primary objective: net-zero emissions in the coming decades.

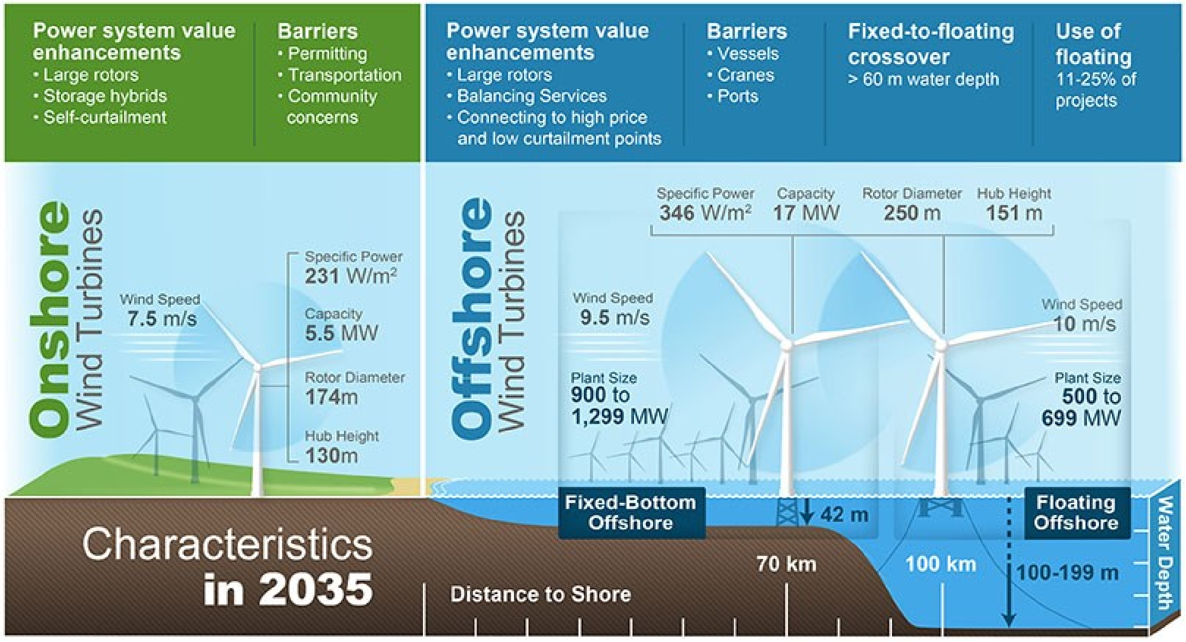

Figure 2-5: Onshore and offshore wind turbine comparison in 2035 [39]

2.2.3 Principles of wind energy conversion

It is helpful to have a fundamental grasp of the physical characteristics of wind energy and how to evaluate wind resource availability before discussing the possibilities for wind turbine systems. The basic concept of wind-electricity generation is to extract the kinetic energy from the moving air, then convert it into mechanical energy. Likewise other energy transformations, this physical phenomenon must also obey its rules.

Alberta Betz [40] proposed the “Momentum Theory” in 1919, which was the widely approbated principle of wind energy conversion. He extracted energy from the air stream using the “actuator disk" and concluded the relationship between mass and momentum in the moving wind. According to Betz's Law, the turbine can only extract up to 16/27 (almost 0.593) of the kinetic energy from the wind. This numerical value is often called Betz's coefficient or Betz's limit. Nevertheless, the energy conversion rate only achieves 70%-80% of this Betz's limit in practical utilization [41]. Even though the energy conversion limitation is insurmountable, "Momentum Theory"-respecting wind turbines gives humanity significant progress and limitless wind energy. Therefore, to provide a better basis for readers, the derivation of "Betz's Elementary Momentum Theory" is briefly presented below.

The kinetic energy in the air stream can be expressed by:

$$E=\frac{1}{2}mv^2 \qquad \text{(Eq. 2-1)}$$

Where E is the kinetic energy ($\mathrm{kg}\cdot\mathrm{m}^2/\mathrm{s}^2$ or joules), m is the air mass (kg), v is the airspeed (m/s)

First, the wind volume flow rate $\dot{V}$ can be derived from the moving air in speed v, passing through a cross-section area A.

$$\dot{V}=vA \ (\mathrm{m^3/s}) \qquad \text{(Eq. 2-2)}$$

The mass flow rate $\dot{m}$ with air density ρ is:

$$\dot{m}=\rho vA \ (\mathrm{kg/s}) \qquad \text{(Eq. 2-3)}$$

Therefore, kinetic energy can be represented by the mass flow passing through a specific area during a unit of time. Physically, the energy amount per unit of time is the power P :

$$P=\frac{1}{2}\rho v^3 A \ (\mathrm{W}) \qquad \text{(Eq. 2-4)}$$

The above equation represents how much mechanical energy the wind converters can extract from the airflow. The power can be regarded as a function of the cubic wind speed. In this instance, the most critical consideration for placing wind turbines is the correlation between mechanical power generation and wind speed.

Figure 2-6 shows the airflow in front of and behind the wind converter. The procedure can be expressed as follows:

$$P = \frac{1}{2}\rho A_1 v_1^3 - \frac{1}{2}\rho A_2 v_2^3 = \frac{1}{2}\rho(A_1 v_1^3 - A_2 v_2^3) \text{ (W)} \qquad \text{(Eq. 2-5)}$$

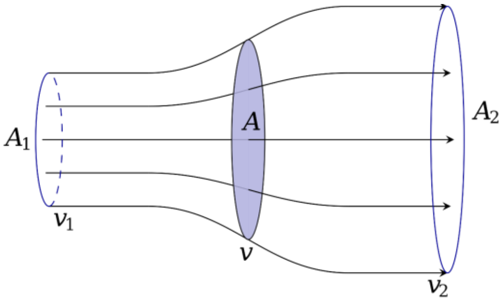

Figure 2-6: Wind flow through a converter [40]

Because the energy loss is unavoidable during kinetic-to-mechanical transformation, thus, the wind speed must decrease while the mass flow keeps unchanged. The cross-section widens as the airflow reaches the converters' plane because of the airflow's reduced velocity and constant mass flow.

To maintain the mass flow's continuity:

$$\rho v_1 A_1 = \rho v_2 A_2 \text{ (kg/s)} \qquad \text{(Eq. 2-6)}$$

Get back to the power function:

$$P = \frac{1}{2}\dot{m}(v_1^2 - v_2^2) = \frac{1}{2}\rho v_1 A_1 (v_1^2 - v_2^2) \qquad \text{(Eq. 2-7)}$$

Assuming that the mass is immutable, the airflow velocity determines the extracting power. To pursue maximum power, the wind speed after the converter v_2 has to be zero. Meanwhile, the outflow in zero velocity means the converter is inactive, so the wind speed before the machine is also zero. To better build the relationship between the airflow velocity and power extraction efficiency, presume a certain numerical ratio v_2/v_1 while deriving the energy equation.

The law of momentum conservation contributes that,

$$F = \dot{m}(v_1 - v_2) \quad \text{(N)} \qquad \text{(Eq. 2-8)}$$

The push must be countered by the converter exerting a corresponding force on the airflow by the "action equals reaction" principle. In this sense, the thrust pushes the air mass at the air velocity v' in the converter's flow plane.

$$P = Fv' = \dot{m}(v_1 - v_2)v' \quad \text{(W)} \qquad \text{(Eq. 2-9)}$$

The amount of energy and power are different while located before or after the converter. Thus, the mechanical power generated by the airflow can be derived from the following:

$$\frac{1}{2}\dot{m}(v_1^2 - v_2^2) = \dot{m}(v_1 - v_2)v' \quad \text{(W)} \qquad \text{(Eq. 2-10)}$$

$$v' = \frac{1}{2}(v_1 - v_2) = \frac{v_1 + v_2}{2} \quad \text{(m/s)} \qquad \text{(Eq. 2-11)}$$

Thus, the airflow velocity v' can be represented by v_1 and v_2 on a mathematical scale. The mass flow can be expressed as:

$$\dot{m} = \rho A v' = \frac{1}{2}\rho A(v_1 + v_2) \quad \text{(kg/s)} \qquad \text{(Eq. 2-12)}$$

Therefore, the output power after the converter is:

$$P = \frac{1}{4}\rho A(v_1^2 - v_2^2)(v_1 + v_2) \quad \text{(W)} \qquad \text{(Eq. 2-13)}$$

The above equations are based on the theoretical derivation of energy conversion principles, so introducing the formula below is necessary to compare with real wind power. The free-air stream power of the undisturbed air stream that passes through the same cross-section A is defined as follows.

$$P_0 = \frac{1}{2}\rho v_1^3 A \quad \text{(W)} \qquad \text{(Eq. 2-14)}$$

The "power coefficient" c_p is the ratio of the mechanical power extracted by the converter to that of the undisturbed air stream.

$$c_P = \frac{P}{P_0} = \frac{\frac{1}{4}\rho A(v_1^2 - v_2^2)(v_1 + v_2)}{\frac{1}{2}\rho A v_1^3} \qquad \text{(Eq. 2-15)}$$

Simplify the power coefficient representation to make the velocity ratio v_2/v_1 as the specific unique value in the function.

$$c_P = \frac{P}{P_0} = \frac{1}{2}\left[1\text{-}\left(\frac{v_2}{v_1}\right)^2\right]\left[1 + \frac{v_2}{v_1}\right] \qquad \text{(Eq. 2-16)}$$

In order to understand the interrelationship between the power coefficient and flow velocity ratio, this function can be plotted graphically. There is a maximum value for power conversion efficiency when $v_2/v_1 = \frac{1}{3}$ the power coefficient c_p reaches the maximum: $c_p = \frac{16}{27} = 0.593$. Betz first put forward this critical value, frequently named "Betz Factor" or "Betz Limit." In the ideal scenario, under the Betz limit, when $v_2/v_1 = \frac{1}{3}$ the flow velocity $v' = \frac{2}{3}v_1$.

Namely, the reduced velocity after the converter is:

$$v_2 = \frac{1}{3}v_1 \qquad \text{(Eq. 2-17)}$$

The relationship between airflow velocity and power extract productivity is evident. In practical wind turbine operation cases, the power coefficient c_p is always lower than the Betz value due to unideal conditions. On the other hand, even if the input airflow is ideal and free-stream, and converters reach a zero-loss energy conversion, only approximately 60% (0.593) of wind energy could be extracted to mechanical power, as depicted in Figure 2-7 [42], the maximum c_p is close to 0.5.

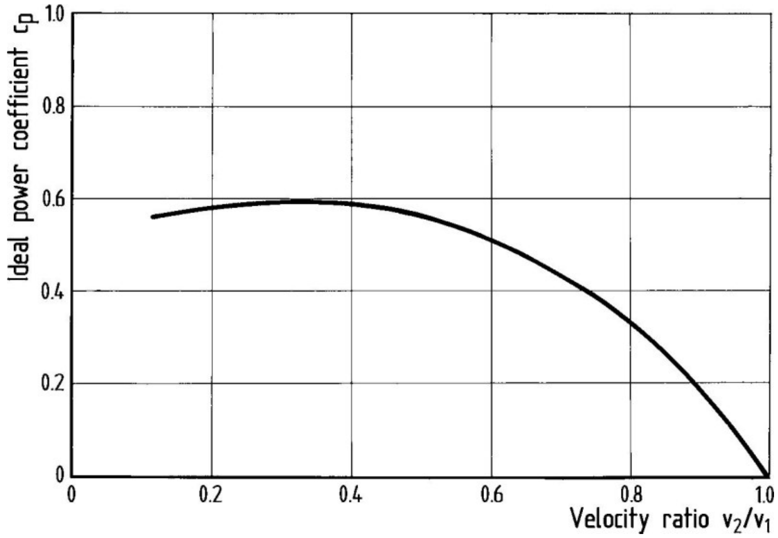

Figure 2-7: Power coefficient versus the airflow velocity ratio before and after the energy converter [42]

2.2.4 Wind energy systems

Windy airflow is produced by the sun's uneven heating of the Earth's surface. Moreover, wind energy systems include different power generators, such as a windmill, wind chargers, wind turbines, or associated facilities, which can convert the kinetic energy in the wind to electrical power. Due to the wind turbine systems' high economic applicability and satisfied power-generated capability, they gradually became the most dominant type in the wind energy industry. As a result, while presenting contemporary wind energy, wind turbine systems would serve as the primary representation. The eliminated wind machines, such as windmills, would be picturesque locations to recognize the forefathers' efforts in producing wind power. The following literature review will concentrate on the power generation process of wind turbine systems.

2.2.4.1 Wind turbine systems

The primary elements in typical wind-to-electricity systems comprise a rotor with turbine blades, a gearbox, an electric generator, a power electronic converter, and a transformer. The energy generation technological procedure from unrestricted airflow to the electrical grid is sketched in Figure 2-8 [43]. When wind flows across a blade, air pressure drops on one side of the blade. The pressure difference between the two surfaces of the blade produces both lift and drag. The lift force is greater than the drag force, causing the rotor to spin. The rotor can be connected to the generator directly or through a shaft and gearboxes to speed up the spinning and permit a physically smaller generator. This conversion of aerodynamic force to generator rotation creates direct current electricity, then is converted to alternating current and through a transformer passing to the power grid and end users.

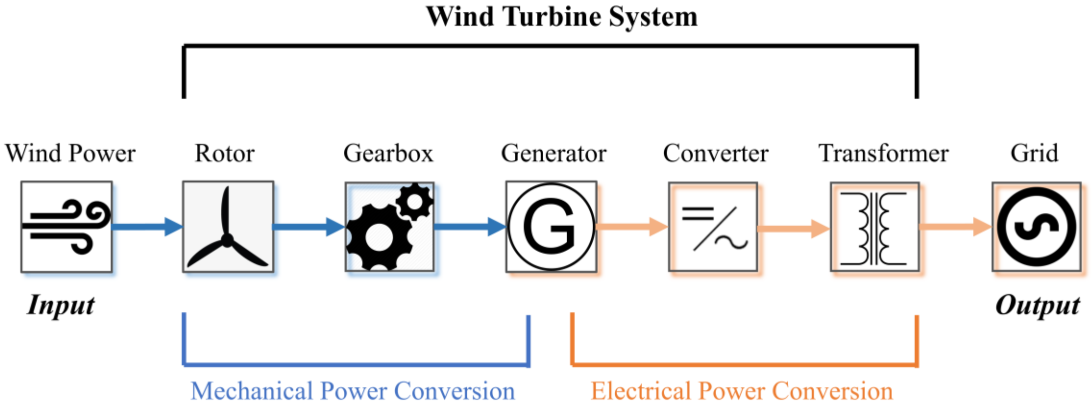

Figure 2-8: Electric generation procedure in wind turbine systems [43]

2.2.4.2 *Wind turbine categories*

The wind turbine can be classified mainly by the orientation of the shaft and rotating axis. As seen in Figure 2-9, the shaft of a vertical axis wind turbine (VAWT) is perpendicular to the ground, while the horizontal wind turbine (HAWT) has a horizontal shaft parallel to the ground. These two types have different rotor designs and offer distinct benefits [44]. The detailed explanations of the two mainstream types of wind turbine systems are as follows.

Horizontal axis wind turbine

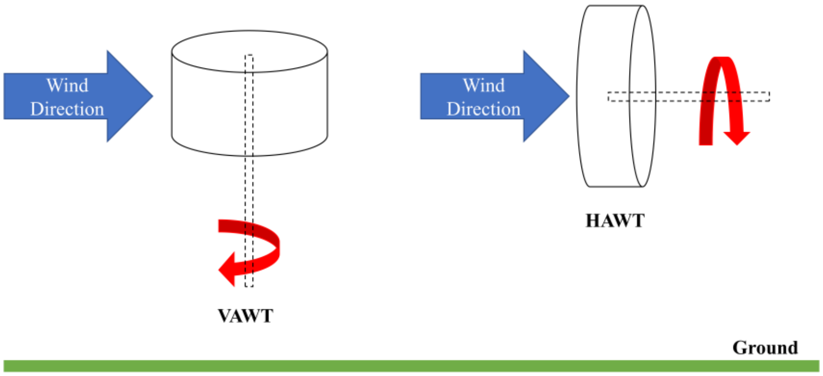

Figure 2-9: The shaft of VAWT and HAWT [45]

HAWT (Figure 2-10) is the most prevalent turbine design in the modern wind industry due to its high efficiency with lower installation and maintenance costs [46]. The main components of a horizontal axis wind turbine (HAWT) are a tower and a nacelle, depicted in Figure 2-11. The nacelle contains the rotor shaft, power take-off system, electrical generating equipment, and electrical control sub-systems. Attached to the nacelle are the hub and aerodynamic blades, as well as a pitch mechanism that ensures effective energy extraction at varying wind speeds and protects the blades under unfavorable wind conditions. A yaw mechanism is implemented to accurately orient the nacelle to align the rotor blades in the direction of the incoming wind [47]. The yaw system is positioned between the tower and the nacelle, producing a rotatable link allowing a complete 360-degree rotation of the HAWTs' active components.

Figure 2-10: Modern onsite horizontal axis wind turbines [48]

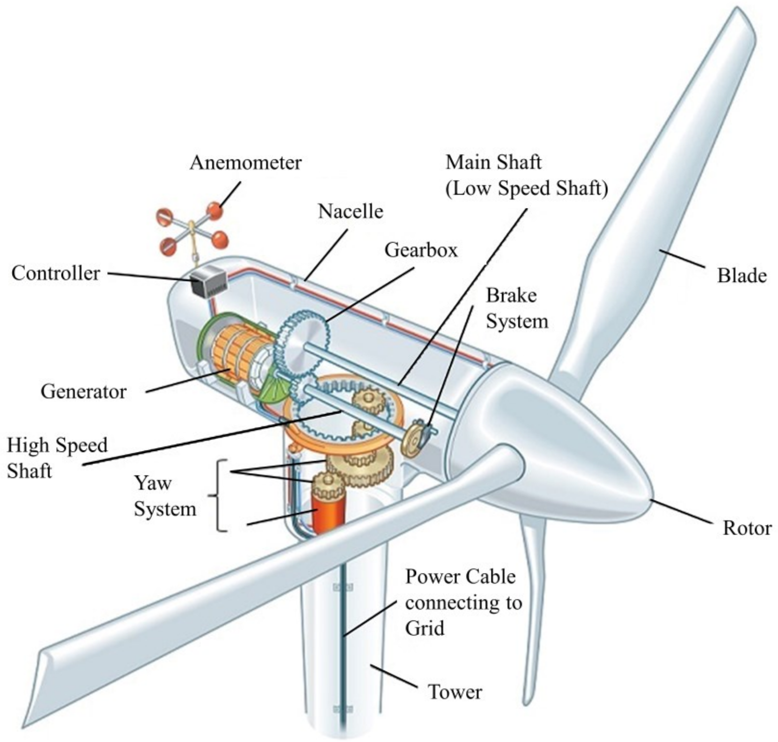

Figure 2-11: Components of a horizontal axis wind turbine [49]

HAWTs can be installed upwind or downwind (Figure 2-12), where the market is currently dominated by upwind rotors, whose rotors are situated in front of the tower [50]. The upwind design provides more power-generated efficiency owing to the lower tower influence on wind inducted at the working portion. In contrast to upwind turbines, downwind turbines suffer a distinct intake wind profile due to establishing a boundary layer on a nacelle and waking in the aerodynamic trail behind the mast. The rotor is located on the rear side of downwind turbines, the lee side of the tower. A downwind machine may be made more effectively and with less weight than an upwind machine. However, downwind turbines typically have a poorer aerodynamic efficiency, and the variation in wind power caused by the rotor going under the wind shadow of the tower may result in more significant fatigue stresses on the turbine than upwind turbines [46]. While determining the blade number of HAWTs, 99% use the standard three-bladed design, with the remaining 1% using one or two-bladed arrangements [41].

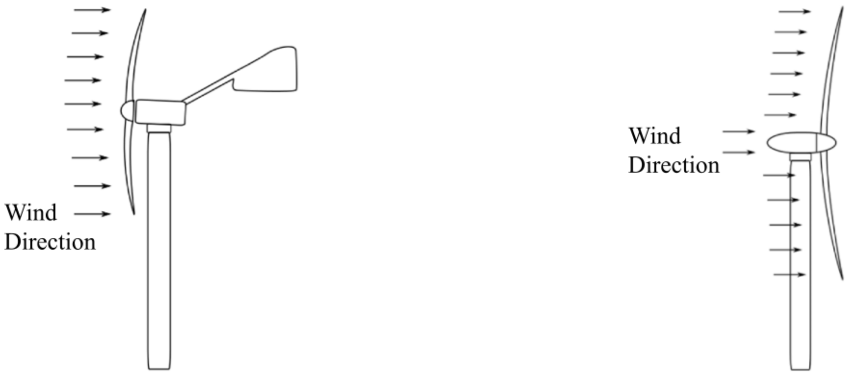

(a) Upwind (b) Downwind

Figure 2-12: Upwind and downwind HAWTs

Vertical axis wind turbine

Vertical axis wind turbines (VAWTs) typically consist of a rotor shaft that is usually vertical and transverse to the direction of the wind, ascending a tower to a hub with blades revolving around the center hub point. The power take-off, generator, and electrical components of VAWTs are located at the ground base. In contrast, the control nacelle of HAWTs is located at the tower's summit. As shown in Figure 2-13 and Figure 2-14, VAWTs can be typically divided into Savonius and Darrieus turbines regarding the rotor configuration [51], and the Darrieus turbine is similar in appearance to an “egg-beater.” It has evolved into several other types, like H-Darrieus and Helix shapes [52], [53]. Compared with Savonius turbines, Darrieus turbines are more efficient in high rotational velocity but with lower starting torque; therefore, some experts have developed turbines to combine the Savonius and Darrieus to exploit their advantages in wind power generation [54].

The primary benefits of VAWTs are mainly three-fold: (1) removing a mechanical yaw system - since it gathers wind energy from any direction - a smaller mass distribution, and (2) the capacity to harness lower wind speeds. Another advantage of VAWTs is operational flexibility because VAWTs can work regardless of wind direction, which is a significant benefit for urban applications where wind direction can quickly vary [55]. Therefore, the potential power capacity of VAWTs might be used to a greater degree than that of HAWTs when building wind turbine systems at variable wind farms. For example, the offshore wind farm has more significant benefits for

VAWTs owing to the more consistent wind profile and lower friction coefficients on the ocean surfaces [56].

On the other side, VAWTs need more material and bigger sizes to get the same amount of energy as HAWTs. They are also less reliable because the long interval span between the top and root of rotor blades means that the wind load varies significantly along the length of the blade, which increases the likelihood of material fatigue.

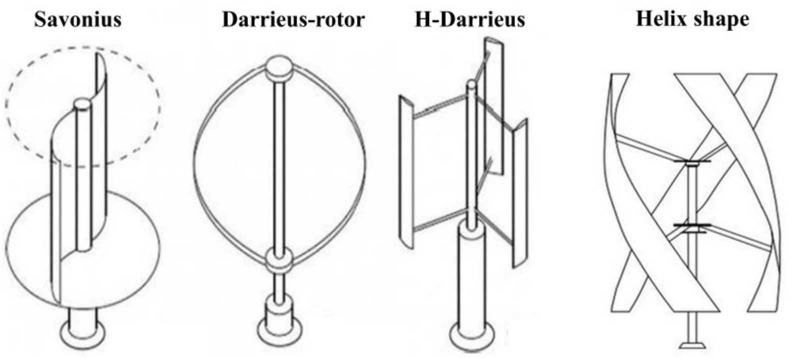

Figure 2-13: Types of VAWTs [51]

(a) Vertical Axis Micro Wind Turbines from UGE [57]

(b) The world's tallest vertical-axis wind turbine, in Cap-Chat, Quebec [58]

Figure 2-14: Two modern VAWTs

2.2.4.3 Wind turbine locations and wind farms

Selecting the wind turbine plant location should consider the summit of smooth, rounded hills, broad plains and bodies of water, and mountain gaps that concentrate and magnify wind. Wind resources are typically more beneficial for energy production at higher altitudes. The optimal site for wind turbines is where the average annual wind speed is at least 9 miles per hour (mph) — or 4 meters per second (m/s) [59], [60]. A wind turbine is a single unit, but a wind farm (Figure 2-15), also called a wind power plant or wind park, is a group of wind turbines in an operational location to generate electricity [61]. Wind farms vary in scale from a few turbines to several hundred over a vast windy region, which might be located inland or offshore.

Based on where the power machine is installed, and the type of grid connection, wind turbines could generally be categorized into three kinds, land-based (onshore) wind turbines, offshore wind turbines, and distributed wind turbines. The land-based (onshore) wind turbines are geo-restricted and prefer to be erected in rural and less-populated areas to avoid wind interruption caused by surrounding buildings. Moreover, the loud noise of running machines is unacceptable to neighborhood residents. However, the benefit is that the cost of installation and maintenance is much cheaper than an offshore wind farm. While there is no obstacle to stopping the airflow on the coastline and sea surface, the wind speed is much higher, as indicated in red in Figure 2-16 [62], and more consistent than the inland regions. Thus, offshore wind is considered more efficient and generates higher electrical delivery. However, due to the vast wind machines installed at the ground under sea level, the initial investment and construction cost are considerably more expensive than distributing a corresponding wind farm inland. Furthermore, the marine wind speed is much higher than onshore, which makes it more possible to cause fatigue failure on the wind turbine blade. The difficult accessibility to the wind turbine leads to extra maintenance costs. Nevertheless, in the end, higher payments likely represent better power generation in the wind industry. The distributed wind turbine is the third type, which refers to placing wind turbines of any size on the "customer" side of the electric meter or on the premises of the location where the energy they generate will be consumed. The comparison of onshore and offshore wind turbines is summarized in Table 2-1, including the power generation features, investment, and other operational conditions.

(a) (b)

Figure 2-15: Two types of wind farms: (a) Onshore wind farm [63], (b) Offshore wind farm [64]

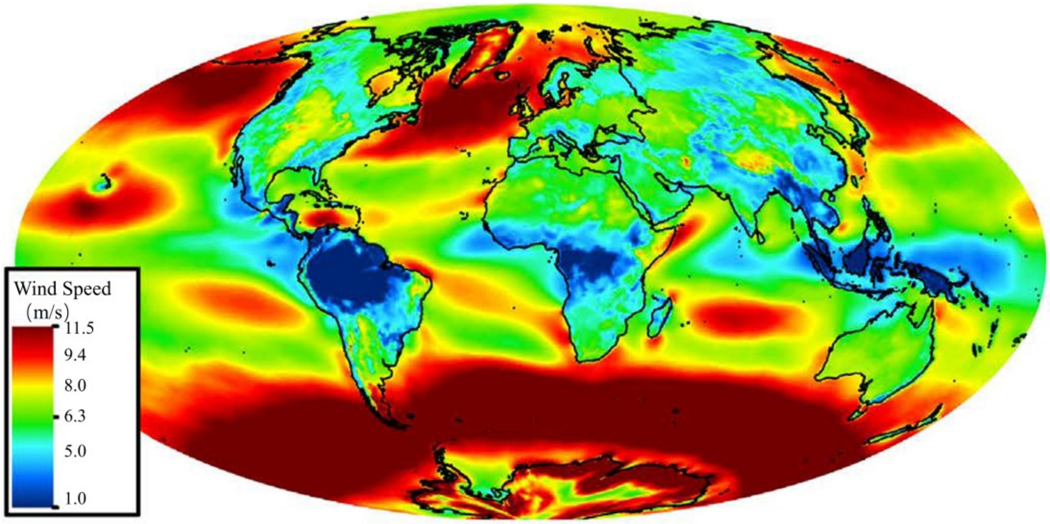

Figure 2-16: Wind speed distribution map for oceans and continents [62]

Table 2-1: Comparison of onshore and offshore wind turbines

Term	Onshore wind turbines	Offshore wind turbines
Cost	Lower	Higher
Efficient	Lower	Higher
Power generation	Less	More
Installation and maintenance	Easy, quick	Hard, expensive
Wind condition	Various, no wind or intermittent	High wind speed, persistent
Installation site	Geographic restrictions	More Space to construct

2.2.4.4 Wind turbine scale and development

While describing the power generation ability of a wind turbine, nameplate capacity or rated capacity is primarily used, which is the highest amount of electricity a wind turbine can produce. It is the rated output or peak production at a specific (typically high) wind speed per hour, measured in megawatt-hours (MWh) or kilowatt-hours (kWh). Generally, higher power capacity needs a larger blade mounted on the top tower to capture more airflow kinetic. Therefore, manufacturers also use hub height and rotor diameter to scale a wind turbine. Furthermore, the decreasing "specific power" helps the manufacturers to balance the high power generation demand and wind turbine magnitude limitation.

Nameplate capacity

Small wind turbines with less than 10 kW in power generation are ideal for use in homes, farms, and remote applications, while intermediate wind turbines ranging from 10 kW to 250 kW are beneficial for use in villages, hybrid systems, and distributed electricity [65], [66]. But for commercial electrical generation, the individual size and power rating of a modern wind turbine are consistently pursuing higher and larger to reduce the cost of energy per produced kilowatt-hour [67]. The leading wind turbine manufacturers have released 4–8 MW products [68], [69], and some large offshore turbines could be over 10 MW. By the end of January 2022, the largest and most potent GE Haliade-Xwind turbine with 14 MW was ordered, even though at the prototype stage [70]. Also, a 16 MW wind turbine concept provided by Mingyang Wind Power [71] endeavors to be the largest offshore wind turbine by 2024. The trend of increasing wind turbine size is still advancing, in the coming years; the average wind turbine capacity is promising over 10 MW, and estimated to be up to 20 MW before 2035 [72].

Hub height & rotor diameter

For horizontal axis wind turbines, the hub height is the distance from the installed ground to the center of the hub mounted on the turbine tower. Since wind velocity is generally increased by altitude climbing in specific wind farms, turbine manufacturers are inclined to produce taller towers to capture more airflow energy. The rotor diameter of a turbine is the length of the circle swept by the revolving blades. A bigger rotor diameter allows the blade to sweep a greater area, capturing more airflow and producing more power.

According to the wind turbine development reported by the Berkeley Lab, NREL in the U.S. [73], summarized by 163 of the world's foremost wind energy experts, more giant wind turbine scale is coming in the decades. According to the scale development of onshore and offshore wind turbines in Figure 2-17 and Figure 2-18, the rotor diameter is more significant than the hub height in a modern wind turbine. In general, the scale of land-based turbines is relatively smaller than offshore. After entering the 21st century, the hub height was getting closer to the Statue of Liberty (93 m). Modern turbines possess almost 80-meter towers and about 100-meter rotor diameters. Hence, the blade is sufficient to sweep an area 50 percent bigger than a football field [72]. While based on the survey forecast, the turbine size in the 2030s would chase after the next revolutionary stage, pursuing higher tower and power capacity under stable and operational conditions.

From a layman's perspective, individuals who believe that a more significant scale is always better may naively raise the size of the turbine and anticipate more power output. However, referring to the proven practice and expert data, this concept is incorrect; otherwise, there would be more towers over 200 meters within the framework of human capacity-building. Manufacturers purposely limit the maximum generating capacity to find the peak power generation efficiency [74].

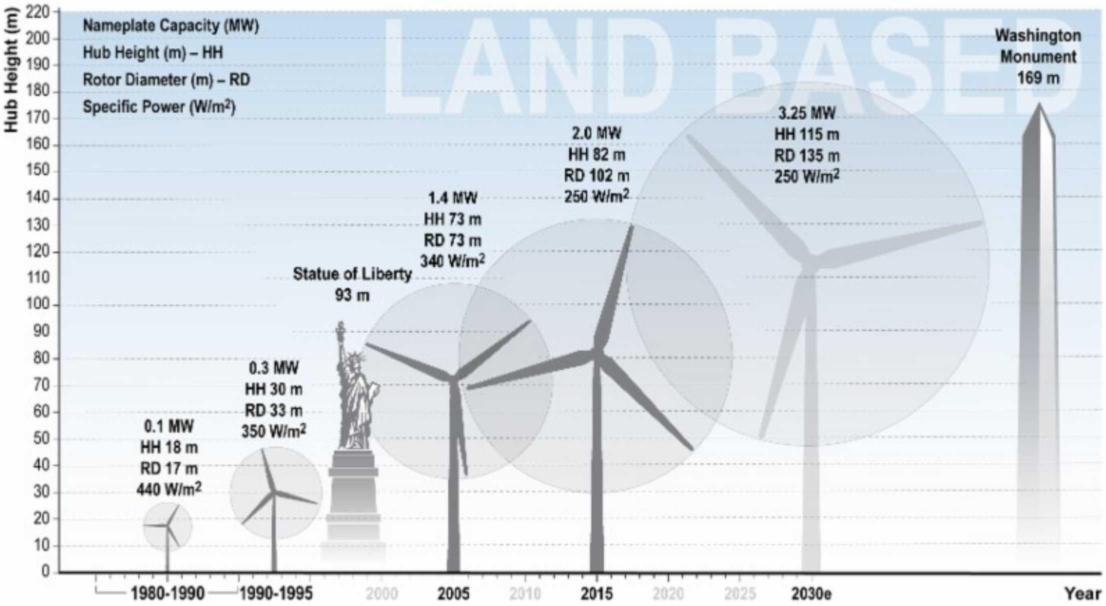

Figure 2-17: Hub height & rotor diameter development of onshore wind turbines [72]

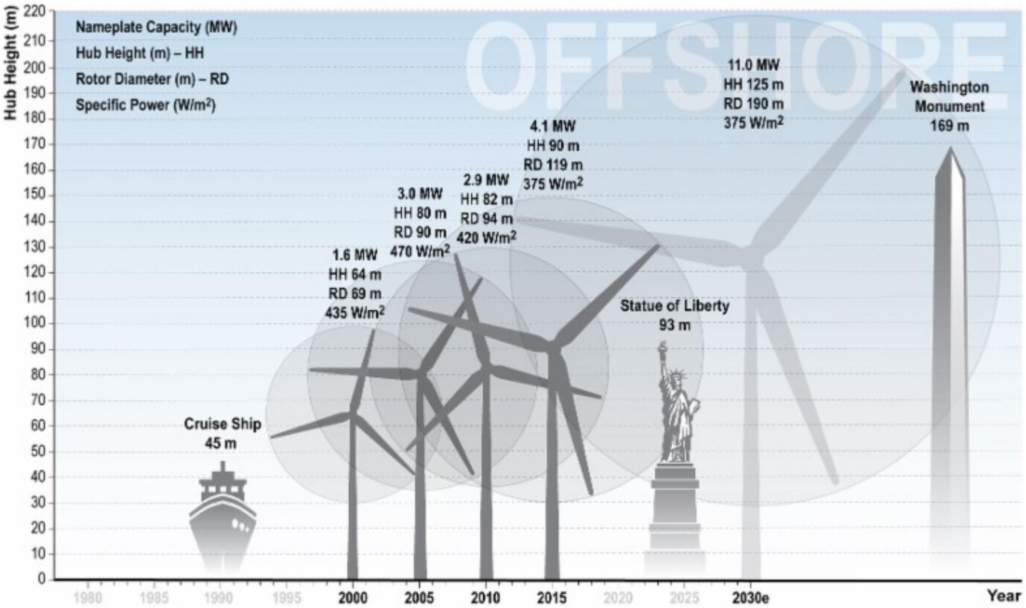

Figure 2-18: Hub height & rotor diameter development of offshore wind turbines [72]

The specific power of a wind turbine is the ratio of its nameplate-capacity rating to the rotor-swept area of the blade. When designing wind turbines for commercial use or distributed order, they deliberately adjust the critical ratio value. Increasing the size of the blades will reduce the specific power [74]. From the economic perspective, a wind turbine with low specific power can decline the Levelized generation cost [75]. In Figure 2-19, the collected data has proved that the magnitude of specific power is consistently downgrading from the beginning of the wind turbine invention. Therefore, the ever-low-specific-power wind turbine represents the development trends in the wind energy market, which means the blade size can not grow blindly.

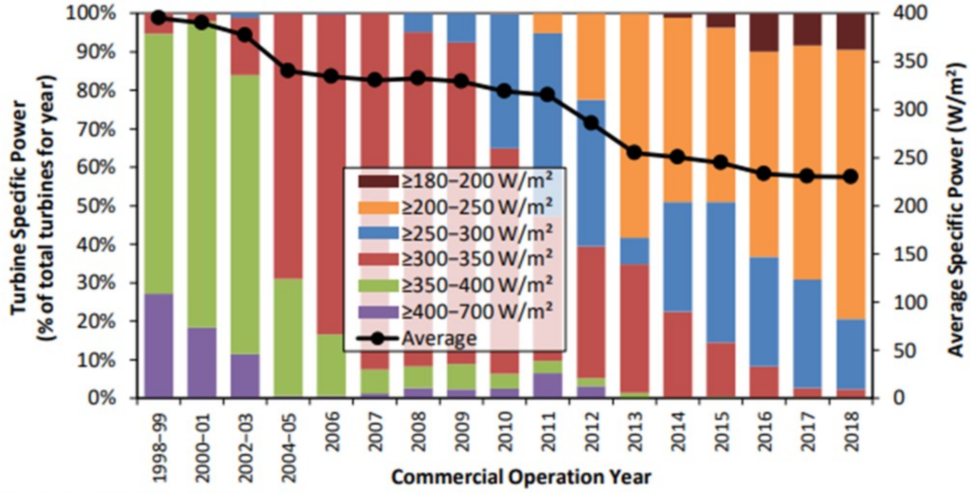

Sources: AWEA WindIQ, USWTDB

Figure 2-19: Specific power development trends from 1988 to 2018 [74]

2.2.5 Wind turbine blade (WTB)

This section will concentrate on the HAWT since it is more prevalent in the current wind energy market than the VAWT. Furthermore, HAWT is this project's NREL target type of 5-MW 61.5 meters blade. Additionally, the blade configuration on both spanwise and chordwise scales, the wind energy industry terminology, and design principles are introduced in this section.

2.2.5.1 Blade spanwise regions

For modern HAWTs, almost 15–20% of the cost of production is attributable to the rotor blades; therefore, optimizing and innovating the blade design would reduce the overall expense of manufacture [4], [5]. While designing a wind turbine blade, both aerodynamic and structural features must be considered and compromised optimally. According to Figure 2-20, the forward one-third span region is designed with the governing structural demand from the root area to the tip side; in contrast, the aft two-thirds span is typically designed with aerodynamics concerns [45], [76]. The root area, midspan, tip, and shear web are discussed below.

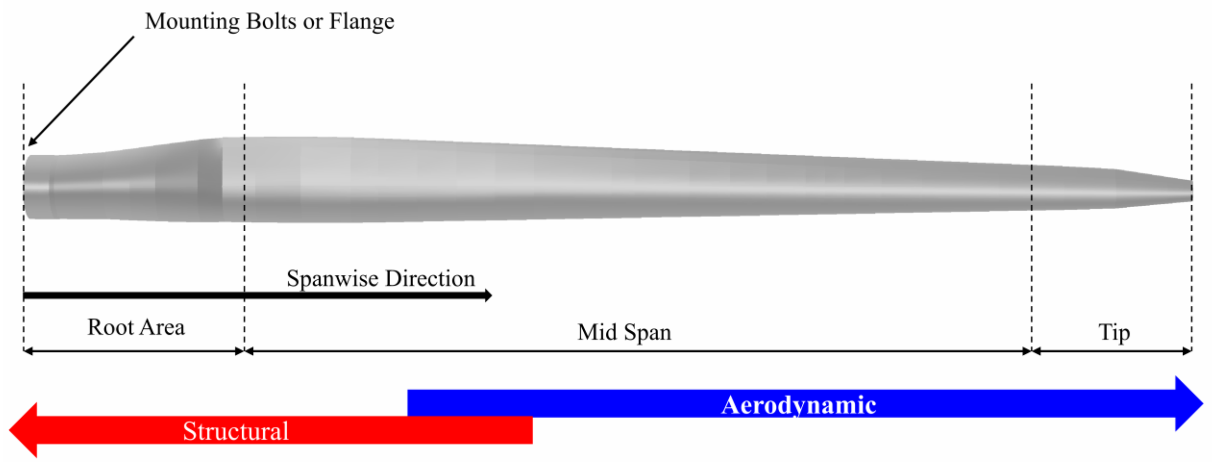

Figure 2-20: Blade spanwise regions [45]

Root area

As described in the literature [45], the root area is the transition between the rotor-mounted cylinder and the first aerofoil station. Bolt is the most common root connection type for WTBs, as shown in Figure 2-21, and the other root types are flange, hub, and stud/insert types [77]. The root area requires durable structural design because this section endures the highest load among the span. The critical loading usually comes from the blade's sudden starting and stopping. Hence, the airfoil profile is inclined to be thick and cylinder due to the structural demand, despite low aerodynamic efficiency.

Figure 2-21: A wind turbine blade with bolt root connection [78]

Midspan

The midspan of a turbine blade is used to provide a smooth transition from the root region to the tip and balance structural durability and aerodynamic efficiency [79]. The length is almost three-quarters of the entire span, but there is no strict definition for this region's start and end points. When Huang [80] investigated the flapping effect on the blade tip vortex, he selected 60-70% as the midspan. For a 61.5 meters 5-MW blade from NREL, a 10 to 54.5 meters span acted as the midspan for Joustra’s blade modeling [79]. Therefore, the midspan is a flexible transition zone connecting two sides of the blade. Nevertheless, this region should primarily guarantee the aerodynamic significance, employing thinner airfoils to increase the lift-to-drag ratio [25], even though sometimes it could slightly compromise the construction objective [79].

Tip

The tip design for a rotor blade is considerable because any slight adjustment would affect the overall aerodynamic damping and aeroacoustics [81], [82], and the tip is the main reason for operational noise, shouldered load carrying, and power output [83]. The tip region is the aerodynamic domain, which needs to utilize the thinnest and most thin airfoil sections to reduce noise and tip losses. Due to the complexity of the airflow around the tip in three-dimensional space, many researchers with backgrounds in fluid mechanics and aerodynamics dedicated their time to tip research and sought noise-optimized designs.

For this wind turbine blade considered in this thesis project, Resor [84] employed the blade element method to simplify the tip design when concentrating on structural analysis purposes. Another 5-MW blade user, Chow [85], distributed meticulous blade geometry with CFD (Computational Fluid Dynamics) software and deeply explored the aerodynamic flow conditions near the blade. Similarly, the CFD fluid analysis software also contributed to many researchers finding how different tip shapes impact the vortex noise and blade loading [86]–[88].

2.2.5.2 Shear webs

From the structural perspective, the blade can be regarded as a cantilever beam with hollow and varying cross-sections formed by two load-carrying shells, one for suction and another for pressure.

However, inner shear webs are typically added between two shells to provide extra buckling resistance and transfer shear loads. Figure 2-22, developed by DTU (Technical University of Denmark), depicts the basic structural configuration of shear webs constructed in a wind turbine blade, including the cross-section with a load-carry box gird, leading edge, and trailing edge [89].

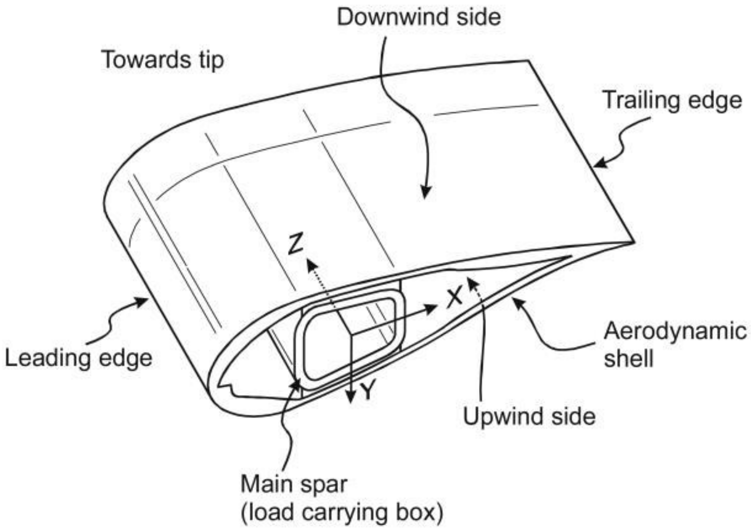

Figure 2-22: A spar box design from DTU [89]

Generally, a “web” as an internal support in a hollow structure provides extra stiffness and strength. Also, it can reduce the risk of structural distortion. Shear web, which ensures sufficient strength to withstand flapwise loading, shear force, and buckling in wind turbine blade designs, also connects both ends' spar caps with bonding joints to improve the structural integrity [90]–[92]. An internal structure of a blade can be regarded as the shear webs or a combination of the shear web-spar cap. Any adjustment for the substantial part would lead to a dramatic jump of the whole blade mass and affect the aerodynamic response [90]. Even though the primary design target is to lower the blade mass, some other factors should be considered vital constraints, including stress, strain, deflection, vibration, and buckling restriction [93]. Therefore, several vital parts must be considered while designing a shear-web structure for a wind turbine blade. They are (1) the number of shear webs, (2) shear web location (chordwise and spanwise), and (3) material utilization and thickness [94].

Figure 2-23 has sketched different configurations of shear web in a wind turbine blade. Two-shear-web configuration (Figure 2-23 (b)) is the most common selection for a wind turbine blade, although for small-scale blades, a single-shear-web internal structure (Figure 2-23 (a)) is enough to afford stable strength. However, for a longer-span blade, like the Sandia 100-meter all-glass baseline wind turbine blade [94], a third “short” web was assigned to pursue extra buckling resistance. DTU wind energy laboratory invented the box girder (Figure 2-22) and provided the possibility to reduce the cap thickness up to 40% [89]. Also, for some innovative designs, like a fabric-covered rotor blade (Figure 2-23 (c)), some ribs were added to increase the stability of the hollow structure [95]. Due to the use of thermosetting materials, this unique rib design is not suited for fabricating wind turbine blades economically [96].

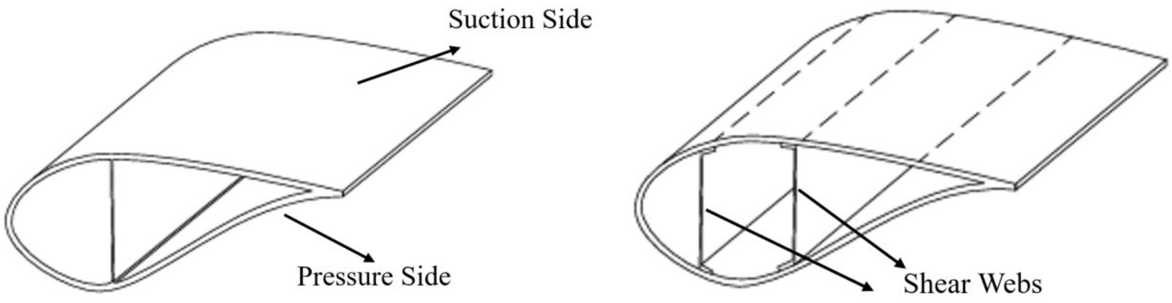

(a) One shear web (b) Two shear webs

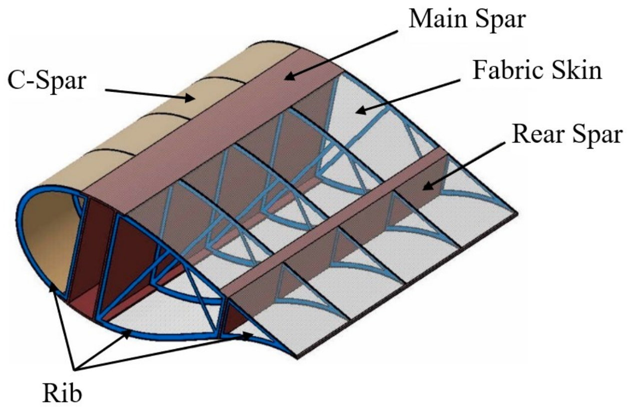

(c) Two shear webs with ribs

Figure 2-23: Different shear webs in wind turbine blade [95], [97]

As for the determination of shear web chordwise location, much research was done to find more optimization methods to balance the blade mass and stiffness properties. By adjusting the spar cap configuration and chordwise position, Alberto [98] developed an optimization algorithm to lighten the internal structure mass and then suggested that the current aerodynamic design for a blade was not optimal. Khan [90] chose the maximum stresses and deflection as the design constraints and used blade mass as a fitness function for a single shear web blade. They concluded that even though the shear webs were slanted to the trailing edge would lead to decreasing stress, the increasing mass would weaken the benefit. Therefore, most of the blade design is to find a relative optimal shear web location through computational simulation and experiments, which is probably not the best.

2.2.5.3 Wind turbine blade design

The discussion above introduced the fundamentals of the wind turbine blades' components. Nevertheless, to construct a qualified blade structure with high structural and aerodynamic performance for electrical generation, the following parts must be considered: determining tip speed ratio, airfoil selections, aerodynamic design, etc.

Tip speed ratio

The tip speed ratio (TSR) is the ratio between blade rotational velocity and relative wind speed, which is a highly critical parameter prior to determining other rotor dimensions [99]. This factor (Eq. 2-18) also leads designers to select a suitable blade size for a given generator.

$$\lambda = \frac{\Omega r}{V_w} \qquad \text{(Eq. 2-18)}$$

where,

λ : Tip speed ratio

Ω : Rotational velocity (rad/s)

r : Rotor radius (m)

V_w : Wind speed (m/s)

Several parts must be considered to determine the TSR (tip speed ratio), including the turbine types, mechanical problems, aerodynamic issues, power generation efficiency, noise, etc. [61]. For a working blade, if the rotor rotates at quite a low speed, the power generation would be limited due to less airflow captured; nevertheless, if the rotor rotates very quickly, the drag force and centrifugal stress would increase dramatically. The general TSR range for a two-blade HAWT is from 9 to 10, and 6 to 8 for a three-blade type, where 7 is the most widely-selected value for manufacturers [100].

Blade configuration

While designing a HAWT blade, the BEM (Blade Element Momentum) method was employed to calculate the two vital parameters, i.e., chord length and twist angle, based on the Betz limit, operational airflow conditions, and aerodynamic forces [45], [100]–[103]. There are also some other BEM-based and evolved concepts to find appropriate blade configuration values in specific conditions. The Betz formula (Eq. 2-19) is the most straightforward choice [104]–[107] to determine the optimum chord length.

$$C_{opt} = \frac{2\pi r}{n} \frac{8}{9C_L} \frac{U_{wd}}{\lambda V_r} \qquad \text{(Eq. 2-19)}$$

where $V_r = \sqrt{V_w^2 + U^2}$

r = Rotor radius (m),
n =Blade quantity
C_L = Lift coefficient
V_r= Local resultant air velocity (m/s)
U = Wind speed (m/s)
U_{wd} = Design wind speed (m/s)
C_{opt}= Optimum chord length

On the other hand, the application of the Betz method is limited to offering a standard and basic modern blade shape, illustrated in Figure 2-24 [100], with a tip speed ratio of six to nine. However, for some low tip speed cases and more practical utilization, several optimal methods considering the wake and drag losses are more accurate than Betz's. That is why many researchers investigated the optimization blade design based on the given Betz theory and improved the power generation efficiency and blade mass magnitude [5], [61], [105], [108]–[110].

Blade airfoils

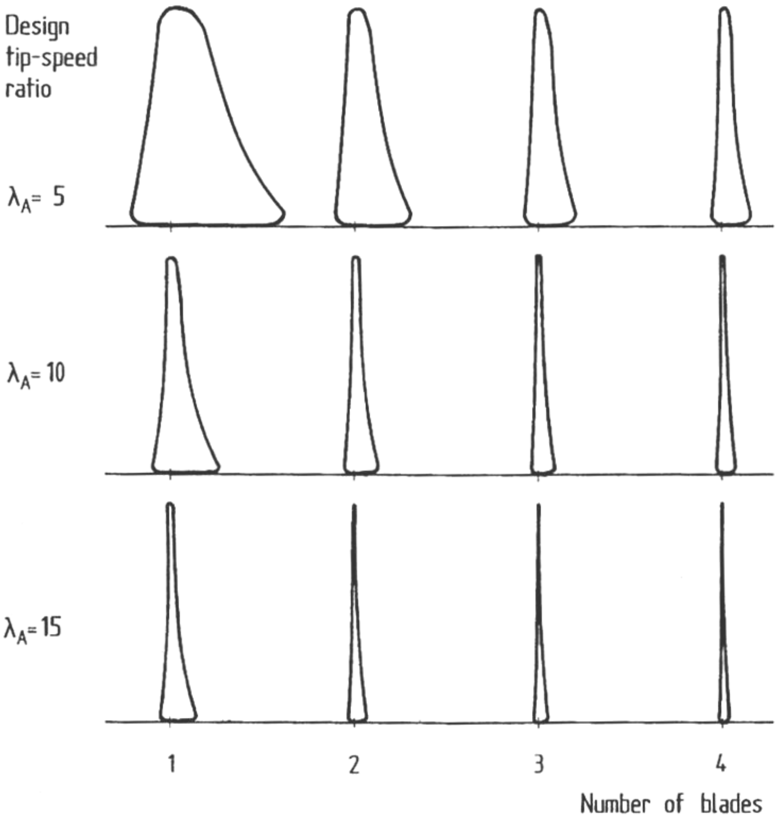

Figure 2-24: Basic blade shapes derived by the Betz method [100]

What has been covered so far pertains to the WTB design theory and the spanwise configuration of a primary blade. Before moving ahead, it is necessary to clarify the importance of airfoil selection during blade design. The lift and drag forces are the two types of aerodynamic loading that drive the turbine blade to complete energy conversion. Nevertheless, lifting is more effective in power generation than dragging, about 50 times greater in the unit working area. Hence, the airfoil was deliberately shaped to pursue the maximum ratio of lift to drag, generally more than 30 for a modern wind turbine blade, defined in (Eq. 2-23) [111].

Airfoil is the selected chordwise shape for the cross-sectional shapes of a blade and lofting along the span to form the blade structure, where the lifting or dragging forces can be thought of as attacking the airfoil equivalently. As shown in Figure 2-25, several design parameters are introduced to determine a specified airfoil, including chord length, thickness, camber (line), attack of angle (AoA) α_{AOA} , suction side and pressure side, leading edge, and trailing edge. Appropriate parameter selection would lead to higher power productivity and conversion rate. When accounting for the relative wind impacting the airfoil, the angle of attack (AoA) was used, which is the angle between the chord line and wind velocity direction. The front side of the airfoil is the leading edge, whereas the back is the trailing edge. The chord line is a straight line connecting the two sides, and the length represents the airfoil magnitude to a certain extent. Another dotted curve shown in Figure 2-25 is the camber line, located halfway between the pressure and suction sides. Correspondingly, the perpendicular distance from the chord line is the camber. Thickness is measured perpendicularly to the chord line by the distance between the pressure and suction sides. Furthermore, the ratio of thickness to chord length is another vital indicator while scheduling the airfoils along the span, which is the magnitude of thickness divided by chord length. While engaging in advanced aerodynamic design for a particular airfoil, several geometric features must be addressed, such as the maximum thickness and thickness distribution, leading-edge radius, and trailing edge angle [50], [112].

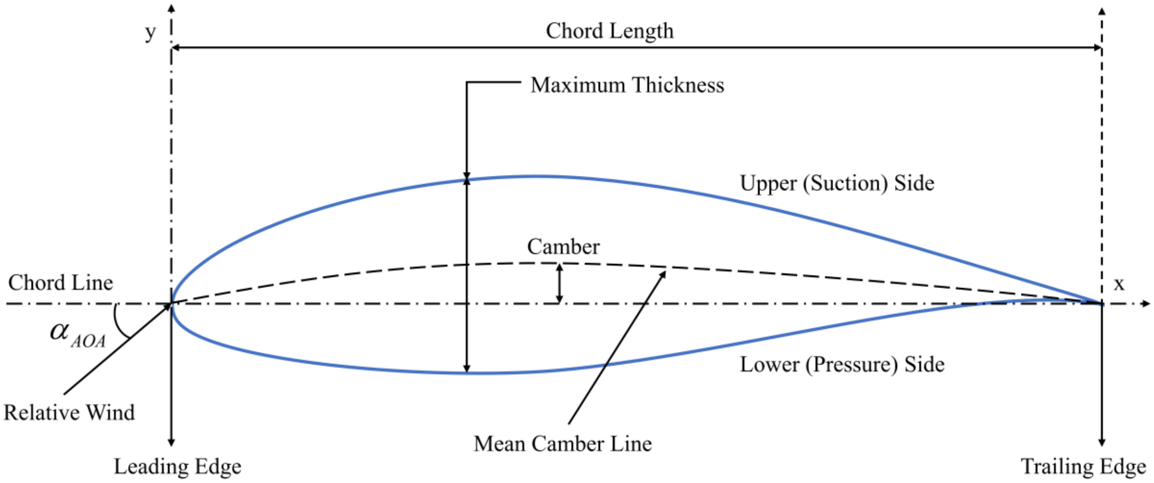

Figure 2-25: Airfoil configuration for the cross-section of wind turbine blades [113]

Airfoil aerodynamic design

After determining the airfoil geometrical details on the cross-section scale, the next task is arranging the blade to carry the aerodynamic loading, like lift and drag forces, and optimizing the aerodynamic properties. Excellent aerodynamic performance is essential for designing efficient blade rotors [114]. The lift force is formed when the airfoil creates the acceleration of air down to the upper surface due to the bending airflow so that the air must apply an equal and opposite (upward) force on the airfoil, which produces lift [115] that perpendicular to the attacking wind direction. Drag force is perpendicular to the lift force or parallel to the attacking wind. As shown in Figure 2-26, where the F_L and F_D is the lift force and drag force, respectively. They are calculated by (Eq. 2-20) and (Eq. 2-21), which compose the resultant force F_R. Also, the Reynolds number *Re* (Eq. 2-22) represents the fluid flow conditions in different velocities for a specific aerofoil, which is the ratio of inertial forces to viscous forces.

$$F_L = \frac{1}{2}\rho c C_L U_{rel}^2 \qquad \text{(Eq. 2-20)}$$

$$F_D = \frac{1}{2}\rho c C_D U_{rel}^2 \qquad \text{(Eq. 2-21)}$$

$$Re = \frac{U_{rel}c}{v_k} = \frac{\rho U_{rel}c}{\mu} \qquad \text{(Eq. 2-22)}$$

F_L, F_D are lift and drag forces, C_L, C_D are lift coefficient and drag coefficient, ρ is the free stream density, U_{rel} is the relative wind velocity, c is the chord length. v_k is the kinematic viscosity, and μ is the dynamic viscosity.

During the airfoil and blade design procedure, manufacturers prefer to maximize the lift and minimize the drag due to their respective encouraging and impeding in power generation; therefore, the drag-to-lift ratio (Eq. 2-23) is of concern. In response to the high requirement of the lift-to-drag ratio, modern designers generally selected a value of more than 30 [111]. Due to the difficulty in mathematically predicting the coefficient of lift to drag, the conventional technique employs actual trials at a certain angle of attack and Reynolds number [116]. However, in the contemporary blade design process, some professional and powerful software is used to determine the ideal value contributing to the distinct aerodynamic design, such as XFOIL [117], QBLADE [118], etc.

$$\text{Lift to Drag Ratio} = \frac{C_L}{C_D} \qquad \text{(Eq. 2-23)}$$

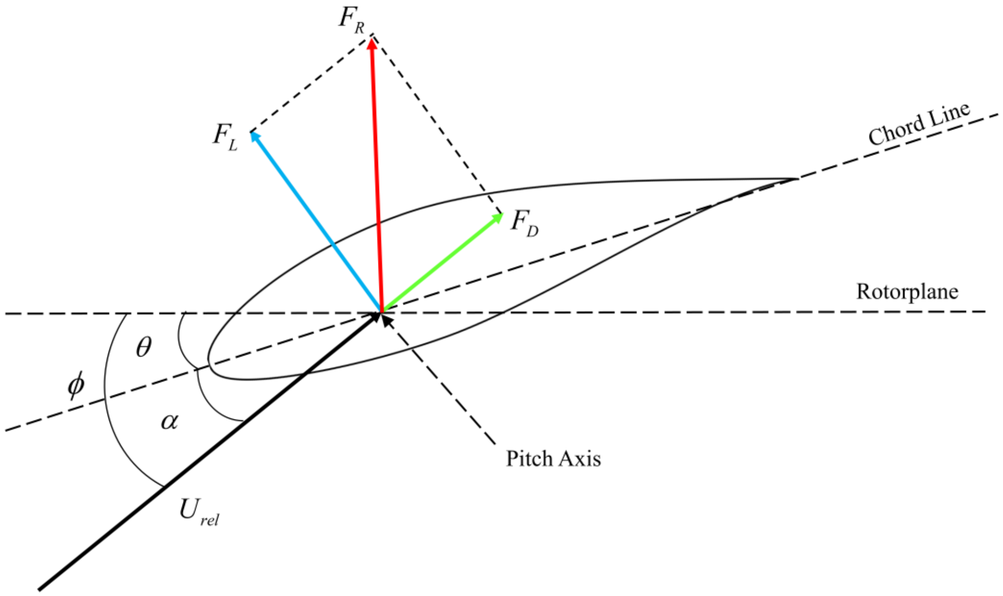

Figure 2-26: Lift and drag forces attacking the blade airfoil

In terms of the angle parameters mentioned in Figure 2-26, α is the angle of attack, and θ is the twist angle or pitch angle, ϕ is the angle of rotor plane rotation, or relative wind angle, which is the angle between the rotor plane and wind. Therefore, the attack angle plays a significant role in blade aerodynamic design. The twist angle is calculated by the design tip speed ratio and angle of attack [45]. Based on the Blade Element Momentum Theory [41], the relative wind angle can be calculated by:

$$\phi = \tan^{-1}\left(\frac{2}{3\lambda}\right) \qquad \text{(Eq. 2-24)}$$

Where the λ is the tip speed ratio; thus, the twist angle is:

$$\theta=\phi-\alpha \qquad \text{(Eq. 2-25)}$$

The basic process is based on the relationships among aerodynamical loadings using Blade Element Theory and the concept of Blade Element Momentum Theory [50], [119]. Readers of interest can refer to relevant literature for details and thus not elaborate here.

The angle of twist combined with chord length are the two primary parameters, especially while distributing the airfoil configuration in each control station. Any adjustment of the twist angle would affect the aerodynamic performance a lot. Typically, the twist ranges from 0 to 20 degrees along the blade span, and some manufacturers prefer to cut the production cost by decreasing the twist angle or simplifying the blade shape. However, this action might decrease the lift-to-drag ratio [45], [120]. Therefore, exploring twist angle optimization with another vital factor, chord length, is still a popular research aspect in today's wind energy and aerospace industries. In order to find a more optimal blade design, some researchers used the linearization method to optimize the chord length and twist angle radial profiles [50], [114], [120]–[123]. Moreover, some others introduced mathematical algorithms, like genetic algorithm (GA), artificial neural network (ANN), extended compact genetic algorithm (ECGA), etc. [124]–[126] for this purpose.

After determining the airfoil configuration and design parameters, the next step is to distribute these selected shapes along the blade span, like the below 5-MW blade airfoil distribution example in Figure 2-27. A particular efficient turbine blade is composed of a series of airfoil profiles with smoothly decreasing twist angles in a spanwise direction, resulting in a circular flange from the root view (Figure 2-28). Simple or single aerofoil usage could result in preliminary design and low power-transverse productivity [111].

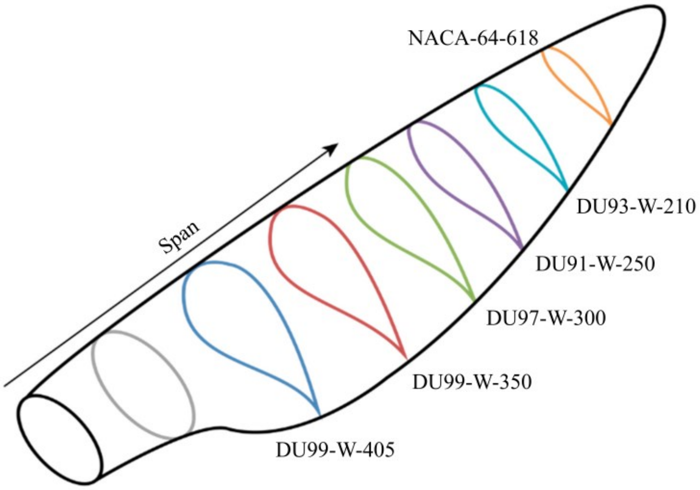

Figure 2-27: Airfoil spanwise schedule for 5-MW blade

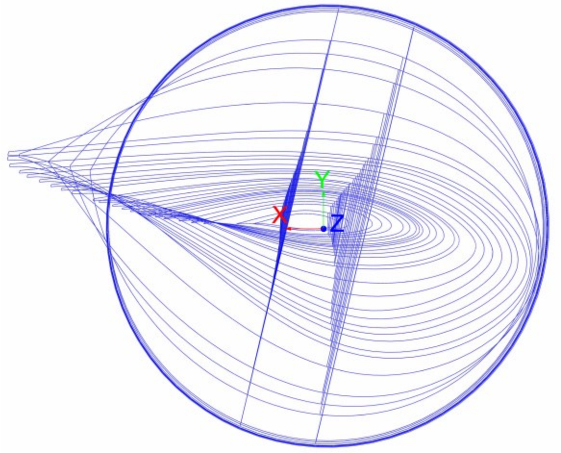

Figure 2-28: Blade root view for decreasing twist angle

As discussed earlier, the blade can be divided into three parts in the spanwise direction, root, midspan, and tip. Based on the distinguished requirements of structure and aerodynamics, appropriate aerofoils can be employed if referring to the instruction listed in Table 2-2. Generally, the aerofoil could be selected concerning the thickness-to-chord ratio (*t/c*), representing the structure and local configuration. Thick airfoil sections typically have a lower lift-to-drag ratio but higher load-carrying ability. Therefore, a type with a high thickness (*t/c* > 27) was often used in the root region to prevent bending failure. Because of the forward tilt of the maximum thickness, the centers of shear and gravity will be brought closer to the aerodynamic center, which will assist in the resolution of challenges associated with instability [127]. While approaching the tip side of the blade, the aerofoil gets thinner to increase the aerodynamic performance [128].

The geometrical compatibility represents the demand for smooth thickness distribution along the span-controlled thickness-to-chord ratio changing. For a qualified wind turbine blade, the surface thickness should decrease gradually and avoid sudden ply drop, which could bring higher aerodynamic performance. Roughness caused by dust, bugs, or manufacturing imperfections located at the leading edge may decrease lift-to-drag efficiency [127]. The off-design is also a random operation accounted for during turbine production due to the stochastic feature of wind, therefore need to ensure the lift-to-drag ratio below stall in most cases. As for the C_L selection, it is similar to the problem of structural-and-aerodynamical balance. Reducing C_L and sacrificing some aerodynamic properties is necessary to desire highly structural solidity near the root. By contrast, it will be as much as possible to increase the lift-to-drag ratio at the tip region;

nevertheless, the side effect is the operational noise. Therefore, the manufacturer should determine the parameters according to the specific usage scenarios.

In the practical manufacturing procedure of the blade, several simplified methods are employed to reduce the production cost, including (1) reducing the twist angle, (2) linearizing the chord length, and (3) decreasing the number of aerofoil types. Nevertheless, the economic consideration should be based on the satisfied guarantee of power generation productivity [45].

Table 2-2: Instruction on airfoil selection in different regions along the blade span [127]

Term	Span position		
	Root	Mid span	Tip
Thickness-to-chord ratio (*t/c*) (%)	>27	27-21	21-15
Structural requirement	High	Medium	Low
Geometrical compatibility	Medium	Medium	Medium
Maximum lift insensitive to leading edge roughness			High
Design lift close to maximum lift off-design		Low	Medium
Maximum C_L and post-stall behavior		Low	High
Low aerofoil noise			High

Blade loading

This part deals with the loads applied to a turbine blade for design purposes. Due to the numerous aerodynamic loading conditions, predecessors have simplified the design work into several vital cases: (1) emergency stop condition, (2) operational extreme loading, (3) parked 50-year storm scenario [41], [45], [129], [130]. Based on the significant scenarios, the dominant loading types can be summarized: as (1) aerodynamic, (2) gravitational, (3) centrifugal, (4) gyroscopic, and (5) operational [41].

The magnitude and direction of aerodynamic loadings are hard to calculate analytically. Therefore, some computer-aided methodologies are introduced to model the blade's complex operating circumstances, such as computational fluid dynamics (CFD) using finite element analysis (FEM). General-purpose tools such as ABAQUS, ANSYS, and other commercial software specialized for the aviation or wind energy industry, like GH BLADED, QBLADE, AeroDyn, FAST, etc. [131], can be used. As for the state-of-the-art blade design code, the IEC 61400-Series provided significant vital points and guidelines to handle the task. Relevant loading information is briefed as follows.

The lift and drag force form the aerodynamic loading, and the key factors are the angle of attack, wind speed, blade velocity, and airfoil configuration. The calculation can be derived from Blade Element Theory and Blade Element Momentum theory [41].

The gravitational and centrifugal forces (Figure 2-29) are mass-dependent, and it is commonly believed that these forces would rise cubically with increasing turbine diameter [132]. In this case, these loads can be regarded as ignorable for the blades with less than 10 meters span. In other cases, the gravitational force is defined by the blade mass multiplied by the acceleration of gravity, and its direction is absolutely toward the ground [45]. The centrifugal force is a function of rotational velocity squared and mass, which always operates radially outward; consequently, higher tip speeds imply more significant load requirements. The superposition of centrifugal and gravitational strains produces an alternating condition with a wavelength equal to one blade rotation.

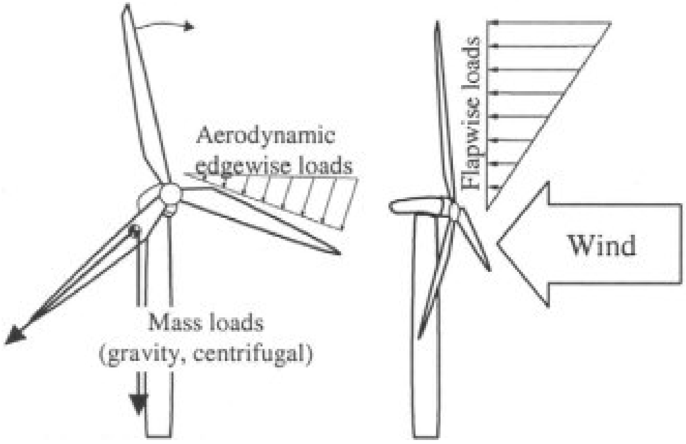

Figure 2-29: Load cases on wind turbine blade [133]

The blade mounted on the rotor could be regarded as a cantilever beam. The aerodynamic loading calculated by commercial software can be correspondingly applied at specific points along the span in flapwise or edgewise direction [134], [135], which is sketched in Figure 2-29.

The aerodynamic force will lead to complicated load scenarios on the blade, which can be simplified by BEM theory into distributed loading applied on the span in flapwise or edgewise directions [61]. Flapwise bending is the first critical load case, indicated by red in Figure 2-30. Thus, as a cantilever beam, the bending moment, local deflection, and material stresses at any blade location can be derived by traditional structural analysis. The edgewise bending moment is caused by blade mass and gravity force, which is negligible for small mass but critical for the large blade with over 70 meters span [61]. Like flapwise bending calculation, the edgewise case is equivalent to a cantilever beam. When the blade is placed horizontally, the second moment of area, moments, stress, and deflection can be derived. Figure 2-30 is a blade loading analysis case that used AeroDyn [136] to find simplified distribution loading on the span. The red indicates the flapwise bending moment, and the blue represents the edgewise type [98].

During a blade’s normal operational conditions, fatigue loading is of concern. For individual load cycles, the magnitude might be small and hard to cause material or structure damage only once. However, due to the long service of a blade, generally twenty years or more, the numerous repeated load cycles would accumulate severe failure to the material. Fatigue loading is the consequence of cyclic gravitational loads equivalent to the number of blade spin during its lifespan. Another source of fatigue is the gusting wind, which would cause almost 1 billion times throughout the turbine's lifetime [137]. Therefore, fatigue loading is sometimes more critical in WTB design than ultimate load conditions.

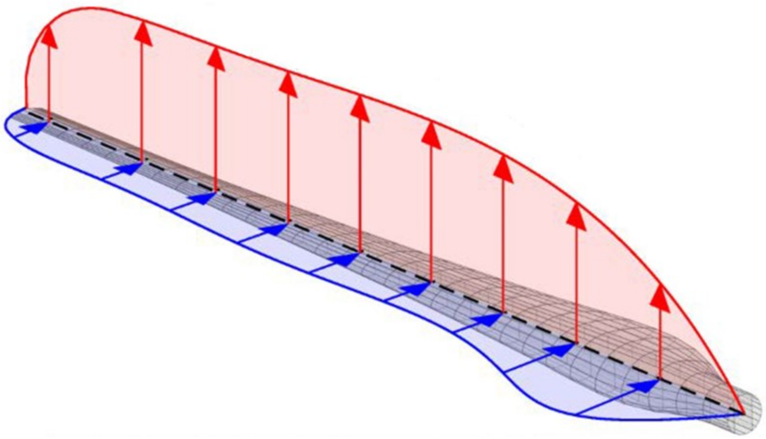

Figure 2-30: Equivalent flap-wise and edgewise loading simplified by BEM theory [98]

red color: flap-wise loading, blue color: edgewise loading

2.3 Blade damage and inspection for maintenance

2.3.1 Damage types and failure modes of wind turbine blades

2.3.1.1 Typical damage types in wind turbine blades

The top three damaged types of wind turbine systems are blade, generator, and gearbox failure [6]. Since the blade significantly affects the turbine system's power generation, it is vital to understand common blade damage types, inspect these potential damages timely, and prevent catastrophic collapse.

Two main reasons can be used to explain the various blade damages, and the first factor is the harsh working conditions, like high winds, bird attacks, heavy rainfall, lightning strike, fatigue loading, shortage of material strength, anthropogenic factors, and so on [138]. The second factor is the inherent defect during the manufacturing process. The invisible defect can grow due to the harsh environment or complex operational load conditions (e.g., extreme aerodynamic load, fatigue load) [139]. Combining these two factors could cause different blade damage types and negatively affect the wind turbine blades. Blade damage could decrease power generation, shorten the service life [140], or generate extra noise (e.g., due to the uneven surface) [141]. For example, prolonged wet working conditions will lead to erosions (Figure 2-31 (a)). A lightning strike (Figure 2-31 (b)) would cause delamination among the materials and debonding between specific components [11]. The long-lasting ice accumulation during the winter leads to unbalanced mass distribution, which rotates in dangerous conditions and leads to unexpected risks [142], including a brittle fracture in some freezing weather [143]. Furthermore, the catastrophic structural collapse will be induced if these damages cannot be repaired timely, as shown in Figure 2-31 (c). As such, the investigation of damage detection for WTBs is undoubtedly meaningful, which not only benefits in cutting operational maintenance costs but also provides the possibility to avoid unwanted accidents and disasters.

In more detail, various damage configurations can be classified as failure modes, as sketched in Figure 2-32 and summarized in Table 2-3, including crack, delamination, and debonding [7]–[9]. Crack would cause irregular surface distribution, which impairs the aerodynamic performance [144], [145]. Furthermore, crack under fatigue loading will propagate dramatically, eventually destroying the blade structure [7]. Delamination happens inside composite materials stacked by multiple single layers, and it will weaken the material's strength and decrease its stiffness. Debonding is on a more macro scale, which will cause detachment between different blade components, like the joint between the spar cap and the shear web, leading to structural instability [10], [144], [145]. Other damage types, like fiber failure, layer peeling, and edge erosion, are also summarized in Table 2-3, combined with crack, delamination, and debonding [19]. These damages could happen to the internal part of blade components, like the composite laminates' debonding and failure, or reflected in certain outside skins. Nevertheless, the root section and bonding joints are the critical regions most susceptible to damage [10], [11].

(a) edge erosion [146] (b) lightning damage [8]

(c) structural collapse [147]

Figure 2-31: Damages on blades in practice

According to Table 2-3, debonding is one of the most prevalent forms of damage at commonly used adhesive connections in wind turbine blades. Because frequent debonding damage may occur anywhere along the span of the blade, it causes rapid fracture propagation that paralyzes the whole structure. Debonding is severe damage that requires additional investigation; thus, it is introduced in detail in the next section.

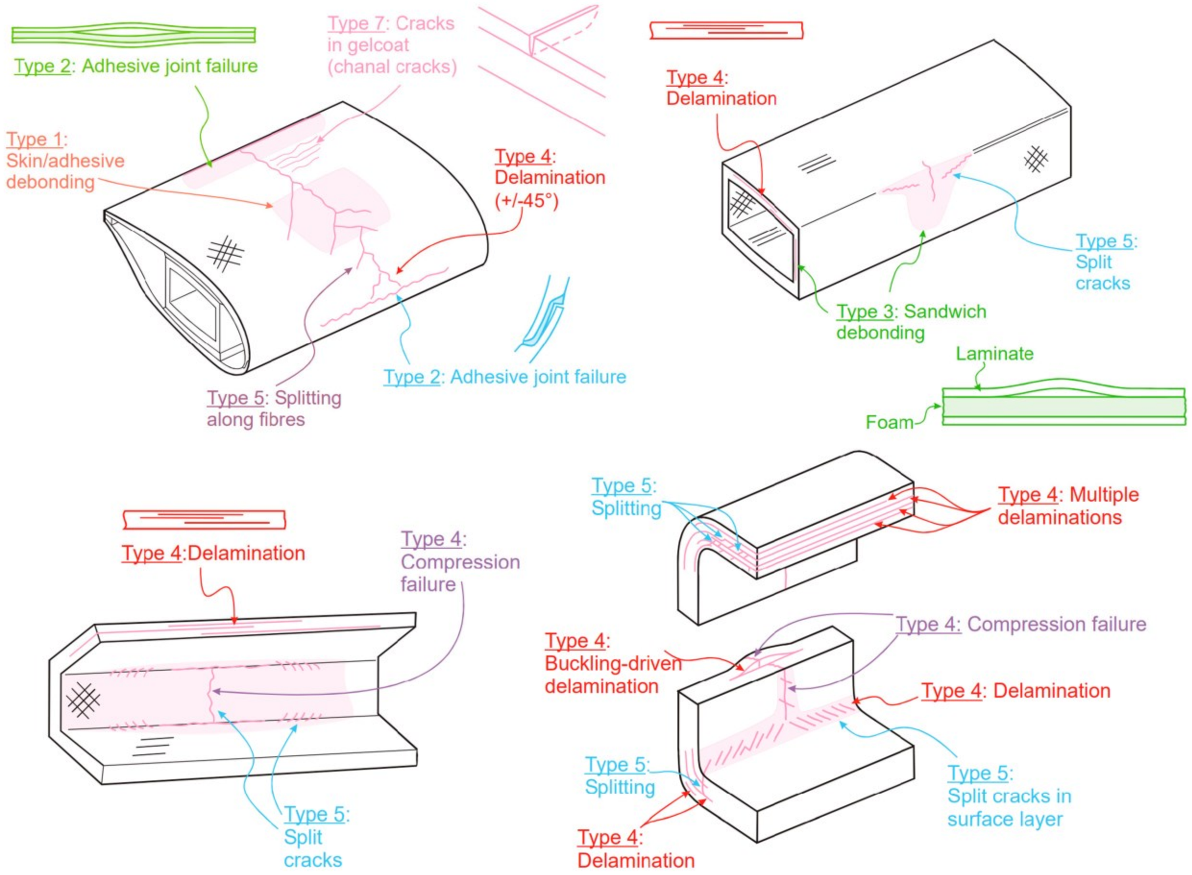

Figure 2-32: Common damage configurations in wind turbine blades [9]

Table 2-3: Common damage types in wind turbine blades [9], [19]

No.	Damage types
1	Debonding of skin/adhesive or main spar/adhesive layer
2	Adhesive joint failure between skins
3	Debonding of the sandwich panel face/core
4	Delamination due to tensional or buckling loading
5	Fiber breakage in tension, laminate failure in compression
6	Skin/adhesive debonding due to buckling
7	Gelcoat debonding or crack

2.3.1.2 Debonding damage in wind turbine blades

The wind turbine blade must be durable and lightweight, balancing satisfactory structural and aerodynamic performance. In order to achieve this requirement, composite materials with their characteristic low weight, high tensile strength, anti-corrosion properties, and chemical resistance are commonly used in blade manufacture [148]. Due to the susceptible characteristics of the interlayer and adhesions, composite laminates are prone to delamination and debonding failure. It is worth noting that delamination and debonding are similar but different. For a given composite material formed by multiple laminates or layers connected by resin or other adhesive materials, the detachment of adjacent layers is often called delamination failure. By contrast, debonding separates two materials or components connected with an adhesion joint. The adhesive failure triggered in a wind turbine blade due to unsatisfied design and manufacturing defects, including the ply drop-off, drilling, and curbed laminates, can cause debonding. The resultant weakened bonding connection is a common phenomenon in the wind energy industry [16], [91], [149], [150]. Due to these existing micro defects at adhesion joints (Figure 2-33), extra stress concentration and fatigue loading will accelerate defect growth and debonding propagation. Furthermore, in these weakened adhesions, the peeling stress from fatigue conditions would contribute to unwanted out-of-plane distortion [151] and buckling failure [152]. Hence, detecting debonding for timely maintenance is necessary before it propagates and destroys the blade structure.

Figure 2-33: Adhesive bond in the practical blade [153]

According to the summarization of damage types in Figure 2-32 and Table 2-3, delamination usually occurs at the interlayer of composite materials on a wind turbine blade. In contrast, debonding is usually located at the adhesive joints, for example, the spar cap-shear web connection, blade shell-web connection (see Figure 2-34) [12], blade skins at the trailing/leading edge, etc. In particular, the adhesive debonding failure (yellow part in Figure 2-34) between the spar cap and the shear web is of more concern primarily for the following two reasons:

(1) Debonding has proved to be the most common damage mode at adhesive joints, as discussed above and summarized in Figure 2-32 and Table 2-3 [9], [19]. Furthermore, debonding will likely be the first crack before other damages and will likely occur at the spar cap-shear web adhesive connections. This was evidenced in a comprehensive full-scale test on a 40 m wind turbine blade by Yang [16], who introduced flapwise loading until the structure collapses. The results indicated that the debonding at the adhesive joints between the spar cap and shear web was the initial damage failure, leading to a more extensive crack propagation to a final collapse. Another full-scale test focusing on the blade failure mechanism was accomplished by Chen [17], which indicated cap-web debonding as the typical and initial failure mode with severe loading. Tang [13] also observed the debonding initiated at the spar cap-shear web adhesion before the structure was crushed.

(2) The spar cap-shear web forms the “box” structure (Figure 2-23) to reduce the unsupported length of the blade skin and provide a more stable strength for the entire structure, which indicates this component is more critical for structural integrity than other adhesive locations. Nevertheless, the shear webs are connected to two-sided spar caps with adhesion joints. The debonding damage will significantly weaken the adhesive integrity and decrease the structural stiffness at the cap-web connection than the other parts of a wind turbine blade [13]–[15].

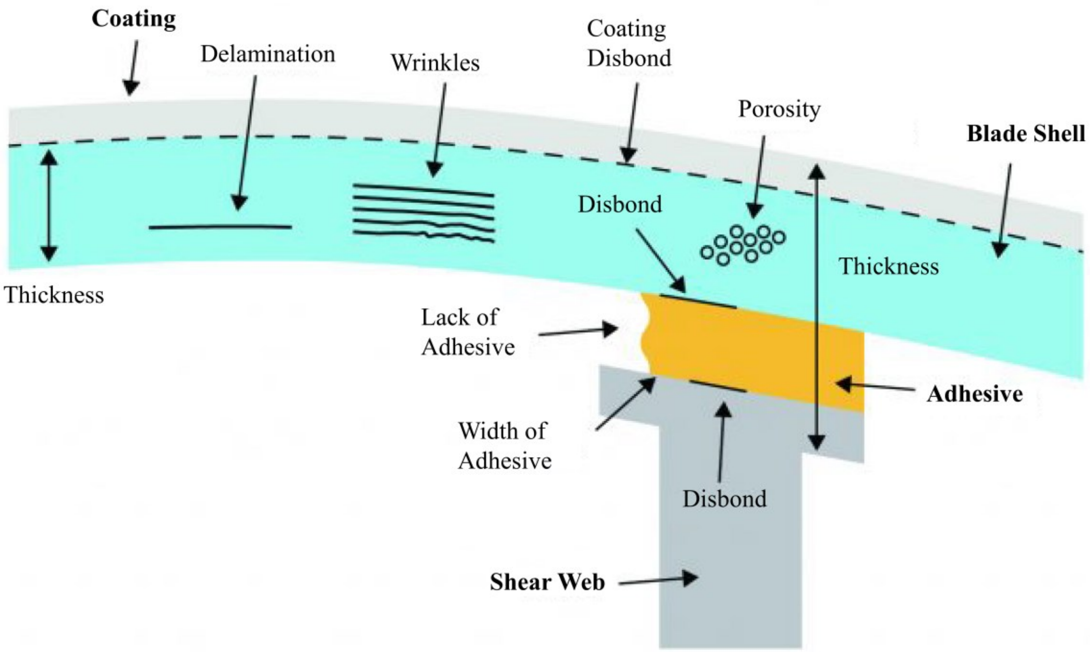

Figure 2-34: Typical damages located at blade shell and adhesive connections [12]

2.3.2 Modern damage detection techniques on wind turbine blades

2.3.2.1 Damage detection techniques

Inspecting the health of wind turbine blades is primarily intended to detect blade damages and potential safety hazards promptly, ensuring safe, keeping healthy operation, and preventing unexpected disasters. Furthermore, damage monitoring contributes to more effective operator maintenance [154]. State-of-the-art damage detection technologies are generally established on strain measurement, acoustic emission, vibration, ultrasound, thermography, machine vision, and others [11], [19], [155]–[158]. Most of these methods require sensors distributed on the blade to emit acoustically or collect response signals [10], [11], [159]–[162]. Some others use cameras to capture 3-dimensional images and determine the damage status by image-processing algorithms [163]–[166] or apply thermal-wave-radar to achieve blade inspection and diagnosis [146]-[147]. Each detection technology has advantages and disadvantages; thus, it was inclined to combine several techniques to inspect more well-rounded blade damages [169]. The following part will introduce these mainstream damage-detection technologies' basic concepts, advantages, disadvantages, and applicability.

Strain measurement

Strain measurement is an economical damage-inspection technique that uses strain sensors to detect slight changes in the deformation of wind turbine blades [159]. Under the applying load, the sensor can monitor the micro changes of a wind turbine blade; if the deformed size exceeds the historical threshold, the damage might be inspected. Direct strain and shear strain are often measured in blade inspection, and the strain, peak strain, Bragg wavelength deflection, and other signals are indicators to detect damage [170]. The strain sensors have two types: strain gauge (Figure 2-35) and Fiber Bragg Grating (FBG). Strain gauges are often distributed on the surface of blade skins, mainly serving for high-stress prevention and damage detection at specific positions [171]. However, this type of sensor is inclined to lose effectiveness during long-time work [172]. Fiber Bragg Grating (FBG) is embedded in fibers inside the blade structure, which can inspect strain variation and temperature variation [173]. In addition, strain measurement has the benefit of being able to monitor the turbine blade over extended periods continually. However, its accuracy and sensitivity rely on the distance between the sensor and the damage. It also depends on a large amount of sensor distribution, the possibility of sensor failure, etc. [19], [22].

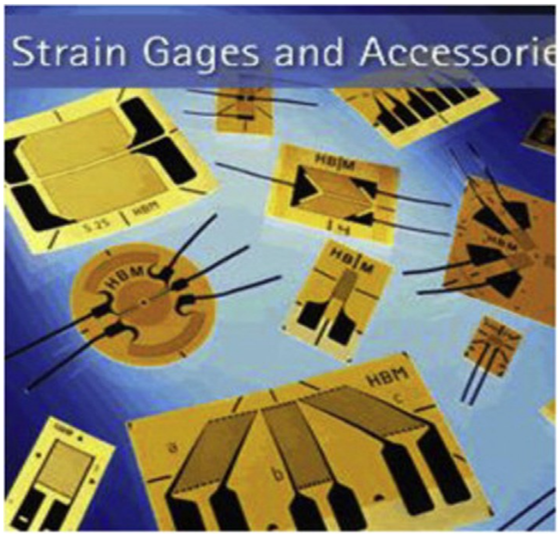

Figure 2-35: Strain gauges [159]

Acoustic emission

Acoustic emission is a passive online detection approach in which a sensor positioned on the blade collects the transient elastic waves released by the structure and materials of the blade. Typical blade damage, such as excessive deformation, crack propagation, and debonding, may cause the emission of these transitory elastic waves used for inspections [174]. Referring to the working principle of acoustic emission illustrated in Figure 2-36, damage causes an energy wave that generates high-frequency sound waves inside the blade structure, which can be detected by acoustic emission sensors [175]. Multiple AE (acoustic emission) sensors are usually used for wave-collected network construction and gather the damage-indicated characteristics, including Bragg wavelengths, acoustic emission signals (mean value, peak value, etc.), waveform signals (rise time, amplitude, etc.), acoustic energy, etc. [19]. Collecting these metrics makes it possible to monitor slight changes in the blade structure, such as fatigue, micro crack, stiffness change, or even irregular surface [144]. Therefore, in terms of the advantages of acoustic emission, it is sensitive to different types of blade damage, making it possible to achieve more accurate damage localization and visualization [19], and it needs fewer sensors than the strain measurement technique [176].

Furthermore, the acoustic emission method can realize continuous damage monitoring and give an early damage warning than strain measurement and vibrated-based technologies [19], [171]. However, many AE sensors must be assigned to achieve this good efficiency, leading to high expenditure [7]. Also, the cost will be increased due to the requirement of a complicated data processing system and the difficulty in discriminating the signals of acoustic emission and environmental noise, which is a central challenge for the modern acoustic emission technique [145].

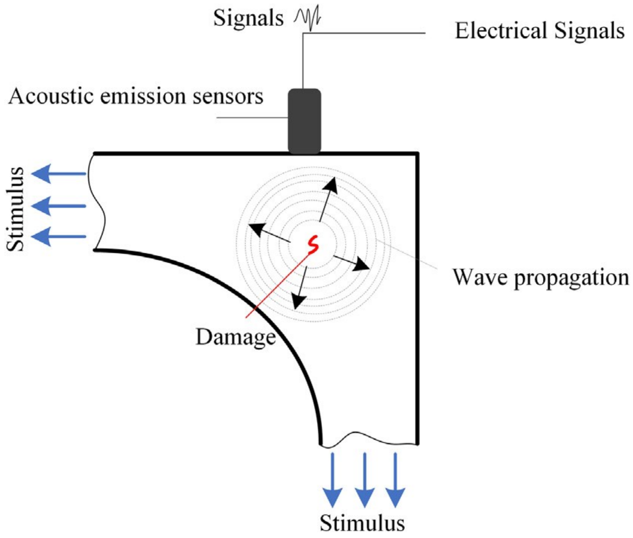

Figure 2-36: Work principle of acoustic emission [7]

Vibration techniques

Vibration data analysis is a prevalent technique that primarily assesses the blade's health by monitoring abnormal dynamic responses reflected in irregular oscillation, unusual vibration, or other signals [19], [177]. Because the damage (debonding or other damages) would reduce the stiffness in impaired regions, which leads to variation in natural frequency, mode shapes, amplitude, damping, and other dynamic properties, the differences will contribute to localizing the damage and visualizing the crack hidden inside the blade [178]–[180]. The vibration method generally includes free and forced vibration [181]. Free vibration analysis is implemented by an initial input (displacement or force) and allows the mechanical system to vibrate freely, which is often used for damage monitoring in cantilever structures (e.g., rotor-mounted blades) and extracting dynamic properties. Another mainstream vibrated-based method is the impact load analysis, which uses a hammer or other impactors to apply external excitation on the blade to trigger vibration. These vibrated responses can be collected by the sensors installed on the surfaces of wind turbine blades (Figure 2-37) include three types: displacement sensor, velocity sensor, and acceleration sensor, correspondingly used for ranges of low-frequency, medium-frequency, and high-frequency [19], [145], [169], [171]. Various signal processing techniques, regarding frequency analysis, time-domain analysis, and time-frequency analysis, are crucial for vibrated-based monitoring methods to extract instructive information and inspect the damage [19], [138]. The standard techniques include empirical mode decomposition (EMD), fast Fourier transformation (FFT), deep neural network (DNN), Hidden Markov model (HMM), and others [19], [145]. Researchers consistently focus on exploring novel signal processing and algorithms to improve damage-inspected efficiency [10]. Regarding the advantages of the vibration method, it is a mature detection method with the characteristic of non-destructive and high sensitivity. Moreover, its easy implementation, damage to localization and visualization capacity, and high development of algorithms contribute to the comprehensive utilization of WTB's health monitoring. By contrast, the defects reflect the inability of the early damage warning, and primarly restricted to the enviromental influence on the dynamic properties, which might mislead the vibration signals to a wrong way [19], [182], [183].


(a) (b)

Figure 2-37: Blade monitoring using vibration method with acceleration sensors [139]

Ultrasound

Ultrasound, a non-destructive technique, is widely used in damage defection in composite and other materials with mature development [184]. Figure 2-38 illustrates the primary mechanism of the ultrasound method: the first transmitter emits an elastic wave that can propagate through the blade structure and inside defects (e.g., debonding, crack, delamination); the second sensor will give the damage information based on the wave changes, such as amplitude, phase, propagation, time, reflection energy, etc. [19], [171]. Ultrasound monitoring is widely used for millimeter-level damages (e.g., debonding and delamination) inside the blade structure [145], [171], and also offers an early warning and inspection for inner damages [139]. By contrast, this detection technique is limited to complicated signal processing, and the wave-propagated path must cover the damage position unless the accuracy decreases [139]. Also, the ultrasound method is challenging to serve for working blades, which reduces many usage scenarios [185].

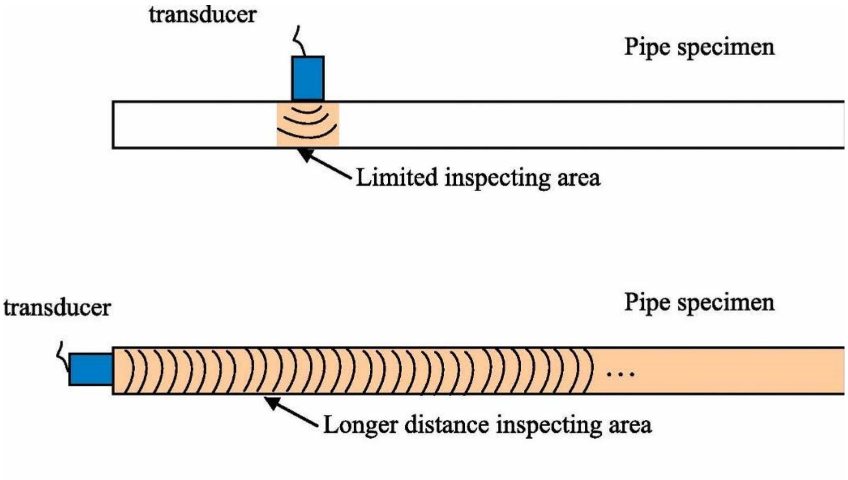

Figure 2-38: Mechanism of ultrasound testing [139]

Thermography

Thermography is a non-contact detection technique based on the collected thermodynamic properties of a wind turbine blade[186]. The blade damage (e.g., cracks, debonding, holes, etc.) will change the structural continuity, leading to low thermal conductivity and resulting in different temperatures on the blade's surface [187]. The infrared camera can collect these differences and achieve rapid damage detection. Moreover, it can help researchers develop the hotspot map of the blade structure and indicate the high-strain regions [139], [168]. Compared with other monitoring methods, thermal imaging can inspect the full-scale blade faster with comparable accuracy and efficiency [165]. Also, it does not need to assign many sensors on the blade, which can reduce the maintenance cost. However, the thermography highly depends on the temperature change of the blade surface. The temperature development is slow, so that not appropriate for early damage inspection [139], [188]. The detected results might be affected by ambient temperature, light reflection, pollution, and other external interferences [139], [189], [190]. Also, most thermography techniques need to shut down the blade rotating for temperature collection, reducing the electrical generation [139].

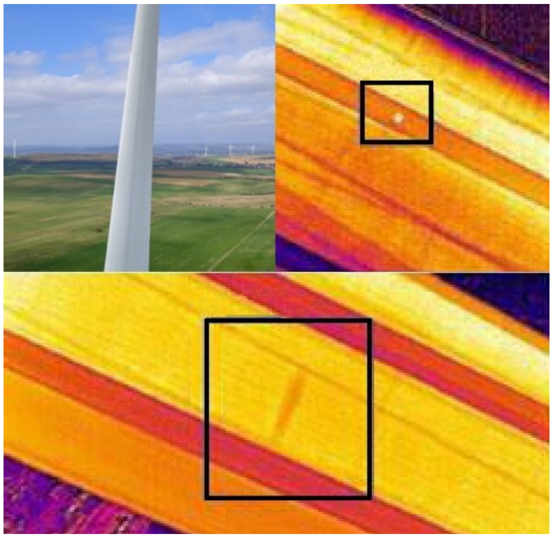

Figure 2-39: Thermal imaging technique for blade damage detection [139]

Machine vision

As shown in Figure 2-40, machine vision captures 2-dimensional or 3-dimensional images of the targe blade to indicate the structure damages like cracks, scratches, holes, ice, and other surface damages [166]. This method has been proven an effective and economical technology widely used in damage detection, dynamic identification, and so on [191]. Machine vision requires high-standard image devices, allows online monitoring, and reduces the operator's risks at the wind farm site [10]. However, the image information is not related to the physical mechanism. Therefore, it needs advanced capabilities of image processing with accuracy. Also, machine vision is often combined with other monitoring techniques and cannot work alone because it cannot inspect the damage inside the blade structure [192].

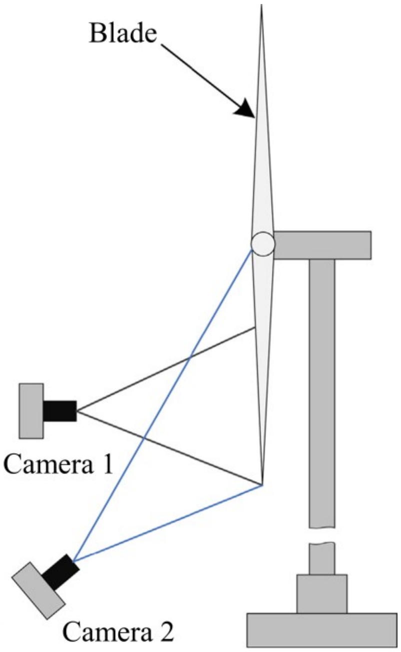

Figure 2-40: Machine vision technology for blade damage inspection [139]

2.3.2.2 Two other methodologies for damage investigation for WTBs

Before discussing the application examples of different monitoring techniques in wind turbine blades, it is necessary to introduce two other methodologies which contribute to investigating damage behaviors, with full-scale physical test and finite element simulation, respectively. They will provide helpful information to inform damage detection or inference.

Full-scale physical test

Before being put into operation, commercial wind turbine blades must pass full-scale tests to evaluate the blade's reliability and applicability [166], [193]. The full-scale experiment includes static and fatigue testing and is usually combined with numerical simulation to validate testing data. Thus, the blade strength and resistance of the ultimate fatigue scenario could be valuable, and observed the failure could be prevented by taking precautions, especially debonding failure. As a full-scale test example in Figure 2-41, the 52.3-meter-span blade was tested by Chen [17], who placed a wind turbine blade on the ground and applied different load cases by cranes. As a result, the complex failure characteristic was investigated. It pointed out that the cap-web debonding was the root cause of processing structural collapse, emphasizing the importance of providing relevant damaged characteristics for future damage monitoring. There are also many full-scale blade experiments to evaluate the blade's damage behavior and provide instructive information for maintainers to guard against critical damage during the blades' operation [16], [18], [92], [194]–[196]. However, the full-scale methodology only served the investigation while the blades were not operating; the high cost always accompanies this method. After the blades are mounted on the wind turbine rotor and begin the electrical generation, the damage monitoring must depend on the techniques discussed in 2.3.2.1.

Figure 2-41: Full-scale blade test [17]

Finite element method (FEM)

Another widely-used methodology is the finite element method (FEM), which helps researchers develop the blade model, reduce the experimental cost, simulate more complicated conditions, verify the experimental results, and investigate blade damage behavior more deeply. FEM is usually combined with other detecting techniques and does not work alone for damage detection. For example, an initially well-validated FE model for an intact wind turbine blade can serve as a reference, i.e., the digital twin of a wind turbine blade under healthy conditions. Using FE models can help reduce the investigation cost by better understanding the wind turbine systems. Especially for those large blades with over 70 meters or longer spans, the cost of increasing sensor utilization and full-scale blade testing sample would be elevated. On the other hand, while accounting for the critical fatigue loading case, the experimental cost and time would be significantly expensive due to the decade's lifespan of the blade [197]. In this case, the finite element method (FEM) can be employed, which profits from its satisfied reliability of blade modeling and accuracy of failure prediction [16], [198], [199]. Even without testing data support, the FE model can predict the damage evolution in the referenced range to a certain degree and provide instructive information for further research [17], [156]. As such, researchers devoted to blade damage almost always use physics-based FE models to verify the testing results or explore uncharted damage characteristics.

2.3.2.3 Inspection of debonding damage on wind turbine blades

The significance of spar cap-shear web debonding monitoring has been discussed earlier, which is crucial for structural collapse prevention and low-cost maintenance. However, not all damage monitoring methods mentioned above are appropriate for cap-web debonding inspection since each technique has strengths, weaknesses, and specific usage scenarios. The following part explains the damage detection cases of each technique. It points out why the vibration method is the most appropriate for cap-web debonding monitoring among the methodologies mentioned in 2.3.2.1.

Exact research of the other methods besides the vibration method

For example, strain measurement is good at developing the strain map of the blade and finding critical regions. Wu [160] constructed an extensive strain gauge network on a wind turbine blade, then used a novel algorithm to develop a two-dimensional strain map and monitored the blade health in time. Aihara [200] used strain gauges to design a blade-vibration monitoring system and measure the deflection scenario in real-time. Ginu [201] introduced fiber sensors to inspect the strain and temperature variation of the wind turbine blades. However, the strain measurement is hard to find usage instances for debonding inspections. Because this method significantly relies on the sensors, it requires many strain sensors, high time-consuming installation, and too expensive costs. Also, the sensors are inclined to lose efficacy and thus unreliable [19]. Acoustic emission is sensitive to different damage types and can determine the severity of damage [19].

Using acoustic emission, Tang [202] developed an identification technique for distinguishing between various damage failures on wind turbine blades. Zhou [203] used acoustic emission technology to assess the level of damage processing in delaminated wind turbine blade materials. Bo [204] revealed that by using specific algorithms, the AE signals might differentiate between various degrees of fatigue degradation. However, it is challenging to eliminate the considerable influence of environmental noise, leading to high data processing costs [10]. Furthermore, acoustic emission cannot provide the stress information of the internal structure, thus, unsuitable for the cap-web debonding analysis located below the blade surfaces [159]. Similarly, thermography and machine vision cannot effectively monitor the spar cap-shear web debonding damage under the blade surface, which are appropriate for inspecting blades' surface damage instead of inner failures [19], [139]. Furthermore, Yang [165] indicated that infrared photography techniques were not widely used in industry, and vision-based methods are still in the initial stages of development [19].

Ultrasound and vibration analysis are more appropriate regarding the spar cap-shear web debonding problem inside the blade structure. Ultrasound technology is extensively recognized for detecting internal damages and minute changes, such as cracks, debonding, and delamination [145]. Lamarre [12] developed a novel ultrasound phased-array methodology to inspect the adhesive integrity between the spar caps and shear webs during the manufacturing process with satisfactory efficiency. Ye [184] used pulse-echo ultrasound to construct an automatic system to reflect the internal damage in 2D/3D maps for WTBs. There are also many ultrasound-related investigations on WTBs with instructive achievements [205]–[208]. However, the biggest problem is that the ultrasound is difficult to inspect the damages for an in-service blade [185], which is unsuitable for maintenance scenarios after the blade is mounted. By comparison, vibration analysis is the mainstream method appropriate for spar cap-shear web debonding inspection on the operational WTBs, as a practical instance is shown in Figure 2-37. The related applications and research will be detailed and reviewed in the following.

Vibrated-based methods

The vibration method's fundamental principle, pros, and cons have been introduced in 2.3.2.1; it is widely used, easy to implement, and non-destructive, with high sensitivity to different damage severity [19]. Also, computation methodologies (e.g., finite element method (FEM), algorithms) are highly-developed to support vibration techniques better processing the dynamic signals and discriminating the blade damages.

Ghoshal [209] tested four algorithms to process vibration signals and monitored damages on a fiber blade using piezoceramic patches for excitation. Researchers continually investigate fresh signal processing and algorithms to enhance the effectiveness of vibrated-based inspection [10]. Currently, some well-established algorithms serve for vibration methods, including empirical mode decomposition (EMD), fast Fourier transformation (FFT), deep neural network (DNN), Markov model (HMM), and others [19], [145]. Wang [156] integrated the finite element method with vibration data analysis and extracted the modal shape curvature information as clues to localize and visualize the damages of the WTBs based on the modal properties. Skrimpas [210] used accelerator sensors to extract vibrational data to detect the icing damage on the blade surfaces, proving the vibration method's feasibility in real-time monitoring of ice or frozen configurations. Colone [190] developed a methodology to monitor blade health based on the statistical pattern and the variety of structural natural frequency.

Vibration analysis is also suitable for internal damage inspections, like delamination and debonding. DoliNski [20] combined the FEM and laser scanning vibrometry method to localize and visualize the delamination damages inside the blade structure. Hoell [21] proposed autoregressive model coefficients as the damage indicator to monitor the trailing edge debonding on the wind turbine blades. Ulriksen [22] used vibration analysis to extract the dynamic properties of a 34-meter blade and localize the trailing edge debonding damage by investigating the modal shapes and wavelet characteristics. Jang [14] introduced an artificial neural network to deal with natural frequencies and identify the debonding between the spar caps and shear web with 84% accuracy. Although the vibration-based method is the mainstream technique to detect damages on WTBs, most vibration method applications and research are related to surface damage monitoring. However, there is a lack of studies focusing on internal blade damages, particularly spar cap-shear web debonding inspection [16], which is crucial for blade health and is typically the cause of structural failure [17]. Therefore, to inherit predecessors' work and offset the limited investigation in spar cab-shear web debonding monitoring using vibration analysis, the current project will consider two parts to developing the debonding inspection research:

(1) Using two methods, free vibration, and impact load analysis, extract the vibrated properties of the 5-MW blade and compare the dynamic responses. Because the

vibration method generally includes free and forced vibration [181], but most of the modern research or maintenance on the WTBs use external force (e.g., manual hammer hit, force transducer, etc.) to induce the excitation and trigger the vibrated responses [211], [212]. The research on debonding monitoring or damage inspection using free vibration analysis is limited and hard to find in the aircraft and wind energy industry. Even though the forced-initiated method is more convenient for acquiring vibrational data with wide application, the free vibration is also effective in extracting dynamic properties and deserves further investigation regarding debonding monitoring on WTBs. Free vibration method is widely used for crack inspection in cantilever structures with satisfied efficiency [213] and also can inspect the debonding damage inside the composite material of the cantilever beam [214]. Therefore, the free vibration method to extract vibrated properties to infer debonding damage and contribute to further practical inspections deserves investigation. Also, research in this direction is short and hard to find, thus contributing to this project's significance.

(2) Regarding vibrated signal collection, it has bright room for development because the vibration method highly depends on the sensor installation, which is the root cause of the maintenance cost and monitoring efficiency. Based on the above literature review, many achievements are restricted by the sensor installation because it is impossible to arrange the sensor everywhere in the WTBs. Therefore, a more intelligent strategy for sensor distribution is indispensable while performing vibration methods to monitor damage. Including (a) pre-knowledge about the critical debonding regions of WTBs, which can reduce the unnecessary sensors' distribution, (b) an effective way to assign sensors for the sake of high-discriminated signals collection, (c) an effective way to trigger more effective signals which instrumented sensors can collect. These three aspects offer opportunities to reduce the sensor installation cost and increase data processing efficiency. To accomplish the goal, finite element simulation of wind turbine blades with and without debonding damage can provide helpful information for vibration-based inspection of wind turbine debonding, which is the main thrust of the research in this thesis work.

2.4 Modeling and simulation of wind turbine blades with and without debonding

2.4.1 Modeling of intact wind turbine blades

The finite element method (FEM) is the primary methodology to investigate wind turbine blade problems in the industry. Also, it is usually combined with the other damage detection techniques to develop better the monitoring system discussed in 2.3.2.2. FEM is often widely available in some commercial software, such as ABAQUS [215] and ANSYS [216], which can be used to develop the intact geometrical FE model and contribute to further investigation. For example, Yang [16] used FEM to develop a 40-meter blade model, simulated it with flapwise loading to be compared with the full-scale testing results, and developed a damage monitoring methodology based on stress-strain with numerical work. Chen [17] also used FEM to reproduce the physical blade, successfully verified the model with experimental results, built a more detailed blade model, and proposed a stress-based delamination or debonding monitoring method [13]. Also, FE can help simulate complicated load conditions that are expensive or hard to test in the real world. Caous [217] investigated the differences among four aerodynamic-load-application methods on a shell-element blade model. Albanesi [98] developed a topology-based optimization method to reduce the blades' mass by performing aerodynamic analysis with the help of the finite element method. Numerous previous achievements proved the effectiveness of the FEM technique for WTBs research [16], [198], [199]. Besides the blade model constructed by FEM in general-purpose software such as ABAQUS and ANSYS, some specialized software tools for WTB have also been developed and used. For example, NuMAD [218] was developed by National Renewable Energy Laboratory (NREL), which simplified the modeling procedure for modern WTBs with a significant database for WTB geometry and material designs. With the help of NuMAD, Jonkman [219] developed a famous 5-MW blade model, which has been widely used as a simulated sample in the industry. And QBLADE is another open-source tool for designing and simulating WTBs that delivers exceptional efficiency in blade geometry modeling and aerodynamic calculations [118].

The FE package embedded in ABAQUS was first employed in the current project to build the 5-MW blade geometrical model without cap-web debonding damage and verify the coherence with the reference database. Due to the global modeling strategy, the practical adhesive material thickness between the spar cap and the shear web is ignored. It will not be modeled in the global blade model due to the computational cost concern. In this scenario, the surface-based adhesive connection between the spar cap and shear web will be regarded as a tie constraint, a prominent methodology for describing the non-relative motion between two adherents [215]. And some researchers used MPC (multi-point constraint) to define the adhesive relationship between the spar cap and shear web, but with the same goal of the node-sharing characteristic [14], [17]. The spar cap-shear web connection can be constructed with more details regarding the local modeling strategy. For example, Tang [220] inserted the cohesive layer between shear webs and the spar cap with suitable thickness to evaluate the failure behavior of a blade's load-carry box. Hua [221] constructed a local cap-web joint with a 2.5 mm adhesive layer to perform elastic-plastic under bending and tension load conditions. However, even if the local-model method can reflect more details about debonding behavior, the computational cost and modeling difficulties will increase significantly due to the investigated objective on a global scale. Therefore, the tie constraint between the spar cap and shear webs will be added initially and served for model verification. Then the adhesive interaction will substitute the pre-defined connection and contribute to further debonding and vibration simulations.

2.4.2 Modeling of wind turbine blades with debonding

2.4.2.1 Adhesive material in wind turbine blades

Adhesive bonds are the most primarily used in the connections and are likely to replace bolts in composite WTB manufacturing because they could reduce almost 50% of the combined weight of the blade structure [222]. Generally, the adhesive materials used in wind turbine blades are (1) epoxy adhesives (EP), (2) polyurethane adhesive (PU), (3) methyl methacrylate adhesives (MMA), or (4) vinyl ester adhesives (VE) [223]. It is crucial to select suitable adhesive materials due to their significant influence on joint reliability. Among these four types, EP is typically the most widely used type. It offers better shear resistance and increases surface harness and strength under appropriate temperatures. PU adhesives perform well in low temperature, with higher toughness and flexibility, but susceptible to moisture and temperature fluctuation in uncured state. MMA adhesives are brittle but able to resist the crack extension to about 130%, and VE is appropriate at bonding polyester or vinylester resins.

2.4.2.2 Failure modes of bonded joints

The spar cap-shear web can be regarded as bonded joints, whose failure modes generally include three types: cohesive, adhesive, and adherend failure [224].

Cohesive failure

Cohesive failure occurs within the adhesive materials, having adhesive present on both adherents after breakage. Cohesive failure is often the consequence of shear load. However, peel stresses or a mix of both may cause cohesive failure. Inadequate joint design, such as inadequate overlap length, is a common cause of cohesive failure [224]. Figure 2-42 explains the two similar illustrations of cohesive failure configuration, which were from ASTM (American Society for Testing and Materials) [225] and Heslehurst, etc. [226].

(a) Cohesive failure modes from ASTM [225]

(b) Cohesive failure modes from Heslehurst and Hart-Smith [226]

Figure 2-42: Cohesive failure modes configuration

Adhesive failure

Adhesive failure is often named debonding, which occurs at the interface between the adhesive material and adherend, as shown in Figure 2-43. Adhesive debonding is commonly caused by improper manufacture and contaminated connections, which reduces bonded strength. Adhesive and cohesive failure modes may coincide. If the adherend surface is visible and the adhesive has split close to the surface, then such a combination is still classified as an adhesive failure.

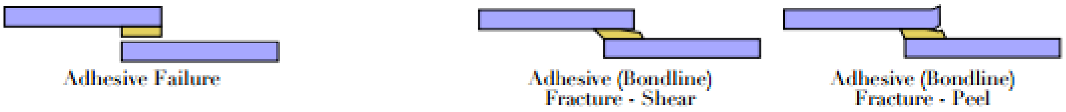

(a) Adhesive failure modes from ASTM [225]

(b) Adhesive failure modes from Heslehurst and Hart-Smith [226]

Figure 2-43: Adhesive failure modes configuration

Adherent failure

Adherent failure occurs at the bonded joint's two-side adherend, as illustrated in Figure 2-44. The general reason for adherend failure is the improper manufacture and strength shortage for adherent composite materials. For the current project, only adhesive failure mode is considered to simulate the debonding analysis between the spar cap and shear webs.

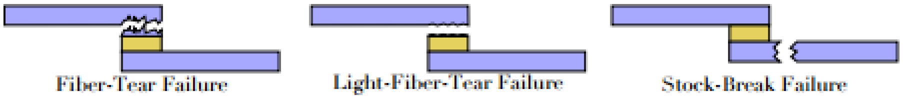

(a) Adherend failure mode from ASTM [225]

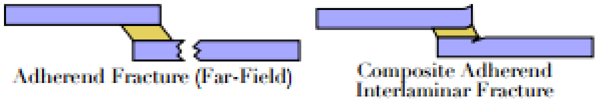

(b) Adherend failure modes from Heslehurst and Hart-Smith [226]

Figure 2-44: Adherend failure modes configuration

2.4.2.3 Methodologies for crack failure investigation

Debonding, delamination, and fractures are the types of cracks while investigating the failure behavior inside the adhesive joints or composite materials. Regarding the objective of the current project, spar cap-shear web debonding, it is necessary to grasp the mainstream methodologies of crack failure analysis and select an appropriate method to investigate the debonding characteristics of a 5-MW blade. Based on the finite element methods, four well-known methodologies are developed to analyze crack failure: continuum mechanics, fracture mechanics, extended finite element method, and damage mechanics [227]. The following literature review focuses on the four mainstream methods' basic concepts, advantages, and disadvantages.

Continuum mechanics

Continuum mechanics is the most frequent and well-known method for material failure analysis. Unlike the other methods using predefined failure criteria concerning the material's critical values to determine whether a material has failed, continuum mechanics compare the maximum values of stress, strain, or strain energy derived from finite element analysis to indicate the damage extent. Continuum mechanics in crack failure analysis has proved effective and with mature development. Nevertheless, it still has some limitations while treating bonded joint failure [228].

Stress-based criteria based on continuum mechanics is a standard selection regarding crack analysis in brittle materials. As an example sketched in Figure 2-45, using continuum mechanics to analyze the plate problem, the exiting crack caused a stress discontinuity at the beginning of the crack tip. The Y-oriented stress near the fracture tip is limited rather than infinite, as predicted by continuum mechanics. Due to free surfaces where crack propagation has already occurred, the Y-stresses decrease near the end of the fracture, which will induce a discontinuity between the crack's head and the remaining crack length. No matter at the crack tip (Figure 2-45) or material interface (Figure 2-45), the stresses need to be continuous. Thus, the crack's stress is infinite, called singularity [228]. The singularity is often present at cracks with smaller than 180 degrees angle and the interface between two bonded materials [229]. Determining stresses depends on the mesh size and the closeness of the stress taken to the singularities. Hence, caution must be used when using critical maximum values, such as maximum principle stresses, as failure criteria. Shear stresses are often used as a failure criterion and to forecast joint strength [230]. The stress-based criteria lack any physical rationale regarding crucial distances from stress singularities. They heavily rely on mesh sizes and other physical characteristics such as adhesive thickness and adherend rounding [228].

While accounting for ductile materials instead of brittle materials, strain-based criteria are more appropriate to analyze crack failure because ductile material can endure large loads during adhesive damage [231]. However, strain-based criteria still suffer the same drawbacks as stress-based. There are other criteria; for example, plastic energy density failure criteria are based on total strain energy and achieve satisfactory results for ductile materials [232]. Moreover, some other criteria were developed for specific situations, for example, to deal with the severe yield loads before failure for some extreme ductile adhesives [233].

The continuum mechanics approach is easy implementation, appropriate for brittle materials, and does not need much criteria information. However, its drawbacks are outstanding, which are unsuitable for discontinuous structures, and ductile materials and highly depend on the meshing quality. Also, the crack cannot be simulated for propagation if no initial crack tip is added.

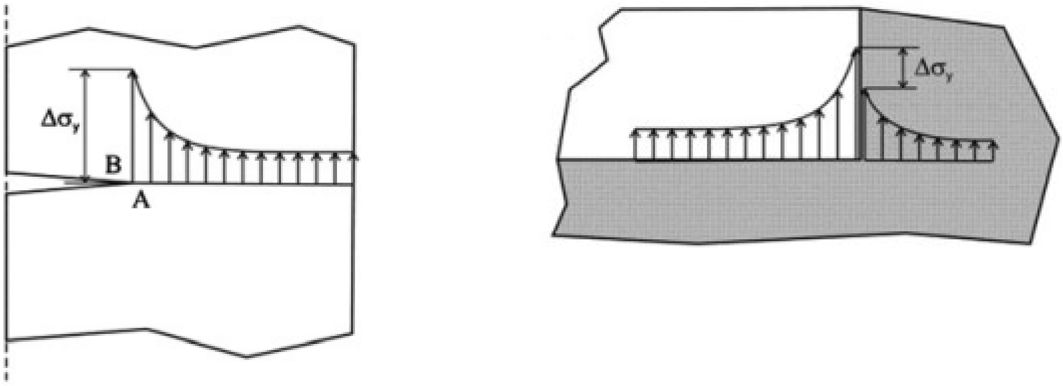

(a) Stress singularity at a crack tip (b) Stress discontinuity at a material interface

Figure 2-45: Stress singularities at crack tips and material interfaces [227]

Fracture mechanics

The continuum mechanics is unsuitable for discontinuous structure problems; also, the stress singularity in this method is infinity which is not valid in the real world. Therefore, researchers develop fracture mechanics to investigate various crack failure modes better. Fracture mechanics generally include Linear Elastic Fracture Mechanics (LEFM), which neglect non-linearity characteristics, and Elasto-Plastic Fracture Mechanics (EPFM), which consider plasticity behaviors [228].

Linear Elastic Fracture Mechanics (LEFM) was initially developed for fracture mechanics, assuming linear-elastic propagated behavior until crack failure in brittle materials. The failure criteria developed by Griffith is the initial one for LEFM to describe the crack propagation once it reaches [234]. Based on Griffith's work, Irwin proposed a "stress intensity factor" to indicate the crack initiation, which used the stress field of the fracture tip within a radius and a small volume around the crack tip [235]. Establishing the stress intensity factor when a fracture spreads near or on a contact surface is difficult. Thus, the strain energy release rate and fracture toughness critical value was developed and widely used in composite materials and adhesive joints [236], [237]. The problem with the LEFM-based method is that it is hard to handle the problems for adhesive joints with complicated geometry. Nevertheless, it performs well for simple bonded joint analysis and is also the theoretical basis of damage tolerance, a widely used design concept in the aircraft industry [228].

Elasto-Plastic Fracture Mechanics (EPFM) is explicitly proposed for ductile materials and considers the plastic behaviors before fracturing, which contradicts LEFM. The initial ideas integrating plasticity in crack behavior used the crack tip opening displacement as a key parameter and a plastic radial or spherical zone that included the fracture [238]. Adjustments and enhancements were performed to enhance the approach by rectifying the actual crack length, the plastic zone, and the assumption that the stress at the boundary is not solitary but zero [239]. With the development of the J-integral, nonlinear fracture mechanics saw a significant advancement [240]. As shown in Figure 2-46, the J-integral is employed as an energy contour line integral. The independent integral route may go from one fracture surface to another while encompassing the crack tip. It estimates the present specific elastic energy stress and strain states at each point along the contour. Owing to the route independence of the integral, the contour may be selected to be circular and connected to the stress intensity factor and energy release rate, which can then be utilized as failure criteria. J-integral has contributed to satisfactory achievement for bonded joints [241], but still with some limitations. J-integral is not suitable for the uncracked joint. Thus, an initial crack tip needs to be assigned and performed analysis. The plastic zone field is limited by adherents and contact surfaces, which leads to the dependence on the joint geometry and interface length [242]. Also, relying on meshing quality often leads to high computational costs and reduced accuracy.

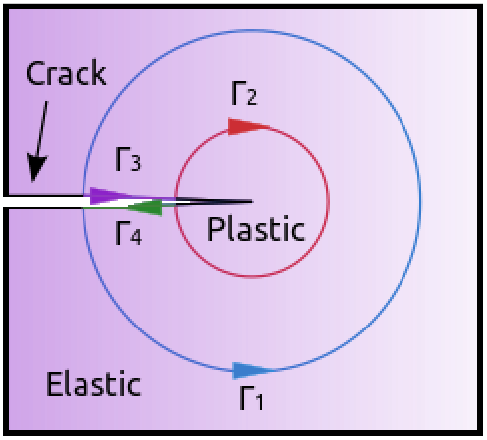

Figure 2-46: Contour of the J-integral around a crack tip[228]

Virtual Crack Closure Technique (VCCT) is another effective crack modeling method for fracture mechanics, initially developed by Rybicki [243]. It is founded on the premise that the energy produced as a crack widens is also the virtual effort necessary to seal the crack back to its original form [244]. Figure 2-47 visualizes the basic concept of VCCT; the coincident nodes are split and employ the energy release rates and critical value, or fracture toughness, to indicate whether the crack is propagated. Using nodal forces and displacements in a finite element model, VCCT computes the current energy release rate for a specific mode, which is the same energy or work necessary to close the crack tip [245]. VCCT can be applied to solid and shell elements in either 2D or 3D crack analysis problems based on plane stress/strain theory, with less computational expense [114]. Nevertheless, due to the method's assumption that nodal forces at nodes along a crack tip route are equal, it is impossible to forecast the initiation and propagation of small cracks [246]. In the wind energy industry, VCCT is still an efficient method to simulate crack problems, especially in blade debonding, as confirmed by several researchers[114], [245], [247].

The fracture mechanics approach is appropriate for the crack failure analysis in brittle and ductile materials with LEFM and EPFM, respectively. However, it needs an initial crack tip to begin the analysis, and it is difficult to simulate the progressive crack propagation. Moreover, the limitation of joint geometry and the dependence on high meshing quality restricts its application in many aspects.

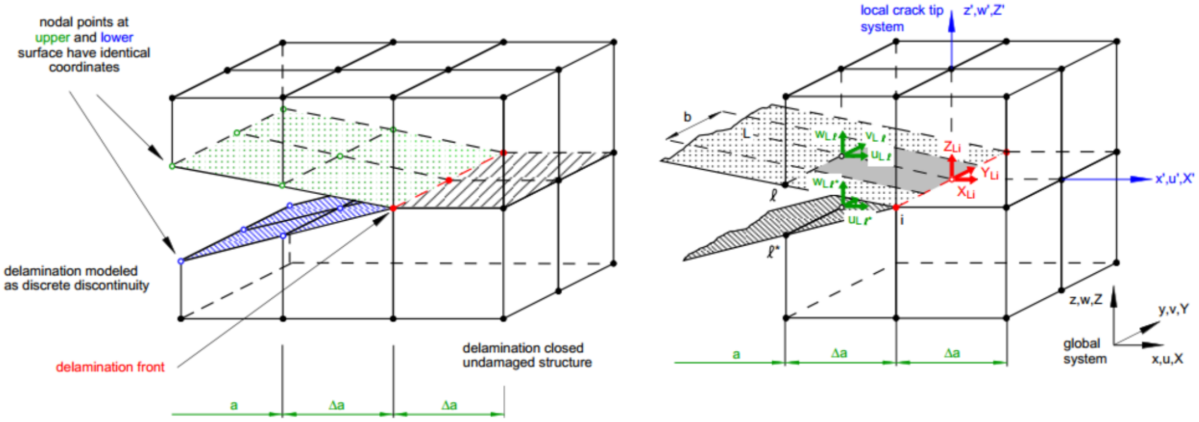

Figure 2-47: Illustration of the VCCT [248]

Extended finite element method

The extended finite element method (XFEM) was first developed in 1999 [249]. It has been embedded in a finite element package for crack propagation modeling and mainly treats linear elastic behavior in the materials [224]. XFEM regards damage initiation and crack propagation, respectively; thus, the criteria and damage laws need to be selected for each stage. Regarding the damage initiation stage, the criteria are usually based on principle stresses or strains; damage law can be according to the average fracture toughnesses or energy release rates and to describe linear or exponential behaviors [228]. After damage initiation happens, phantom nodes confined to existing nodes begin to split, subdividing the elements severed by a crack and mimicking the separation of two newly generated subelements. The phantom and actual nodes then adhere to a damage law until the growth of the crack, so that XFEM do not need require a crack tip or path pre-definition. Therefore, the primary strength of XFEM is to model the arbitrary crack without remeshing, even through different materials, and without needing a pre-defined crack tip or path [250]. Also, XFEM can combine with LEFM and EPFM to analyze crack failure problems for brittle and ductile materials. XFEM has performed well at crack growth simulation under monotonic increasing loading and fatigue loading, showing satisfying agreement with experimental data [251], [252].

However, due to the novelty of XFEM, particularly in finite element software, there have been few applications and simulations, including XFEM and bonded joints. Even though the prominent advantages of XFEM are outstanding, its obvious drawbacks hinder practical application and development and need further investigation [228]. Firstly, the XFEM is not well-developed in finite element packages, such as ABAQUS, where the non-mature functions restrict its application. Secondly, the algorithm of XFEM embedded in software is not mature. It is also highly dependent on the maximum principle stress and strain criteria, making it impossible to deal with mix-mode load conditions, like the tensile and shear combination. Most importantly, XFEM in finite element tools is not working for multiple material structures because existing criteria do not differentiate between various materials or regions, which might result in fracture pathways and sources that are not viable.

Damage mechanics

Damage mechanics track cracks or damage gradually in a limited area, beginning at an arbitrary point or a predefined fracture until structural breakdown. During damage initiation until propagation, damage mechanics allow the crack to grow progressively and consider the stiffness to decrease continuously [253]. The stiffness degradation is used to develop the damage laws, which can be expressed in various methods, including stresses, strain, strain rates, Poisson ratios, and so on [254]. The damage extent inside an element can be indicated by ratios while using damage laws, ranging from 0 to 1, where 0 represents no damage existing, and 1 represents complete damage. Continuum damage mechanics are damage variables utilized in continuum mechanics strategies. Moreover, some failure criteria, such as Tsai-Wu, Puck, or Hashin, can be used accompanied by damage laws [228].

The cohesive zone method (CZM) was developed based on damage mechanics theory, which can be divided into two approaches: local and continuum [228]. The local approach, sometimes named cohesive interface, defines the damage in a finite element region or interface with zero volume or zero area constraint, which works for 2D or 3D crack simulations. Furthermore, the continuum approach, also called the cohesive element method, assigns the damage to the finite element with non-zero volume or area. The cohesive zone method regards the strain energy release rate as the fracture toughness. It combines with the cohesive traction stress to construct the function between the relative displacement and opposing nodes. This function is named constitutive law or traction separation law (TSL). While using the traction law to describe the crack failure, the material starts with elastic behavior and reversible characteristics, and the material stiffness will not decrease within unloading or reloading conditions. After reaching the maximum traction stress, the material becomes irreversible and softening properties; then, the damage begins propagation. The fracture toughness, which the area of the separation-traction law can represent, is pre-defined to control the complete damage stage; once the critical value has been reached, the structure is destroyed. A detailed explanation of the cohesive zone method is offered in 2.4.3.

CZM is a prominent method while investigating crack analysis and probation under static pf fatigue load conditions because of its numerous advantages. As the separation law is the basic principle of CZM, which considers both reversible and irreversible damage behavior, it can retain the crack extent in non-destroyed elements during cyclic loads and bring it to further simulations [255]. The initial crack is not required in CZM to eliminate the pre-defined crack path; furthermore, the crack can propagate randomly in certation regions or even interaction surfaces between two materials like debonding [256]. On the scale of a damaged element, CZM can simulate the crack propagation step-by-step and offer detailed evolution until the element is complete damage. While considering the model and remeshing problem, CZM can accommodate the damage trigger and crack growth in the same model and make the entire analysis in one model [246]. However, CZM still has some drawbacks even though it is already the mainstream technology in damage analysis. Firstly, the meshing quality and sizes directly impact the simulation accuracy; in this case, CZM is inclined to higher computational costs due to the detailed simulation. Another disadvantage is the limitation of different traction laws, which are different for composite, ductile, and other specific materials [228]. As for the debonding problem in a wind turbine blade, the predecessors' achievement has successfully demonstrated the capability and effectiveness of CZM [196], [257]–[259]. Also, compared with the mesh-rely limitation, CZM’s advantages help it become the most prominent method to analyze crack failure for the current industry. It has better application and earnings than VCCT or XFEM. Therefore, CZM is selected to model this project's spar cap-shear web debonding problem, which will be discussed in 2.4.3.

2.4.3 Cohesive zone modeling

2.4.3.1 Concepts of CZM

CZM (cohesive zone method) was created in the 1960s by Dugdale and Barenblatt [260]. After being implemented in a finite element package [261], CZM rapidly becomes a popular technique for simulating crack problems in adhesive joints and solving separation problems under various loading conditions.

The first use of Dugdale and Barenblatt's CZM was to examine the damage progression from a fracture tip under static stresses [239], [262]. Initially, Dugdale only considered the plastic behavior near the crack tip on a small scale and regarded the response as completely linear elastic in a brittle material (Figure 2-48). Based on this theory, Barenblatt improved it by introducing a stress function related to the crack tip displacement (Figure 2-48 (b)). Therefore, the cohesive zone can be defined based on stress functions because they represent the damage behavior of adhesion materials. After the stress function concepts developed, the application and techniques of CZM increased rapidly and helped it become the industry's primary bonded damage analysis method. Various stress functions were proposed afterward to treat specific materials and adhesive materials. The linear relationship between stress (traction) and strain (displacement) proposed by Hillerborg [261] was the first and most fundamental one to implement CZM.

It should be noted that the CZM functioned material separation with applied stress, which is the separation traction law (TSL), to describe the damage failure but not indicate the physical behavior of adhesive materials. Therefore, the shape of TSL in CZM can be different for specific materials but can be determined by three certain parameters. The first one is the fracture energy, which is the area under the TSL shape and represents the energy necessary to split material points completely. The second one is the separation of the damage initiation, and the third one is the maximum separation to indicate that a complete failure happened. These parameters and different TSL shapes will be discussed in 2.4.3.2.

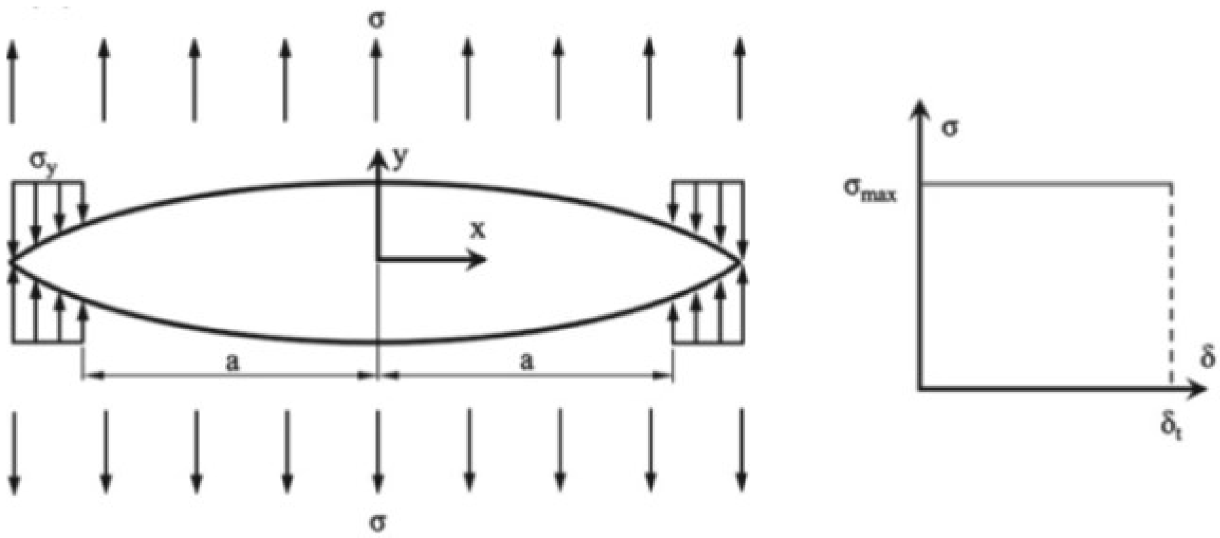

(a) Dugdale’s [239]

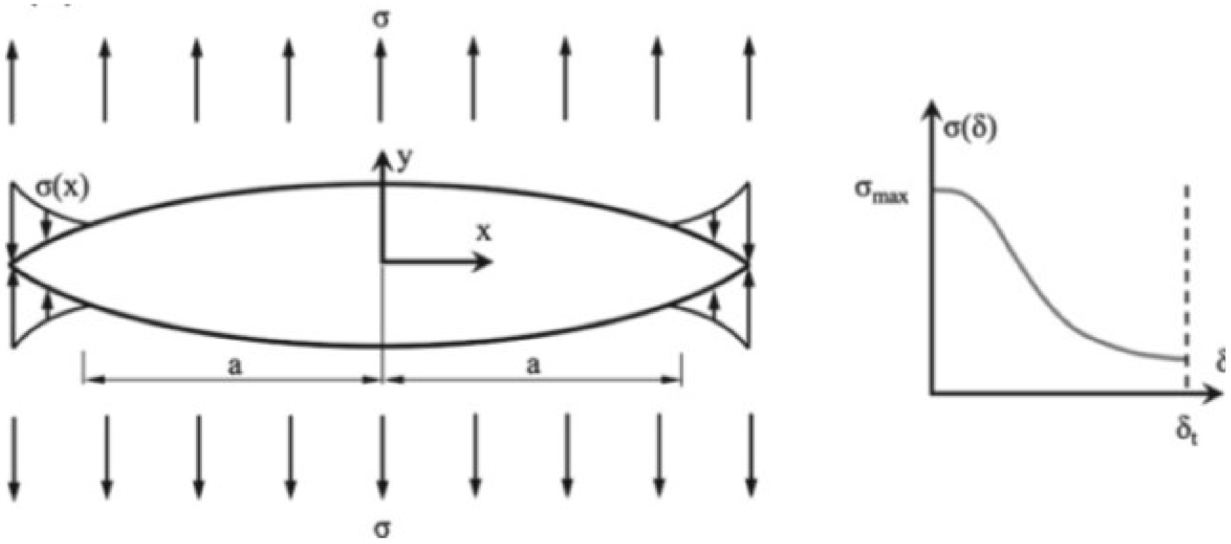

(b) Barenblatt's [262]

Figure 2-48: Two initial cohesive models

2.4.3.2 Traction separation law

The separation traction law represents the relationship between the relative displacement δ between two target points and traction behavior T. The evolution curve is changeable based on different adhesive joints applied; it could be linear, non-linear, continuous, or discontinuous [228].

The specific TSL configuration depends on the separation behavior to be described, but the complete damage evolution comprises two parts. According to Figure 2-49, the damage will be triggered only when the separated displacement reaches the damage initiation point, which is the maximum traction $T_{\max}$. Therefore, the first part of TSL can be described by the interval from zero displacements to the damage initiation point. In this stage, the materials will not sustain any breakage and can restore the original state if unloaded due to their linear-elastic characteristics. The slope of the straight line is the cohesive stiffness. However, if the displacement increases and exceeds the initial damage criterion $T_{\max}$ or δ_C , the damage will initiate and move forward to the second stage of TSL. This phase begins with the damage initiation criterion and grows with the damage propagation criterion, characterized by the energy release rate G_c. The energy release rate, sometimes called cohesive energy, is the energy conversion rate during a material's fracture, which can be calculated by the area formed by the TSL curve and $y = 0$. In general, to define a damaging behavior with CZM, one usually uses the cohesive stiffness k_c to describe the linear-elastic stage, $T_{\max}$ and δ_C for damage-initiated condition, and G_c for propagation criterion. Nevertheless, the example curve above is the basic bilinear TSL concept, often used in brittle materials. Due to the distinguished mechanical properties of different materials, TSL has been extended to various configurations, like the trapezoidal, exponential, polynomial, trilinear, etc. [224], [263]. The two other mainstream TSL types, trapezoidal and exponential TSL, are illustrated in Figure 2-50. Trapezoidal TSL is more suitable for ductile materials, especially for those adhesive materials with large fracture process zone in which bilinear TSL is not correctly [224]. The exponential TSL is employed to treat different adhesive material behaviors, mainly works for shear load conditions, and is especially suitable for materials with plastic characteristics before failure initiation [224]. Regarding the current project, the bilinear TSL was introduced to deal with the cohesive interaction between the spar cap and the shear web, to investigate debonding behavior with a linear-elastic characteristic.

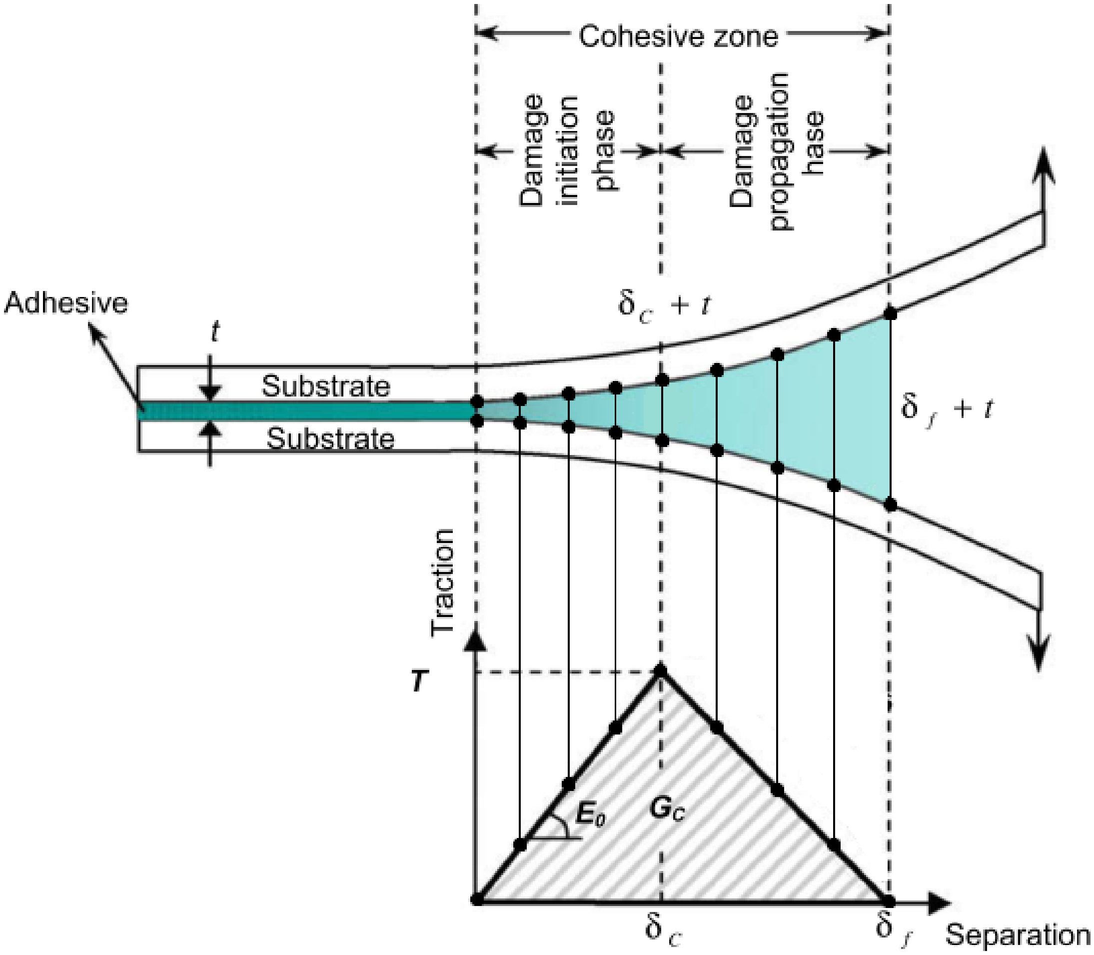

Figure 2-49: Traction separation law for CZM [255]

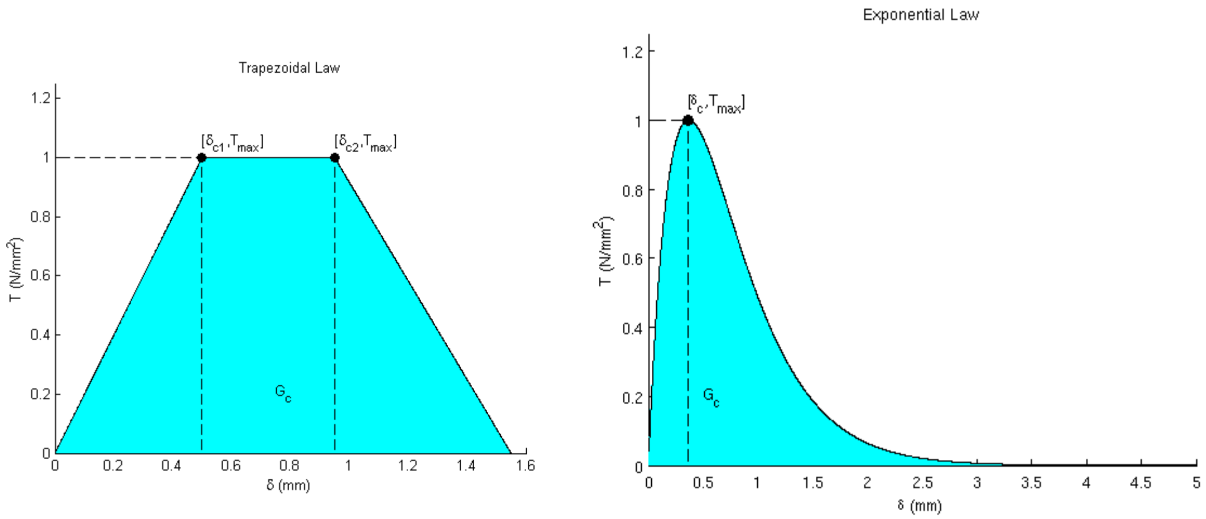

(a) trapezoidal TSL (b) exponential TSL

Figure 2-50: Other shapes of TSL [228]

2.4.3.3 Failure modes of CZM

Based on the traction separation law, the fracture failure mode of a cohesive zone can be divided into three parts in Figure 2-51, normal direction (Mode I), in-plane shear (Mode II), and out-of-plane shear or tear (Mode III). The damage configurations sketched represent the pure delamination modes due to tensile or shear stresses [228].

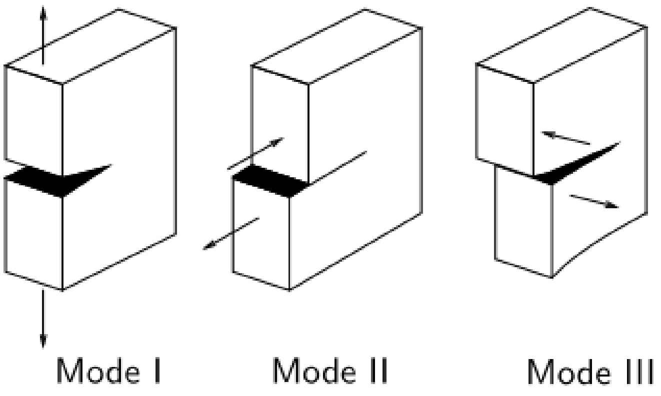

Figure 2-51: Three failure modes in CZM [228]

Nevertheless, the mixed mode is more common in practical damage analysis, which combines normal, shear, and tear damage. Even though the fracture evolution of mixed mode becomes more complicated, it can still be regarded as two stages, damage initiation and damage evolution. In terms of the relationship between stress and strain and based on the traction law, four principles were used to describe the damage initiation criteria of the mixed-mode behavior. They are the maximum nominal stress criterion, maximum nominal strain criterion, quadratic nominal stress criterion, and quadratic nominal strain criterion, which are described in (Eq. 2-26) to (Eq. 2-29), respectively [215]:

Maximum nominal stress criterion

$$\text{Max}\left\{\frac{\langle T_n\rangle}{T_{max,n}},\frac{T_s}{T_{max,s}},\frac{T_t}{T_{max,t}}\right\}=1 \qquad \text{(Eq. 2-26)}$$

Hence, the damage will be triggered when the maximum magnitude among the three nominal stress ratios reaches one value.

Maximum nominal strain criterion

$$\text{Max}\left\{\frac{\langle \varepsilon_n\rangle}{\varepsilon_{max,n}},\frac{\varepsilon_s}{\varepsilon_{max,s}},\frac{\varepsilon_t}{\varepsilon_{max,t}}\right\}=1 \qquad \text{(Eq. 2-27)}$$

This criterion is similar to the previous stress function but uses the strain ratio as the indicator to judge the damage initiation.

Quadratic nominal stress criterion

$$\left(\frac{\langle T_n\rangle}{T_{max,n}}\right)^2+\left(\frac{T_s}{T_{max,s}}\right)^2+\left(\frac{T_t}{T_{max,t}}\right)^2=1 \qquad \text{(Eq. 2-28)}$$

Quadratic nominal strain criterion

$$\left(\frac{\langle \varepsilon_n\rangle}{\varepsilon_{max,n}}\right)^2+\left(\frac{\varepsilon_s}{\varepsilon_{max,s}}\right)^2+\left(\frac{\varepsilon_t}{\varepsilon_{max,t}}\right)^2=1 \qquad \text{(Eq. 2-29)}$$

In the above equations of four damage initiation criteria, *n, s, t* represents the normal, in-plane-shear, and out-of-plane shear (tear) directions. In each direction, T and T_{max} are the traction and maximum traction stresses ε and ε_{max} are the strain and maximum strain with a given constitutive thickness $t=1$. The Macaulay brackets indicate that a pure compressive deformation or stress condition does not result in damage.

As for the criterion in quadratic nominal stress (strain) criterion (QUADS or QUADE), the damage will be initiated when the interaction among three pure modes results in the maximum nominal stress (strain) (MAXS or MAXE) ratio with the value greater than one. While the QUADS/QUADE criteria take concurring quadratic ratios between nominal stress and allowed stress operating in distinct directions into account, the MAXS/MAXE criterion makes no assumptions about the relationships between the various stress directions [264]. The investigation of suitable criterion selection is still limited in the literature. Cui [265] indicated that the non-interactive criteria (MAXS/MAXE) were unsuitable for in-plane delamination problems. Indeed the QUADS/QUADE has been proven effective in multiple aspects [266], [267]. However, many researchers have obtained significant results with maximum stress assumptions [255], [268]–[270]. Therefore, selecting appropriate criteria should be related to the target damage state and refer to the experimental data support.

As for the mixed-mode damage evolution, most criteria are related to the fracture mechanics concepts and the use of the energy release rate to give the function and define the behavior. The two widely-used concepts are power law [271] and Benzeggagh and Kenane Criterion [272], which can be expressed in (Eq. 2-30) and (Eq. 2-31), respectively:

Power law

$$\left(\frac{G_n}{G_{c,n}}\right)^{\alpha_c}+\left(\frac{G_s}{G_{c,s}}\right)^{\alpha_c}+\left(\frac{G_t}{G_{c,t}}\right)^{\alpha_c}=1 \qquad \text{(Eq. 2-30)}$$

Where G_n, G_s, G_t are the fracture energy in normal, shear and tear directions, whereas the $G_{c,n}$, $G_{c,s}$, $G_{c,t}$ represent the critical energy release rate. α_c is the empirical coefficient.

Benzeggagh and Kenane (BK)

$$G_{c,n}+\left(G_{c,s}-G_{c,n}\right)\left\{\frac{G_S}{G_T}\right\}^{\eta}=G_C \qquad \text{(Eq. 2-31)}$$

Where G_C is the total mixed-mode fracture energy, $G_S = G_s + G_t$, $G_T = G_n + G_S$, and η is the exponential factor. BK is especially suitable for failure problems where the pure crack growth of in-plane and out-of-plane shear are the same. Figure 2-52 is a mixed-mode example considering the normal and in-plane shear damage deformation based on BK theory, reflecting the resultant traction law on the three-dimensional scale [273].

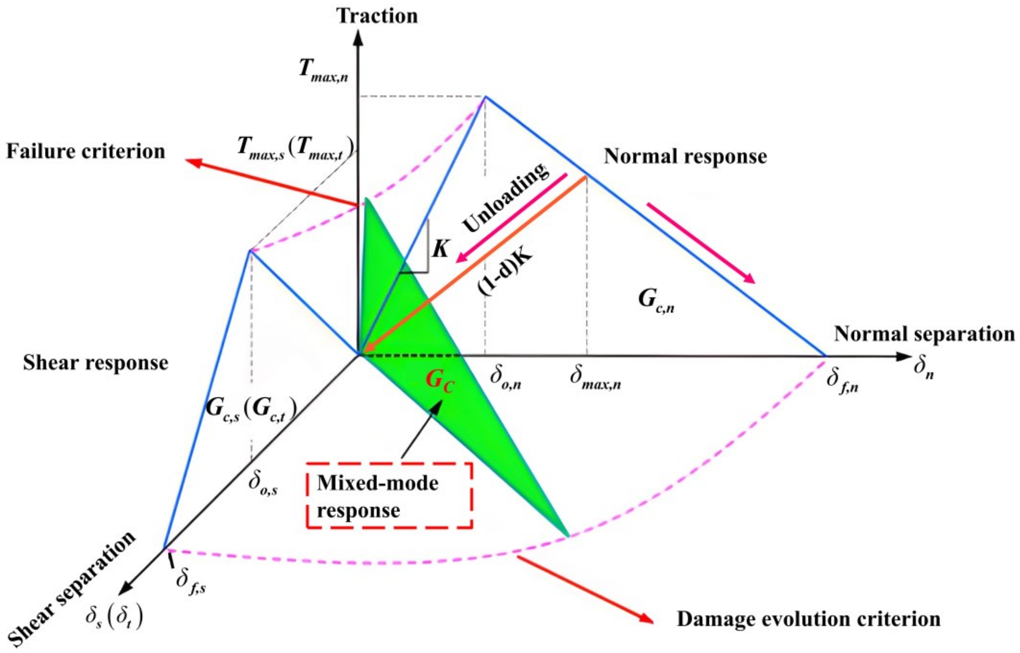

Figure 2-52: Mixed-mode using BK theory [273]

CHAPTER 3: NREL 5-MW WTB MODELING AND VERIFICATION

3.1 Geometrical model

The NREL 5-MW blade [84], which is treated as a benchmark WTB by many previous researchers [274]–[277], is considered in this study. The selected blade has a 61.5 m span (Figure 3-1), where the span was divided into 38 stations and scheduled with seven different airfoil types, where the maximum chord length is 4.652 m at the 17th station, and a circular cylinder airfoil with a diameter of 3.386 m is designed at the root for higher load-carrying capability. The seven types of airfoil distribution in the spanwise direction for the 5-MW blade are summarized in

Table 3-1, with the respective profile in Figure 3-2. The NACA 64-series airfoil is assigned in the final one-third of the blade span. For two-thirds of the forward blade, the DU family of airfoils are given sequentially along the span regarding the thickness to chord (*t/c*) ratios, which compare the maximum vertical thickness of an airfoil to its chord length.

Two shear webs (Figure 3-1 (b)) are constructed to form the inside structure, reduce the unsupported airfoil shell length, and offer extra structural stability. The pre-defined shear webs can determine the distribution of the spar cap, resulting in a “box” design that resists buckling and avoids severe chordwise thickness declines. In the spanwise direction, the shear webs range from 1.3667m to 60.1333m. However, the NREL does not offer sufficient data to determine the chordwise position's precise coordinates. The shear web parameters in Table 3-2 refer to Herrema’s 5-MW blade modeling work [278], [279], which used a chordwise ratio to clarify the exact shear webs position for each airfoil along the entire 5-MW blade span.

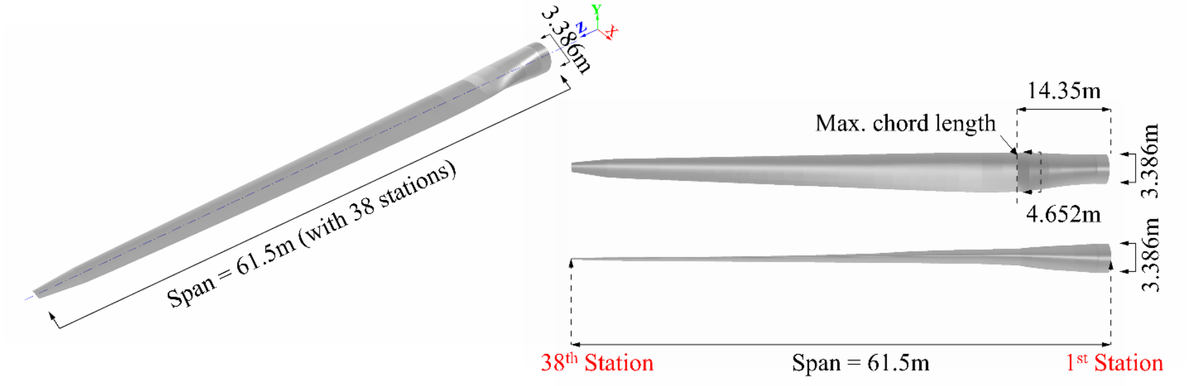

(a) Geometry configuration of NREL 5-MW blade

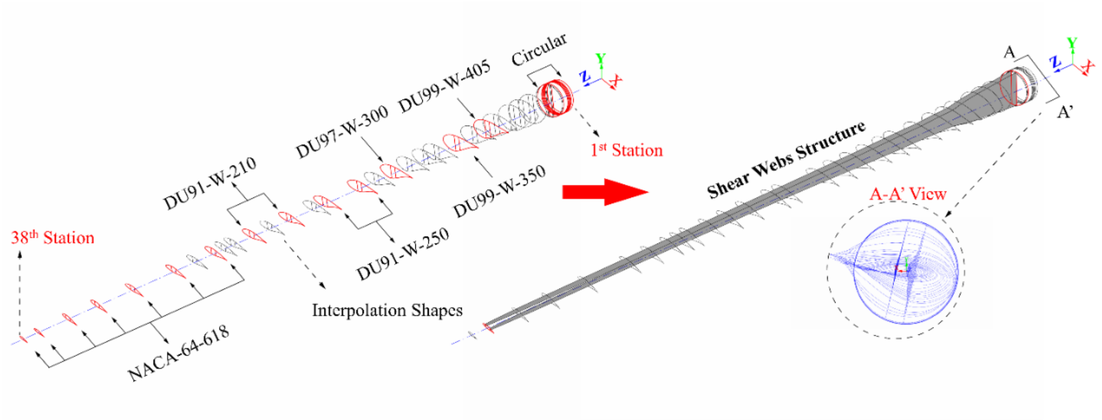

(b) The spanwise airfoil schedule and shear web structure

Figure 3-1: Geometrical model of the 5-MW blade

Table 3-1: Airfoil schedule along the 5-MW blade span

No.	Airfoil type	Blade section name	Thickness (*t*/*c*)	Begin radius (m)
1	Cylinder	Circular	100%	0
2	DU40_A17	DU W-405	40.50%	10.25
3	DU35_A17	DU W-350	35.09%	14.35
4	DU30_A17	DU 97-W-300	30%	22.55
5	DU25_A17	DU 91-W2-250	25%	26.65
6	DU21_A17	DU 91-W-210	21%	34.85
7	NACA64_A17	NACA 64-618	18%	43.05

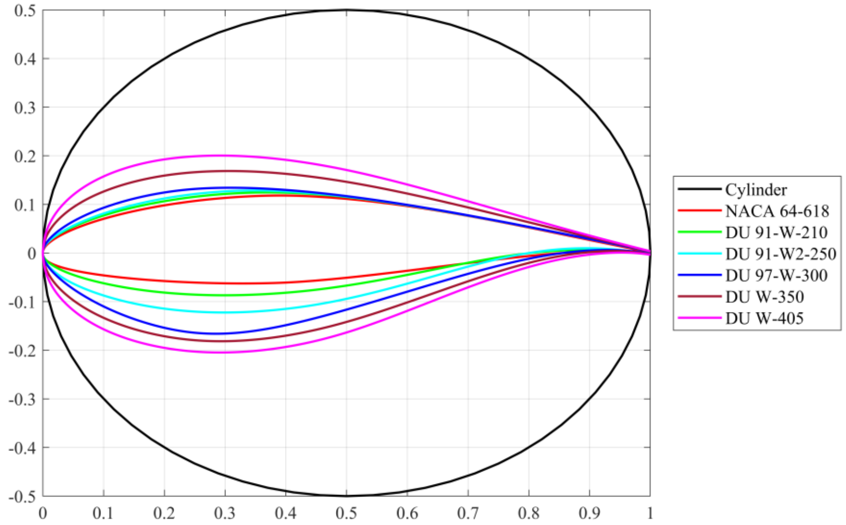

Figure 3-2: Specific airfoils configuration for 5-MW blade

The seven kinds of airfoil in

Table 3-1 are insufficient for smooth thickness distribution. In order to avoid sudden ply drop, some intermediate stations are introduced. Unlike Resor [84] and Griffith [94] using NuMAD [218] for interpolated stations, an open-source software named QBLADE [280] is used for this project. Miao [281] created the 2D coordinators for the transition forms using QBLADE, and the rebuilt blade model, which has shown satisfactory agreement with the NREL version. Therefore, the transition shapes are interpolated by QBLADE in this project.

Then different airfoils are distributed at each station, including the input of airfoil coordinators, chord length, twist angle, and pitch axis position. The detailed geometrical information from NREL [84] about the 5-MW blade is listed in Table 3-2.

Table 3-2: Geometrical details of the NREL 5-MW wind turbine blade

No.	Location (m)	Airfoil	*t/c* (%) (thickness/chord)	Twist (deg)	Chord (m)	Pitch Axis	SW1	SW2
1	0	Cylinder	100.00	13.31	3.39	0.5	0.4114	0.5886
2	0.3	Cylinder	100.00	13.31	3.39	0.5	0.4114	0.5886
3	0.4	Cylinder	100.00	13.31	3.39	0.5	0.4114	0.5886
4	0.5	Cylinder	100.00	13.31	3.39	0.5	0.4114	0.5886
5	0.6	Cylinder	100.00	13.31	3.39	0.5	0.4114	0.5886
6	0.7	Cylinder	100.00	13.31	3.39	0.5	0.4114	0.5886
7	0.8	Cylinder	100.00	13.31	3.39	0.5	0.4114	0.5886
8	1.3667	Cylinder	100.00	13.31	3.39	0.5	0.4114	0.5886
9	1.5	interp	99.11	13.31	3.39	0.4985	0.4102	0.5868
10	1.6	interp	98.44	13.31	3.39	0.4974	0.4094	0.5854
11	4.1	interp	81.69	13.31	3.63	0.4692	0.3876	0.5508
12	5.5	interp	72.32	13.31	3.87	0.4535	0.3755	0.5315
13	6.8333	interp	63.38	13.31	4.12	0.4385	0.3639	0.5131
14	9	interp	48.87	13.31	4.46	0.4141	0.3450	0.4831
15	10.25	DU99-W-405	40.50	13.31	4.56	0.4	0.3342	0.4658
16	12	interp	38.19	12.53	4.62	0.4	0.3313	0.4687
17	14.35	DU99-W-350	35.09	11.48	4.65	0.4	0.3274	0.4726
18	17	interp	33.45	10.68	4.58	0.4	0.3230	0.4770
19	18.45	interp	32.55	10.16	4.51	0.4	0.3206	0.4794
20	20.5	interp	31.27	9.63	4.37	0.4	0.3172	0.4828
21	22.55	DU97-W-300	30.00	9.01	4.25	0.4	0.3138	0.4862
22	24.6	interp	27.50	8.40	4.13	0.4	0.3104	0.4896
23	26.65	DU91-W-250	25.00	7.79	4.01	0.4	0.3070	0.4930
24	30.75	DU91-W-250	23.00	6.54	3.75	0.4	0.3003	0.4997
25	32	interp	22.39	6.18	3.67	0.4	0.2982	0.5018
26	34.85	DU93-W-210	21.00	5.36	3.50	0.4	0.2935	0.5065
27	37	interp	20.48	4.75	3.37	0.4	0.2899	0.5101
28	38.95	DU93-W-210	20.00	4.19	3.26	0.4	0.2867	0.5133
29	41	interp	19.50	3.66	3.13	0.4	0.2833	0.5167
30	42	interp	19.26	3.40	3.07	0.4	0.2817	0.5183
31	43.05	NACA-64-618	19.00	3.13	3.01	0.4	0.2799	0.5201
32	45	interp	18.52	2.74	2.89	0.4	0.2767	0.5233
33	47.15	NACA-64-618	18.00	2.32	2.76	0.4	0.2731	0.5269
34	51.25	NACA-64-618	18.00	1.53	2.52	0.4	0.2664	0.5336
35	54.6667	NACA-64-618	18.00	0.86	2.31	0.4	0.2607	0.5393

36	57.4	NACA-64-618	18.00	0.37	2.09	0.4	0.2562	0.5438
37	60.1333	NACA-64-618	18.00	0.11	1.42	0.4	0.1886	0.6114
38	61.5	NACA-64-618	18.00	0.00	1.09	0.4	0.1236	0.6764

Note: “Interp” in Figure 3-2 represents the transition shape scheduled at a specific station developed by QBLADE [118], which benefits smooth thickness distribution along the span. The Pitch axis sometimes acts as the blade reference axis, where the ratio represents the amount the aerodynamic center occupied in the chordwise direction. “SW1” and “SW2” indicate the chordwise ratio of the two shear webs, respectively.

3.2 Finite element model

A shell-continuum shell coupled model is built in ABAQUS to reproduce the dynamic characteristics of the NREL 5-MW blade considered. The shell elements (S4R) are used to model the blade skin, and continuum shell elements (SC8R) are assigned for shear webs, respectively, allowing the adhesion joint between the skin and the web to be modeled as the cohesive interface using the CZM discussed in 2.4.3. A schematic view of the FE model for the WTB is shown in Figure 3-3. The element size is selected with a consistent 0.35 m for the entire model, and the blade root area is fixed in ABAQUS to model the rotor-mounted scenario.

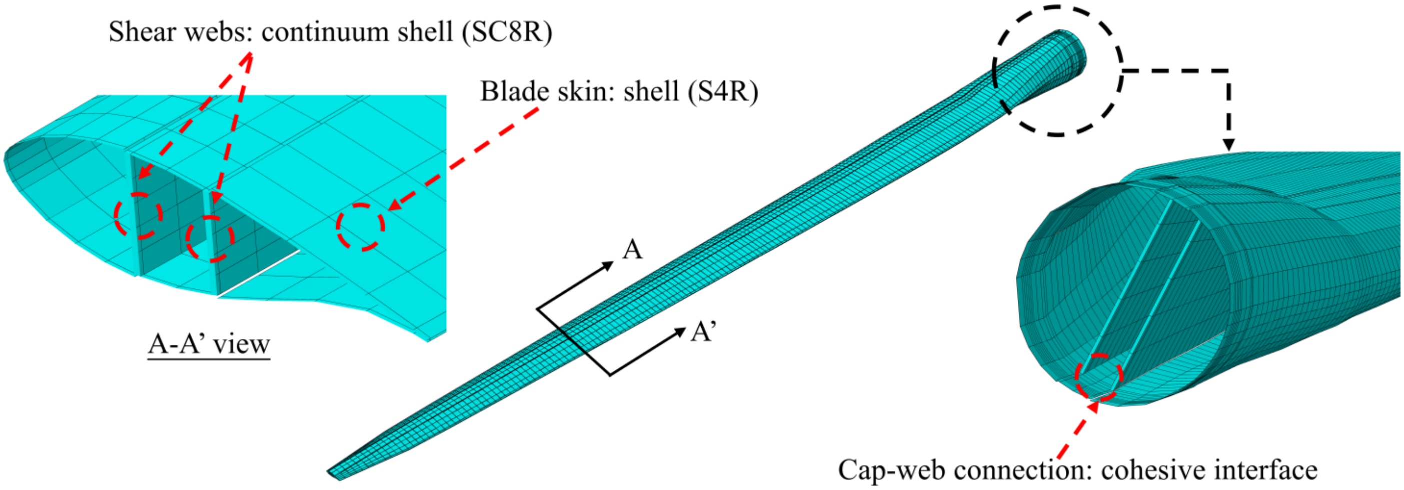

Figure 3-3: Meshing of 5-MW blade with the cohesive connections between the spar cap and shear webs

The cohesive connections are defined at four target contact surfaces between the spar cap and shear webs, as illustrated in Figure 3-4. Thus, it can be denoted with LE-BOT, LE-TOP, TE-BOT, and

TE-TOP, respectively. Here, LE & TE represent the leading edge & trailing edge, and BOT & TOP indicate the bottom & top surface, respectively.

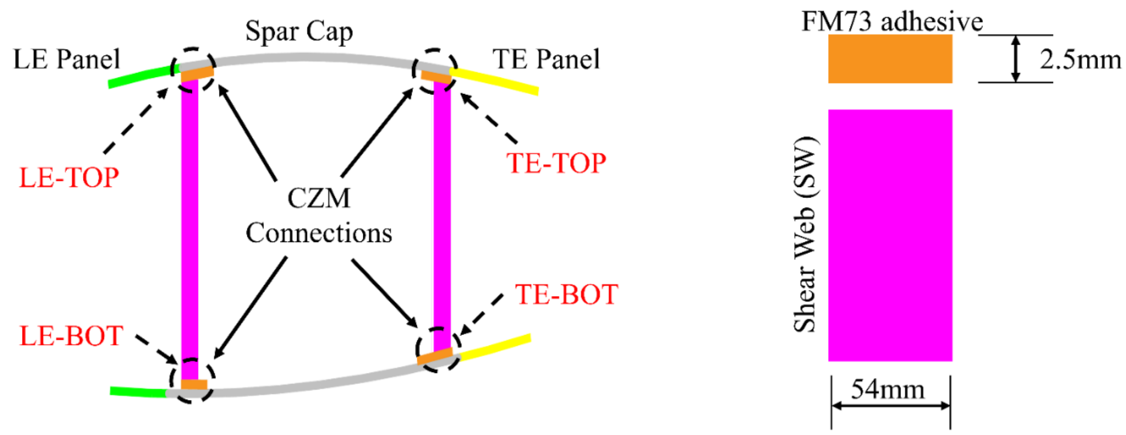

Figure 3-4: Adhesive connections between the spar cap and shear webs

Table 3-3: Material properties of FM73 adhesive [255], [282]

Properties		FM73 adhesive
Thickness t (mm)		2.5
Longitudinal modulus E_1 (GPa)		1.1
In-plane shear modulus G_{12} (GPa)		0.382
In-plane Poison's Ratio υ_{12}		0.44
Density (g/cm^3)		1.2
Traction stress (MPa)	Normal (peeling)	66
	Shear (I,II)	114
Fracture energy (kJ/m^2)	Normal (peeling)	1.4
	Shear (I,II)	2.8
Cohesive stiffness (N/m^3)	Normal K_{nn}	$4.4*10^{11}$
	Shear (I,II) $K_{ss(tt)}$	$1.528*10^{11}$

Note: shear (I, II) represents the in-plane and out-of-plane shear, respectively.

The FM 73 adhesive, a widely used bonding material in wind turbine blades, is considered the adhesive material between the spar cap and shear webs, with pertinent parameters summarized in Table 3-3. Note that the thickness of 2.5 mm is not explicitly modeled but used to calculate the cohesive stiffness K_{nn} and $K_{ss(tt)}$ defined by T_m/δ_c (traction divided by separation, with the unit N/m^3) for the cohesive interface. In order to characterize the cohesive failure in blade debonding, the proper beginning criteria of the maximum nominal stress criterion (MAXS) is selected, as discussed earlier. As for the damage evolution in the second stage, Benzeggagh-Kenane (BK) law is employed with the coefficient $\eta=2$ [255]. Moreover, viscous damping is used to reduce the simulation instability and achieve complete damage behavior, with a usually adopted value (10^{-5} N s/mm) [255], without impacting the simulation accuracy.

3.3 Composite material arrangement

3.3.1 Material properties

Wind turbine blades are mainly made of lightweight and high-strength composite fiber materials, which allow the structural weight to be drastically reduced without sacrificing material strength [283]. The composite material arrangement of the WTB is from the original database provided by NREL [84]. Table 3-4 summarises the material used for the 5-MW blade, including the thickness, composite layers, and material properties. Multiple laminate layers stack a specific composite material (e.g., Saertex) with specific orientations (e.g., $[\pm45]_4$ for Saertex layup).

Table 3-4: Material properties used in the NREL 5-MW blade model

Material	Layer Thickness	Layup	E_1	E_2	G_{12}	v_{12}	ρ	UTS	UCS
	(mm)	(-)	(GPa)	(GPa)	(GPa)	(-)	(kg/m^3)	(GPa)	(GPa)
Gelcoat	0.05	NA	3.440	3.440	1.323	0.30	1235	-	-
E-LT-5500	0.47	$[0]_2$	41.80	14.00	2.630	0.28	1920	0.972	0.702
SNL Triax	0.94	$[\pm45]_2[0]_2$	27.70	13.65	7.200	0.39	1850	0.700	-
Saertex	1.00	$[\pm45]_4$	13.60	13.30	11.80	0.49	1780	0.144	0.213
FOAM	1.00	NA	0.256	0.256	0.022	0.30	200	-	-
Carbon (UD)	0.47	$[-45]_2[+45]_2[0]_{23}$	114.5	8.390	5.990	0.27	1220	1.546	1.047

Note: E_1 and E_2 are Young's modulus in the first (longitudinal) and second (transverse) material directions. G_{12} is the shear modulus. ν_{12} is the Poisson's ratio. ρ is the density. UTS is the ultimate tensile strength (longitudinal direction). UCS is the ultimate compressive strength (longitudinal direction).

3.3.2 Material distribution

Before distributing the composite layers for the 5-MW blade in Abaqus, the mapping of stacks is defined with the designated stack ID provided in Table 3-5 for each material in Table 3-4. In Table 3-5, "SW" stands for the shear web made from exterior Saertex (DB) and interlayer Foam. "Triax" refers to using triaxial composite material, which has been particularly assigned at the root area to strengthen the buckling resistance and distributed on exterior and interior skin for the entire span. "UD" is an abbreviation for "Uni-directional," UD Carbon and UD E-LT-5500 are adopted for spar cap and trailing edge reinforcement, where the airfoil cross-section with specified regions is shown in Figure 3-5.

Table 3-5: Mapping of stacks and materials

Stack ID	Stack Name	Material
1	Gelcoat	Gelcoat
2	Triax Skins	SNL(Triax)
3	Triax Root	SNL(Triax)
4	UD Carbon	UD Carbon
5	UD Glass TE	E-LT-5500(UD)
6	TE Foam	Foam
7	LE Foam	Foam
8	SW Skins	Saertex(DB)
9	SW Foam	Foam

The chordwise airfoil profile is separated into several material zones to arrange different material usage, as illustrated in Figure 3-5 for station # 13 as an example, denoted by LE (leading edge), LE panel, SW1 (forward shear web), the spar cap, SW2 (aft shear web), TE (trailing edge) panel, TE REINF (reinforcement), and TE, respectively. Some material zones' chordwise length remains constant throughout the blade span, including LE (100 mm), spar cap (600 mm), TE REINF (400 mm), and TE (100 mm). Hence, the geometry of the other material zones can be mathematically defined by the specific chord length and situated station. And the exact composite layer arrangement for different material regions was sketched in Figure 3-6.

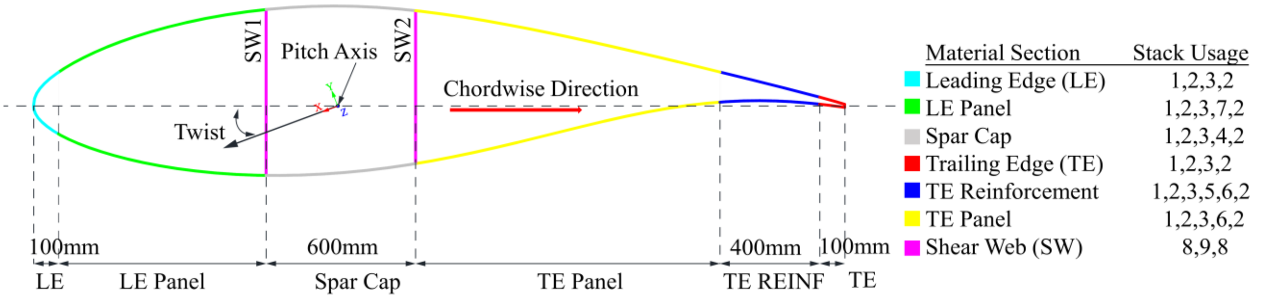

Figure 3-5: Material zone definition for Station # 13 of the 5-MW blade in the chordwise direction

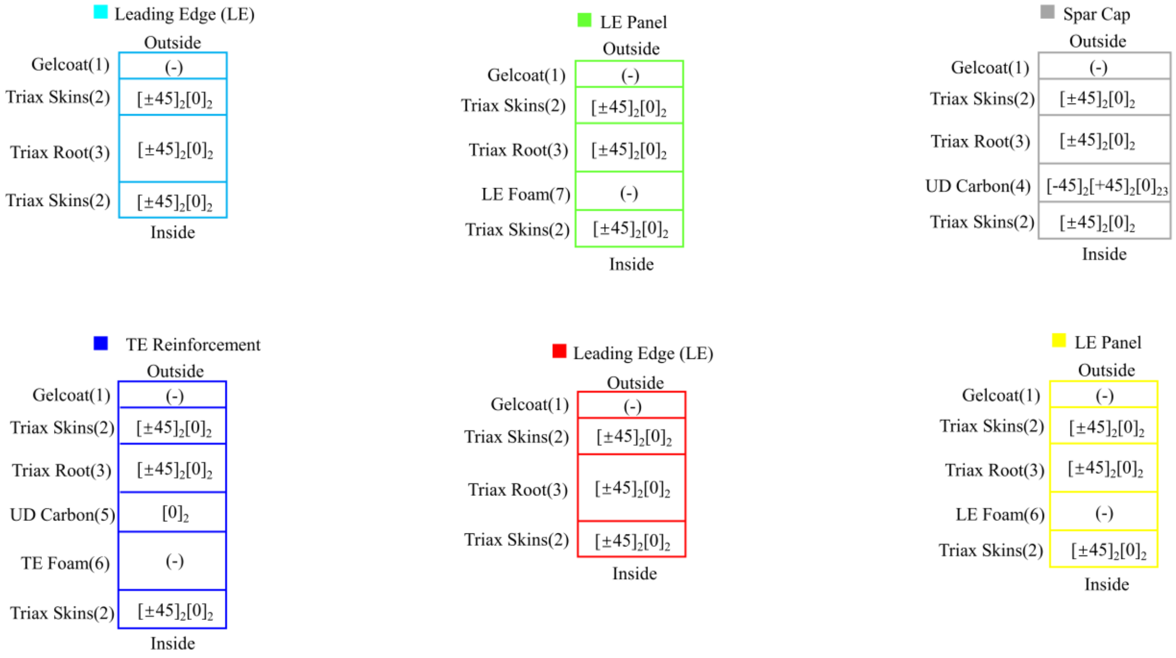

Figure 3-6: Stack sequence for different material zones

In the spanwise direction, the composite layer design varies with the stack ID sequence summarized in Table 3-6 for eight certain stations, while the remaining thirty stations can be determined by linear interpolation according to the number of layers along the span, as shown in

Figure 3-7. Therefore, the exact thickness of each composite material in Table 3-4 can be calculated by the layer numbers and the corresponding layer thickness. The blade is not entirely manufactured from orthotropic materials. A Gelcoat with 0.05 mm thickness is applied to the whole span's outer surface, and Foam is inserted as an interlayer in panels and webs. Thus, the values in Figure 3-7 for these two isotropic materials mean the imposed thickness because they cannot be counted by layer number.

Table 3-6: Stack sequences for different zones of the blade model

Station #	Location (m)	TE	TE_REINF	TE_Panel	Spar Cap	LE_Panel	LE	Shear Webs
1	0	1,2,3,2	1,2,3,2	1,2,3,2	1,2,3,2	1,2,3,2	1,2,3,2	/
8	1.3667	1,2,3,2	1,2,3,2	1,2,3,2	1,2,3,2	1,2,3,2	1,2,3,2	8,9,8
9	1.5	1,2,3,2	1,2,3,5,6,2	1,2,3,6,2	1,2,3,4,2	1,2,3,7,2	1,2,3,2	8,9,8
13	6.8333	1,2,3,2	1,2,3,5,6,2	1,2,3,6,2	1,2,3,4,2	1,2,3,7,2	1,2,3,2	8,9,8
14	9	1,2,2	1,2,5,6,2	1,2,6,2	1,2,4,2	1,2,7,2	1,2,2	8,9,8
31	43.05	1,2,2	1,2,5,6,2	1,2,6,2	1,2,4,2	1,2,7,2	1,2,2	8,9,8
32	45	1,2,2	/	1,2,6,2	1,2,4,2	1,2,7,2	1,2,2	8,9,8
38	61.5	1,2,2	/	1,2,2	1,2,2	1,2,2	1,2,2	8,9,8

Note: from left to right, the stack sequence starts from the outer blade skin to the internal surface

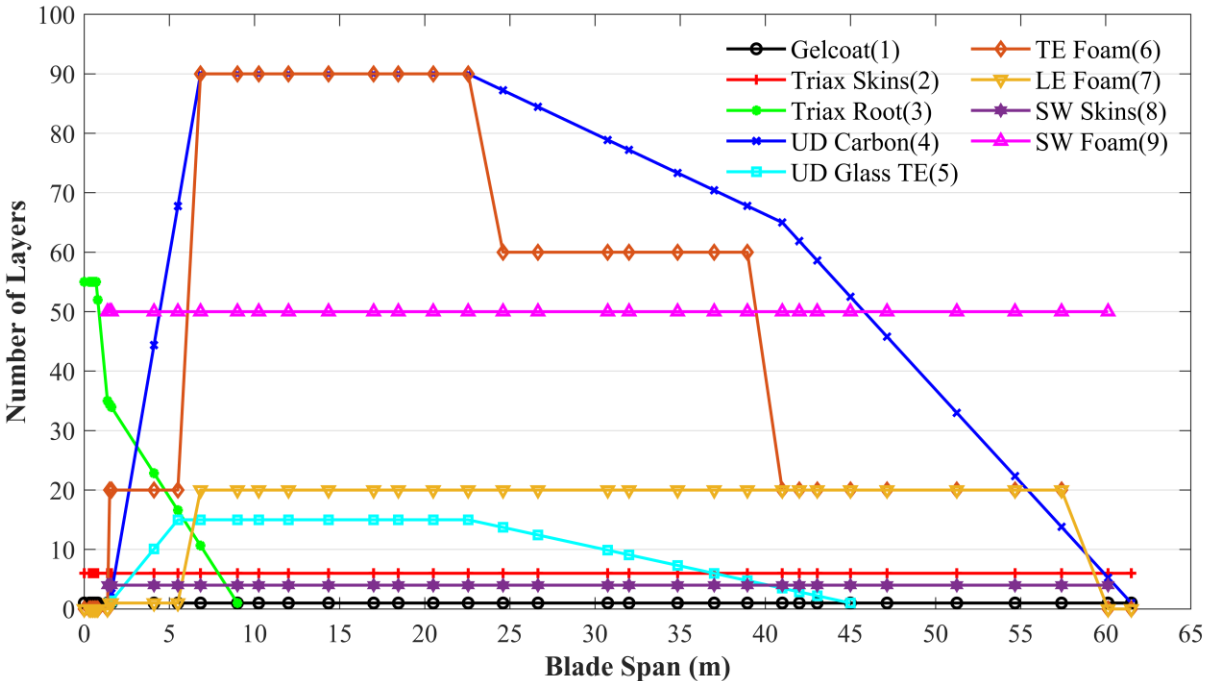

Figure 3-7: The total number of layers for each stack along the 5-MW blade span

The material selection, characteristics, and laminate scheduling are outlined previously; however, several 5-MW blade researchers employed different ways to spread the composite layers. For example, Miao [281] replicated the 5-MW blade model using the outside surface as the reference plane. For the material arrangement work in the current project, the bottom surface is selected as the spar cap's reference plane to insert the cohesive interface between the spar cap and shear web, as sketched in Figure 3-8. For the other blade outside skins, the middle reference plane is adopted. Nevertheless, the current modeling strategy requires the geometric offsets between the spar cap and adjacent panels in the model (see Figure 3-8) to be corrected by tie constraints.

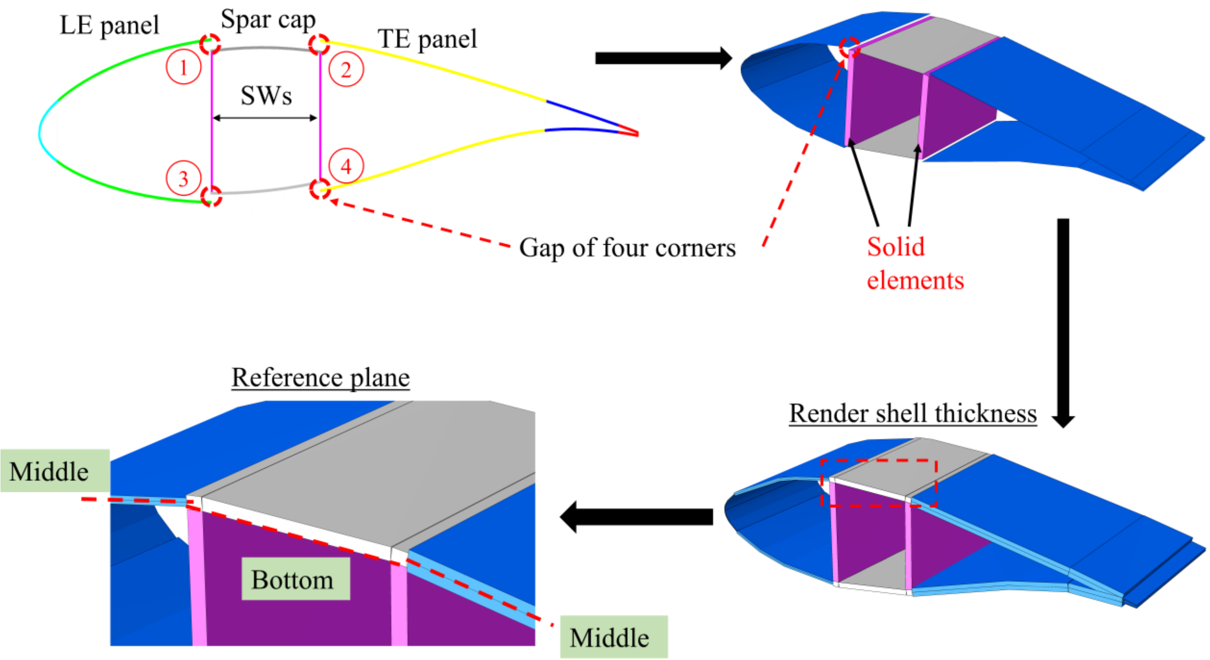

Figure 3-8: Reference plane usage for the spar cap and the other material regions

Due to the anisotropic qualities of composite materials, the fiber direction must be appropriately defined in ABAQUS. General types of fiber orientation in composite materials include unidirectional, biaxial, triaxial, and random. The first three types are the majority laminate orientation for the spar cap, shear webs, and other regions in WTBs [283]. On a scale of degree orientation, fibers are typically orientated to 0°, +45°, and -45°, where 0° corresponds to the pitching axis or blade span direction [284]. The 0° plies are responsible for flap-wise stiffness, while the 45° fibers offer torsional stiffness and buckling resistance [285], [286]. As an example of fiber assignment in Figure 3-9, the stack utilization of the trailing edge from 37 m to 38.5 m is 1,2,3,2 (see Table 3-6). Since Gelcoat is isotropic, it has only a 0° orientation relative to the "1" reference axis, the spanwise direction in the ABAQUS specification. Triax Skins plies with $[\pm 45]_2[0]_2$ are alternately scheduled from the outside to the inside surface.

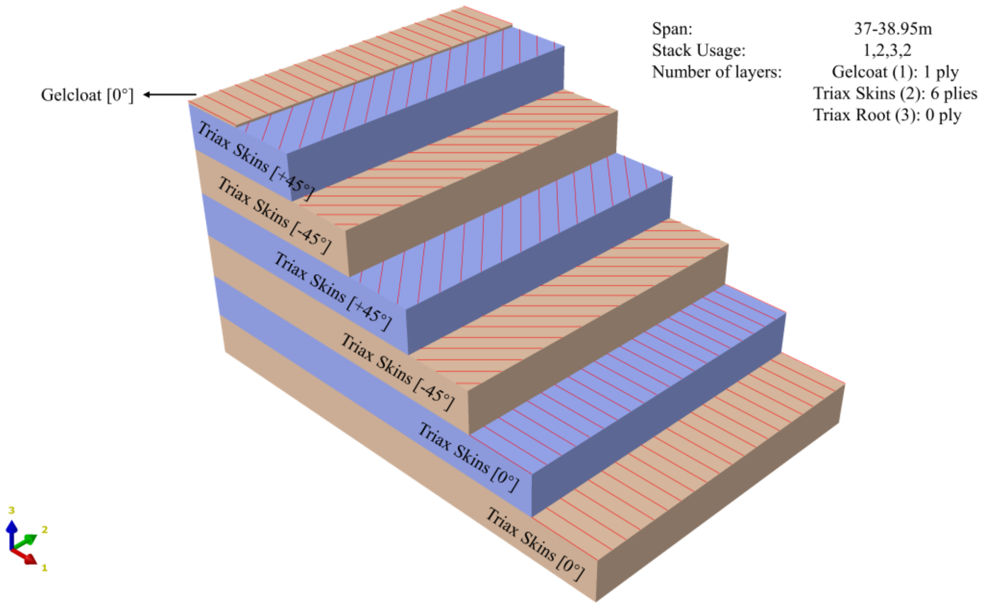

Figure 3-9: Stack plot for trailing edge with a span of 37-38.95m

3.4 Model verification

For the purpose of vibration simulation of WTBs, the model is verified with the reference data [84] in terms of mass properties and vibration properties (e.g., frequencies, mode shapes) obtained from eigenvalue analysis. The analysis results show that the 5-MW blade model developed captures the dynamic properties well, with the comparison summarized in Table 3-7 and the first six modal shapes illustrated in Figure 3-10. Note that the sixth mode is the first torsional mode, which has the largest difference, attributed to the lack of detailed information on the shear web locations.

This is considered acceptable in this study because the vibration simulation (e.g., free vibration and hammer testing) mainly excites the flapwise or edgewise behavior of the blade, and dynamics responses will be compared between the WTB with and without debonding damage.

Table 3-7: 5-MW blade model verification with reference data

Mode #		Ref (Hz)	5-MW blade model in Abaqus	
			Freq (Hz)	Diff (%)
1	1st flapwise	0.87	0.866	0.432%
2	1st edgewise	1.06	1.043	1.632%
3	2nd flapwise	2.68	2.682	0.063%
4	2nd edgewise	3.91	3.890	0.517%
5	3rd flapwise	5.57	5.630	1.081%
6	1st torsion	6.45	6.940	7.597%
	Mass (kg)	17740	17961	1.245%
	Mass center location (m)	20.47	20.58	0.537%

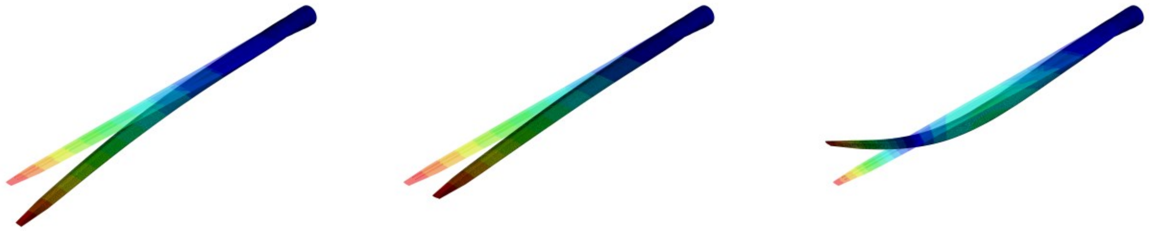

(a) 1st flapwise (b) 1st edgewise (c) 2nd flapwsie

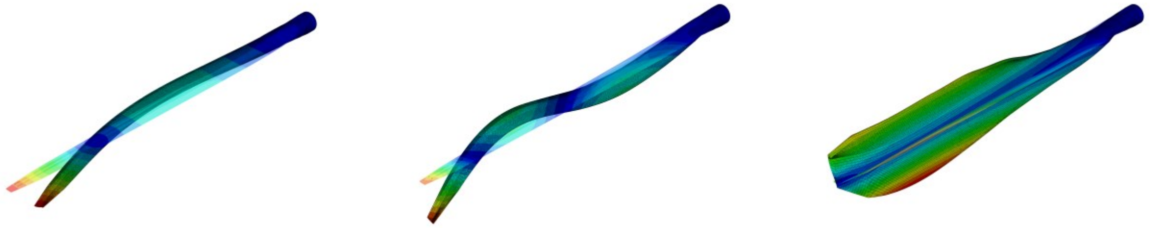

(d) 2nd edgewise (e) 3rd flapwise (f) 1st torsion

Figure 3-10: The first six modal shapes of 5-MW Blade

CHAPTER 4: DEBONDING HOTSPOT ANALYSIS

CHAPTER #3 has described the intact blade FE model using shell-continuum shell coupled elements in ABAQUS, and the model has been verified in terms of vibration characteristics (e.g., frequencies and modes). Most research about debonding problems in wind turbine blades only considers simple loading conditions, such as the bending test [16], [18]. However, a rotating blade suffers from complicated aerodynamic loads. Consequently, it is more realistic to investigate debonding potential and behaviors by applying operational aerodynamic forces to the WTB. This will lead to better knowledge about the debonding hotspot area in the adhesive connection between the spar cap and shear webs. Thus, in CHAPTER #4, the main task is to identify the hotspot area for spar cap-shear web debonding under aerodynamic loads, then demonstrate the debonding area propagation for a pre-existing crack in the hotspot area.

4.1 Identification of the hotspot for cap-web debonding with aerodynamic loads

4.1.1 Aerodynamic loads calculation

AeroDyn [136] is used to calculate aerodynamic loading for the NREL 5-MW WTB; this software is embedded in OpenFast provided by NREL [219] and based on Blade Element and Momentum Theory. The airflow loads applied on the wind turbine blade can be divided into lifting and dragging. These two forces are influenced by wind velocity, airfoil profiles, yaw axis, and other wind turbine design parameters illustrated in Figure 4-1 [287]. The overhang is the distance from the yaw axis to the rotor apex for the three-blade turbine, and the blade cone angle is precone. The exact design parameters provided by Jonkman [219] for the 5-MW blade, as summarized in Table 4-1, are used in AeroDyn to calculate aerodynamic loadings. The specified wind speed of 11.4 m/s, which indicates the wind turbine's highest-rated output and represents the usual operating circumstances of a functioning blade on-site, and a more stringent cut-out wind speed of 25 m/s, are selected for determining the aerodynamic loads.

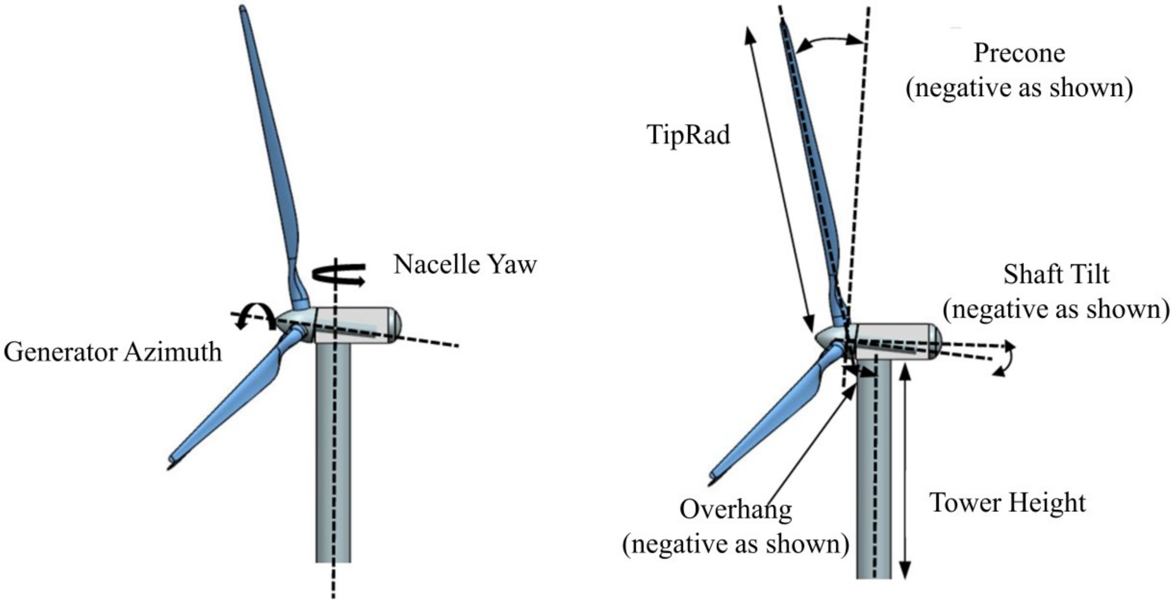

(a) (b)

Figure 4-1: Configuration of wind turbine design parameters [287]

Table 4-1: Design parameters used to determine the aerodynamic loads for NREL 5-MW wind turbine blade [219]

Term	Parameters
Power capacity	5-MW
Rotor orientation, numbers	Upwind, three blades
Rotor, hub diameter	126 m, 3 m
Hub height	90 m
TipRad	63 m
Cut-in, rated, cut-out wind speed	3 m/s, 11.4 m/s, 25 m/s
Cut-in rated rotor speed	6.9 rpm, 12.1 rpm
Overhang	5 m
Shaft tilt	5°
Precone	2.5°

The aerodynamic loading derived from AeroDyn can be defined with F_n, F_t, and M_m, which indicate the force normal to the rotor plane, force tangential to the rotor plane, and pitching moment (respect to the pitching axis), respectively; the detailed illustration is in Figure 4-2 [136]. The 61.5-meter-long blade is divided into 19 control locations to output the computed aerodynamic loading, and the results of wind speed in 11.4 m/s and 25 m/s are summarized in Table 4-2 and Table 4-3.

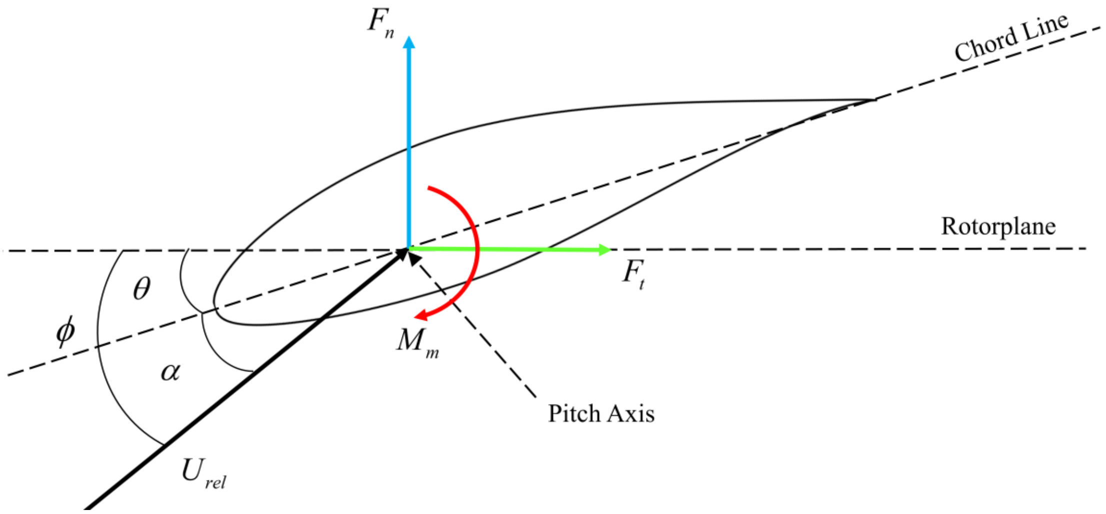

Figure 4-2: Indication of aerodynamic loads (view from the root toward the tip) [136]

Table 4-2: Aerodynamic loads of 11.4 m/s wind speed calculated by AeroDyn

Number	Span position	F_n (N/m)	F_t (N/m)	M_m (N*m/m)
1	0	124	-40	0
2	1.367	164	-102	0
3	4.1	149	-138	0
4	6.833	1400	556	-399
5	10.25	2030	772	-749
6	14.35	2440	767	-1050
7	18.45	2910	767	-1470
8	22.55	3560	788	-1970
9	26.65	4140	790	-2230
10	30.75	4870	796	-2330
11	34.85	5570	794	-2470
12	38.95	5940	790	-2250
13	43.05	6510	779	-2250
14	47.15	7020	753	-2190
15	51.25	7300	697	-2090
16	54.67	7080	593	-1860
17	57.4	5100	379	-930
18	60.13	2380	-29	-792
19	61.5	-4	0	

Table 4-3: Aerodynamic loads of 25 m/s wind speed calculated by AeroDyn

Number	Span position	F_n (N/m)	F_t (N/m)	M_m (N*m/m)
1	0	576	-84	0
2	1.367	703	-200	0
3	4.1	578	-244	0
4	6.833	4375	1526	-2269
5	10.25	4575	1362	-2703
6	14.35	5273	1452	-2793
7	18.45	5218	1431	-2993
8	22.55	5528	1582	-2870
9	26.65	6600	1917	-2749
10	30.75	7442	2256	-2243
11	34.85	8156	2269	-2090
12	38.95	9866	2383	-2269
13	43.05	10492	2343	-2205
14	47.15	11008	2272	-2149
15	51.25	11365	2196	-2048
16	54.67	11167	2042	-1807
17	57.4	8224	1446	-901
18	60.13	2377	-29	-792
19	61.5	-4	0	

The aerodynamic loading calculated by AeroDyn is distributed load per unit length; however, while defining load cases in ABAQUS, it needs to be converted to nodal loads based on the mechanic concept about the transition between distributed and concentrated loads. As shown in Figure 4-3, the reference point is coupled by several points located at the edge of a specific cross-section, then the loads can be assigned at this point in three directions. The converted nodal loads associated with two different wind speeds are summarized in Table 4-4 and Table 4-5, respectively.

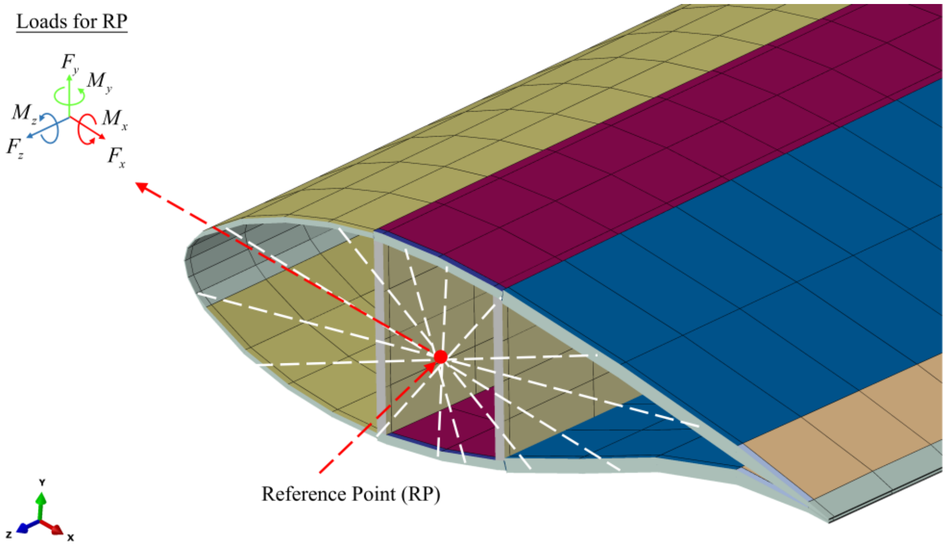

Figure 4-3: Aerodynamic loads defined at reference points in ABAQUS

Table 4-4: Converted aerodynamic loading associated with 11.4 m/s wind speed

No.	Span position	F_x (N)	F_y (N)	M_x (N*m)	M_y (N*m)	M_z (N*m)
1	0	0.00	0.00	0.00	0.00	0.00
2	1.367	-29.82	85.08	-38.85	14.84	0.00
3	4.1	-193.55	393.61	-512.46	225.34	0.00
4	6.833	-328.63	428.37	-593.72	425.97	0.00
5	10.25	702.99	2613.20	-3218.56	-527.26	-680.10
6	14.35	2750.74	7072.61	-13591.38	-5316.40	-2350.47
7	18.45	3223.03	9270.39	-18409.65	-6607.03	-3681.12
8	22.55	3228.83	11139.24	-22152.79	-6615.32	-5187.68
9	26.65	3278.13	13485.27	-26724.02	-6690.23	-7055.69
10	30.75	3334.54	16052.27	-32073.47	-6827.17	-8585.45
11	34.85	3366.41	18793.36	-37486.61	-6887.99	-9328.65
12	38.95	3390.63	21796.72	-43670.35	-6947.39	-9839.29
13	43.05	3395.45	24077.72	-48813.26	-6960.77	-9715.05
14	47.15	3375.76	26068.53	-52625.90	-6933.67	-9279.37
15	51.25	3302.35	28332.79	-57349.27	-6806.64	-9153.44
16	54.67	2678.50	25617.61	-44529.98	-4742.57	-7530.96
17	57.4	1865.48	19949.42	-27026.46	-2575.93	-5375.33
18	60.13	1438.59	17021.57	-24202.18	-2076.71	-3813.42
19	61.5	275.25	5376.45	-4239.74	-266.33	-1215.52

Table 4-5: Converted aerodynamic loading associated with 25 m/s wind speed

No.	Span position	F_x (N)	F_y (N)	M_x (N*m)	M_y (N*m)	M_z (N*m)
1	0	0.00	0.00	0	0	0.00
2	1.367	-29.82	85.08	-180.7	28.7352	0.00
3	4.1	-193.55	393.61	-2309.8	456.995	0.00
4	6.833	-328.63	428.37	-2469.5	800.566	0.00
5	10.25	702.99	2613.20	-10498	-1967.5	-680.10
6	14.35	2750.74	7072.61	-37423	-12395	-2350.47
7	18.45	3223.03	9270.39	-40496	-11739	-3681.12
8	22.55	3228.83	11139.24	-44255	-12168	-5187.68
9	26.65	3278.13	13485.27	-44747	-12401	-7055.69
10	30.75	3334.54	16052.27	-49449	-14168	-8585.45
11	34.85	3366.41	18793.36	-57747	-16966	-9328.65
12	38.95	3390.63	21796.72	-64504	-18941	-9839.29
13	43.05	3395.45	24077.72	-73500	-19456	-9715.05
14	47.15	3375.76	26068.53	-84768	-19970	-9279.37
15	51.25	3302.35	28332.79	-89769	-19562	-9153.44
16	54.67	2678.50	25617.61	-68279	-13805	-7530.96
17	57.4	1865.48	19949.42	-41333	-7855.9	-5375.33
18	60.13	1438.59	17021.57	-37322	-6769.4	-3813.42
19	61.5	275.25	5376.45	-6172.6	-942.25	-1215.52

4.1.2 Debonding hotspot simulation under aerodynamic loading

4.1.2.1 Deformation and stress modeling results

The tip deflection and Stress Von Mises distributions along the blade span are sketched in Figure 4-4. For wind speeds of 11.4 m/s and 25 m/s conditions, the tip displacements are 4.23 m and 6.29 m, respectively, which are similar to the tip movement from another blade investigation under aerodynamic loads [258]. For both wind speed cases, it can be noticed that the most critical region of the stress schedule is located at the trailing edge near the root area (a distance of 9.05 m from the root). Chen [17] did a practical full-scale on a 52.3-meter blade with flap-wise bending, where the results indicated the stress concentrated in similar locations as the current project. Also, Zuo [258] applied aerodynamic loads on a 1.5-MW blade and concluded that the maximum stress appeared at 6.1 m out of a 70 m blade span. However, the maximum stress point is near the spar cap instead of the trailing edge. This scenario might be caused by the geometrical imperfection or different modeling strategies, which could lead to stress concentration. Therefore, it cannot conclude that the maximum point at the trailing edge of this project is the most critical case due to the deficiency of testing data support. Nevertheless, it can still give reference for further investigation, and on the other hand, the regions near the root area are susceptible to stress concentration and debonding initiation.

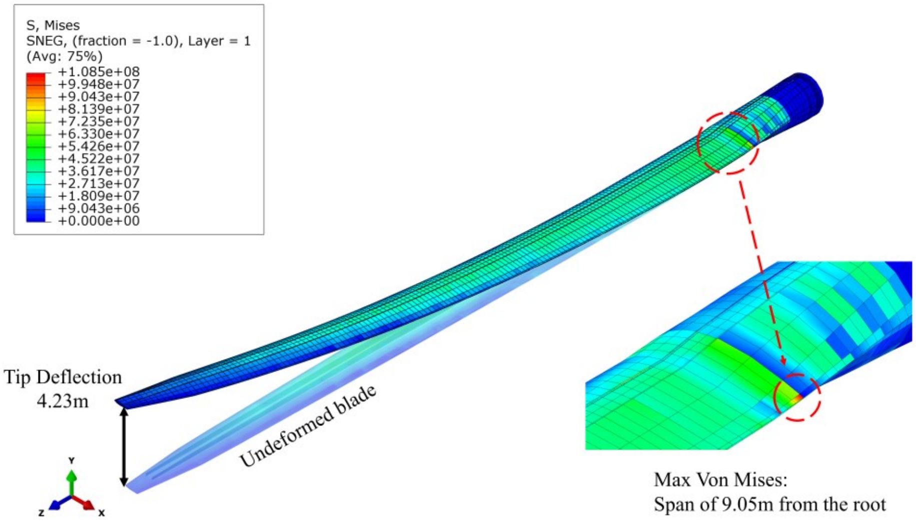

(a) Deformation and Stress Von Mises cloud diagram of 11.4 m/s wind speed

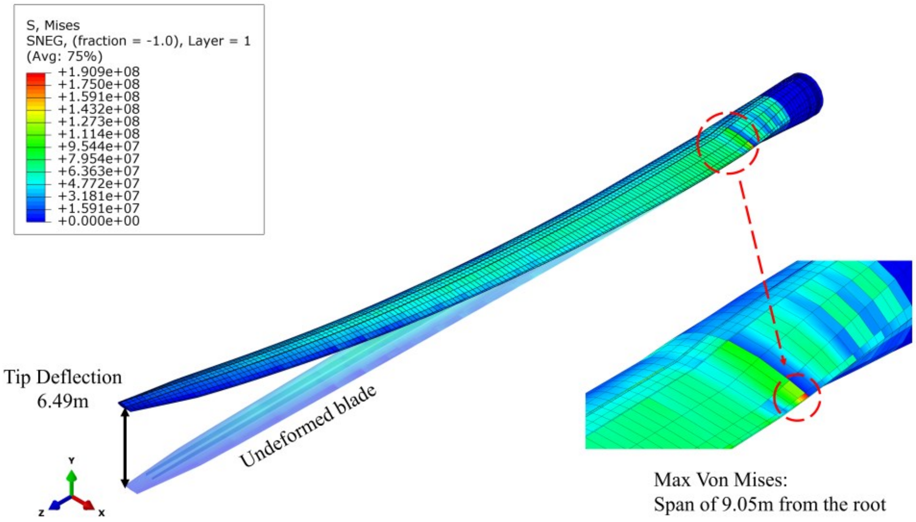

(b) Deformation and Stress Von Mises cloud diagram of 25 m/s wind speed

Figure 4-4: Deformation and Stress Von Mises cloud diagram of the 5-MW blade

4.1.2.2 *Results of cap-web debonding hotspot*

The 5-MW blade is analyzed under the aerodynamic load determined by AeroDyn, which is applied statically. CSMAXSCRT [288], expressed by (Eq. 2-26), is used as a debonding damage indicator to evaluate the extent of cohesive damage: if a contact site has reached the maximum traction stress, and the debonding will be triggered based on the maximum nominal stress criterion. For four cohesive target connections, LE-TOP, TE-TOP, LE-BOT, and TE-BOT, mentioned in Figure 3-4, the simulation results are summarized in Figure 4-5, Figure 4-6, and Table 4-6.

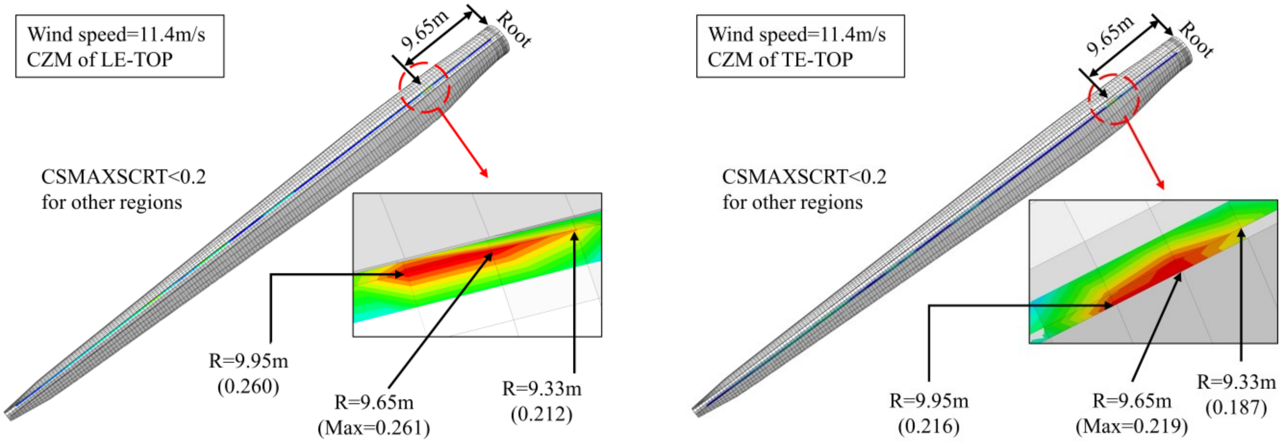

(a) LE-TOP

(b) TE-TOP

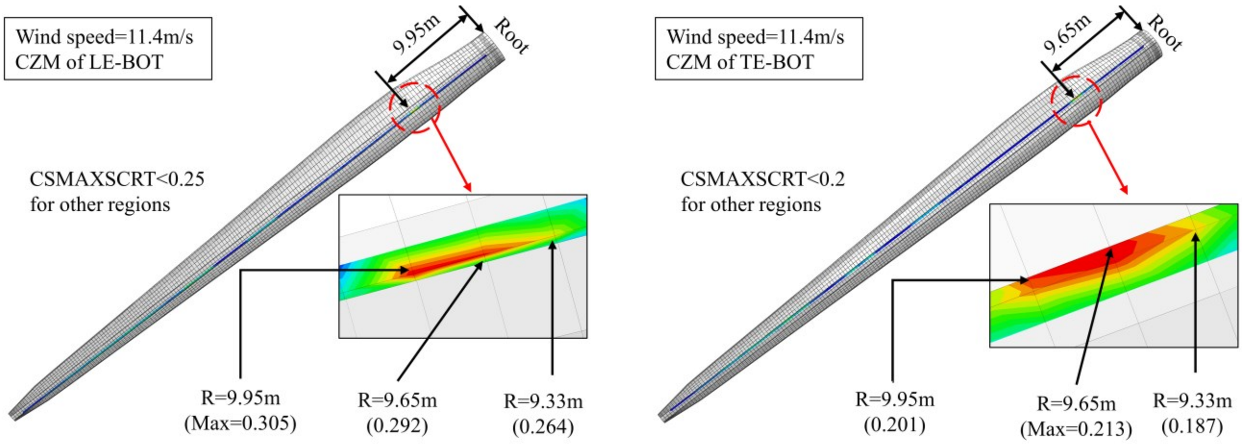

(c) LE-BOT

(d) TE-BOT

Figure 4-5: Debonding hotspot for four damaged parts with 11.4 m/s wind speed based on CSMAXSCRT

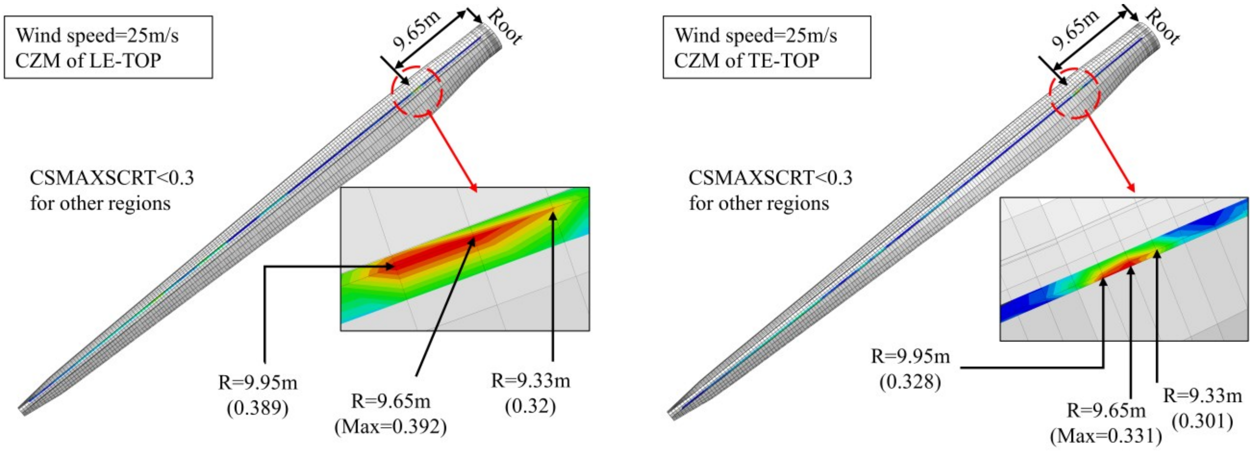

(a) LE-TOP (b) TE-TOP

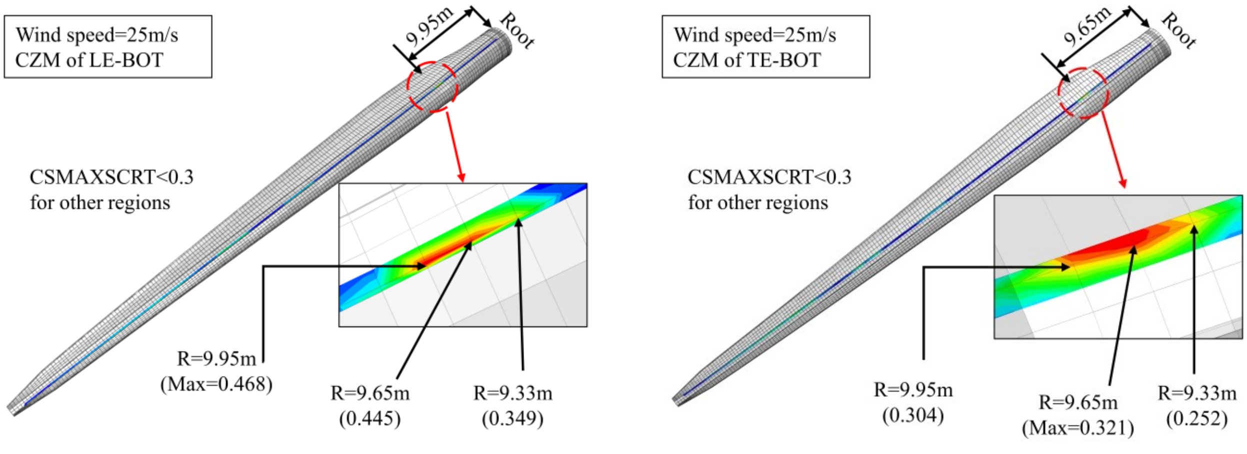

(c) LE-BOT (d) TE-BOT

Figure 4-6: Debonding hotspot for four damaged parts with 25 m/s wind speed based on CSMAXSCRT

The CSMAXSCRT values are shown in contour plots in Figure 4-5 and Figure 4-6 for the WTB under two different aerodynamic loads associated with different wind speeds, which shows the damage extent at the four adhesive connections between the spar cap and the shear webs. It is found that the most critical debonding regions are the same under different aerodynamic loads associated with different wind speeds. The most critical debonding regions (e.g., CSMAXSCRT > 0.25 ~ 0.3) are primarily located at intervals of 9.33 to 9.95 meters away from the root in a spanwise direction for both rated and cut-out wind speed levels. The overall simulation results of the four adhesive joints between the spar cap and shear webs (LE-TOP, TE-TOP, LE-BOT, TE-BOT) are summarized in Table 4-6, with the maximum CSMAXSCRT values and spanwise locations. According to Table 4-6, except LE-BOT (9.95 m), the other three have the same maximum CSMAXSCRT at the same position of 9.65 m. Furthermore, LE-BOT is the most likely to have cohesive damage or debonding compared to the other three. This observation is similar to the finding in another research [258], which simulated various wind speeds on a 33.25-meter-long blade to investigate the debonding behavior based on the crack density distribution. The author observed that the debonding between the spar cap and shear web was the first crack initiated at around 6.1 m spanwise position with rated wind speed and propagated from 2 m to 15 m at the cut-out speed. Furthermore, the vulnerable region (9.33 m-9.95 m in spanwise position) is located at the most critical region, as proved by another full-scale test on a 34-meter blade [18]. The author discovered that the internal blade structure formed by the spar cap and shear webs could be regarded as a long, thin hollow beam. Thus, the hotspot identified is credible to some extent and is instructive for future experiments or damage investigations. In this case, 9 m-10.25 m, which is located between the 14th and 15th stations, is considered in the following simulations as the hotspot.

Table 4-6: Max CSMAXSCRT values and positions in the WTB under different aerodynamic loads associated with different wind speeds

	11.4 m/s (rated wind speed)		25 m/s (cut-out wind speed)	
	Max CSMAXSCRT value	Max CSMAXSCRT position (m)	Max CSMAXSCRT value	Max CSMAXSCRT position (m)
LE-TOP	0.261	9.65	0.392	9.65
TE-TOP	0.219	9.65	0.331	9.65
LE-BOT	0.305	9.95	0.468	9.95
TE-BOT	0.213	9.65	0.321	9.65

4.2 Debonding area growth with initial crack in the hotspot

The above debonding modeling aims to inspect the critical regions vulnerable to cap-web debonding failure. Results of different aerodynamic load levels consistently indicated that 9 m to

10.25 m cap-web connections is more vulnerable to debonding than other areas. On the other hand, the damage indicators in Table 4-6 are all smaller than one, indicating no separation initiated despite under 25 m/s wind speed. This scenario is probably due to the solid cohesive material utilization, non-fatigue aerodynamic loads, and neglect of geometrical imperfection in wind turbine blades. Since normal wind loads (i.e., without considering the fatigue effect) cannot initiate the debonding, to further confirm the most vulnerable area or hotspot identified above for debonding, potential crack growth is examined when an initial crack (or complete debonding) exists at the boundary of the hotspot areas identified. To demonstrate the potential debonding area growth, initial cracks are assumed at the two ends of the hotspot area identified. As shown in Figure 4-7 (a), the hotspot area (i.e., between 9 m and 10.25 m) is evenly divided into five zones with 250 mm each, denoted as zone #1, #2, #3, #4, and #5 in the spanwise direction from the WTB root to the tip. A pre-existing crack is assumed at #1 and #5, referred to as crack #1 and #5, respectively (see Figure 4-7 (b)), to investigate whether the crack growth tendency is towards the hotspot or not. Note that the element size for each zone is refined to ensure three elements in each zone to simulate the debonding propagation in these areas better.

The rated aerodynamic loading pattern with increasing amplitude (e.g., to 20 times) is applied to the WTB to demonstrate debonding propagation. Crack #1 or crack #5 are defined for LE-BOT, LE-TOP, TE-BOT, and TE-TOP, respectively, which means only one pre-existing crack for each study case. This leads to a total of 8 case studies for the debonding crack growth analysis in the hotspot areas.

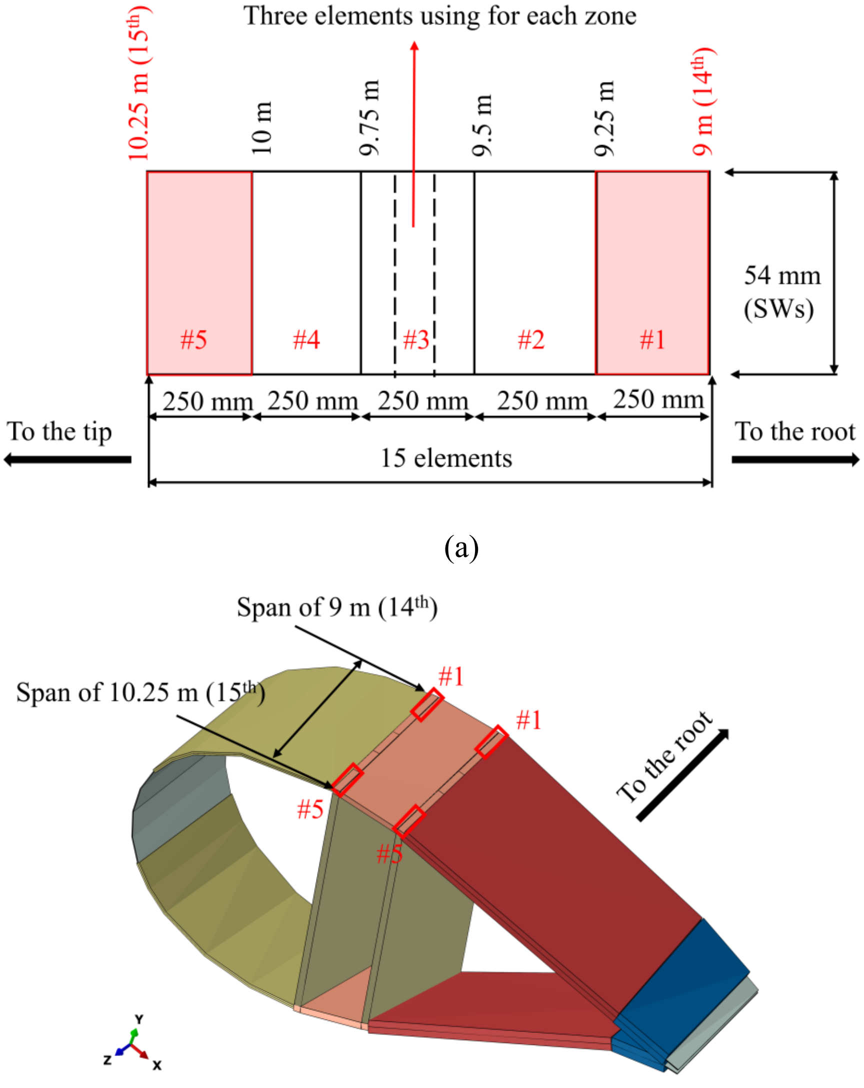

(a)

(b)

Figure 4-7: Pre-definition of cracks in the 5-MW blade

4.2.1 Debonding propagation results

As for the debonding hotspot inspection, the cohesive connections are defined at LE-BOT, LE-TOP, TE-BOT, and TE-TOP, and then the analysis is performed. However, in the simulation of debonding propagation, one initial crack is assumed in one of the four cohesive connections, respectively, which means the other three cohesive connections keep intact.

4.2.1.1 Debonding propagation with crack #1 (9-9.25 m) pre-defined

LE-BOT with crack #1

With the initial crack existing at 9-9.25 m, the pre-existing crack located at LE-BOT does not grow towards the root beyond 9 m (Figure 4-8 (a)). In contrast, the debonding propagates to the tip side to a relatively large degree, developing from 9.25 m to 10.78 m in the final stage (Figure 4-8-(b)). The configuration of debonding is peeling-dominated, also combined with small out-of-plane shear due to the slight buckling influence of the shear web.

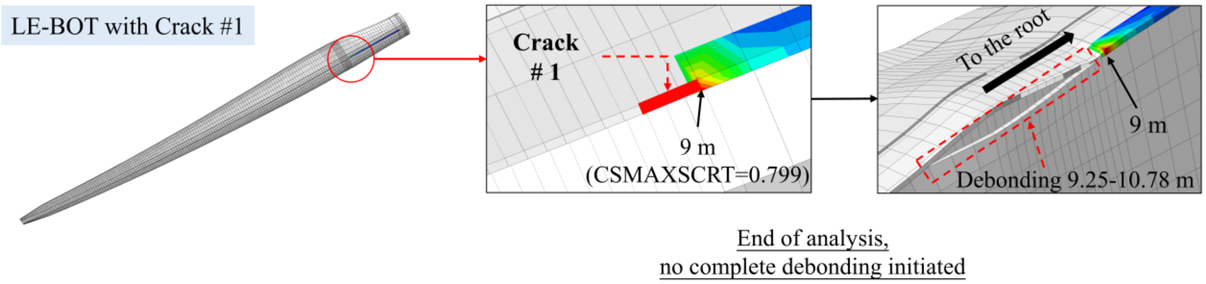

(a) On the root side of the pre-existing crack #1

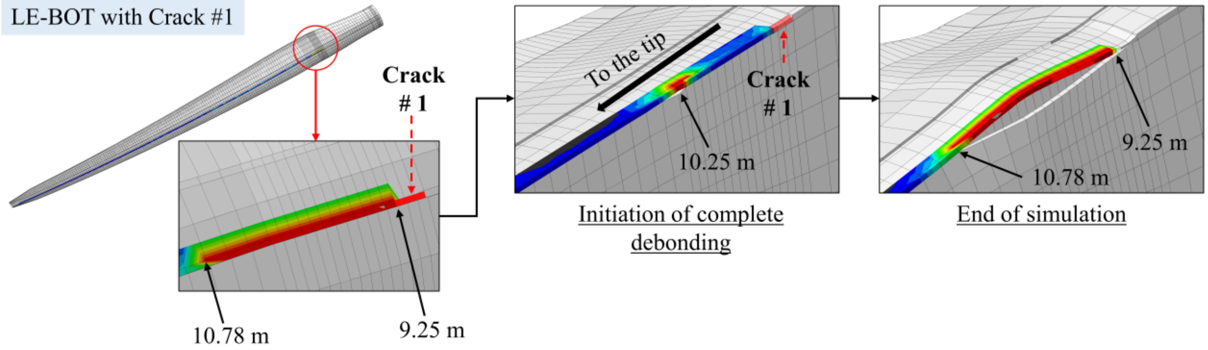

(b) On the tip side of the pre-existing crack #1, including hotspot (9 m – 10.25 m)

Figure 4-8: Debonding propagation of WTB with a pre-existing crack #1 for LE-BOT

LE-TOP with crack #1

The debonding growth fro crack #1 located at LE-TOP is not dramatic; after experiencing the extreme aerodynamic loading (i.e., 20 times), the root-oriented separation is only limited at slight peeling around 9 m and does not propagate further (Figure 4-9 (a)). Nevertheless, the peeling-like debonding growth is relatively small, from 9.25 m to 9.33 m (Figure 4-9 (b)).

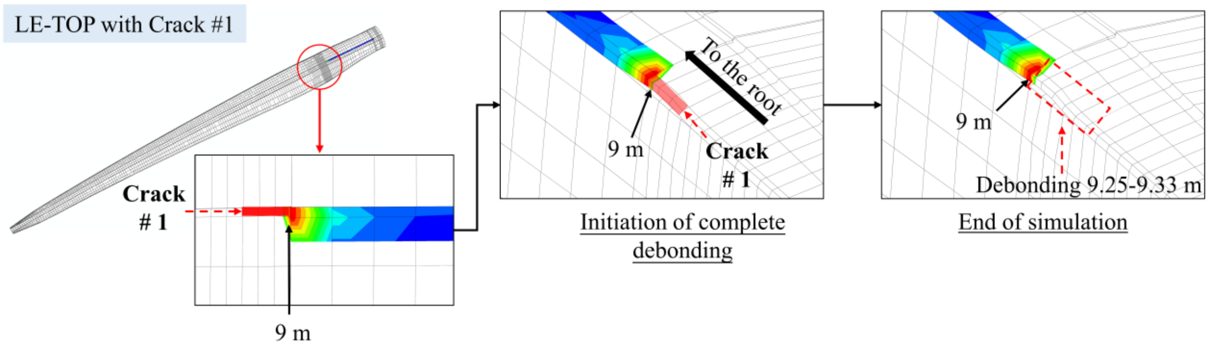

(a) On the root side of the pre-existing crack #1

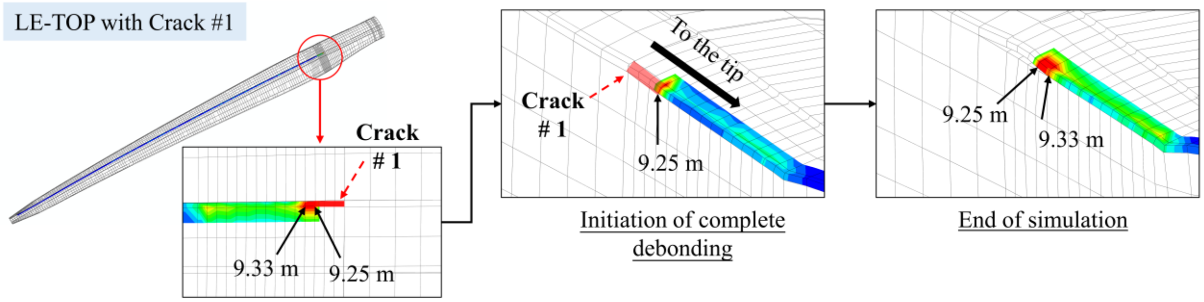

(b) On the tip side of the pre-existing crack #1, including hotspot (9 m – 10.25 m)

Figure 4-9: Debonding propagation of WTB with a pre-existing crack #1 for LE-TOP

TE-BOT with crack #1

The debonding crack growth behavior of WTB with an initial crack located at TE-BOT is quite similar to the case of LE-BOT with pre-existing crack #1. The crack is hard to grow towards the root beyond 9 m (Figure 4-10 (a)), while on the tip-oriented side, the debonding-induced separation (cracking) becomes more dramatic, with an almost one-meter crack length (9.25-10.25 m) (Figure 4-10 (b)). Compared with the LE-BOT case, the debonding is initiated at the same position (10.25 m).

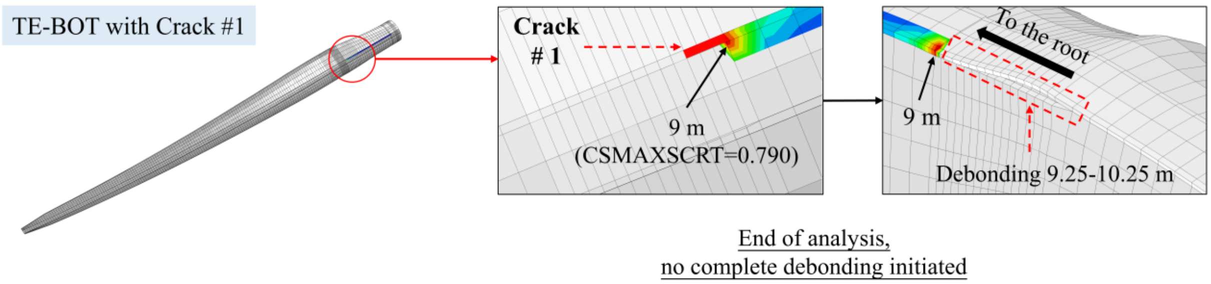

(a) On the root side of the pre-existing crack #1

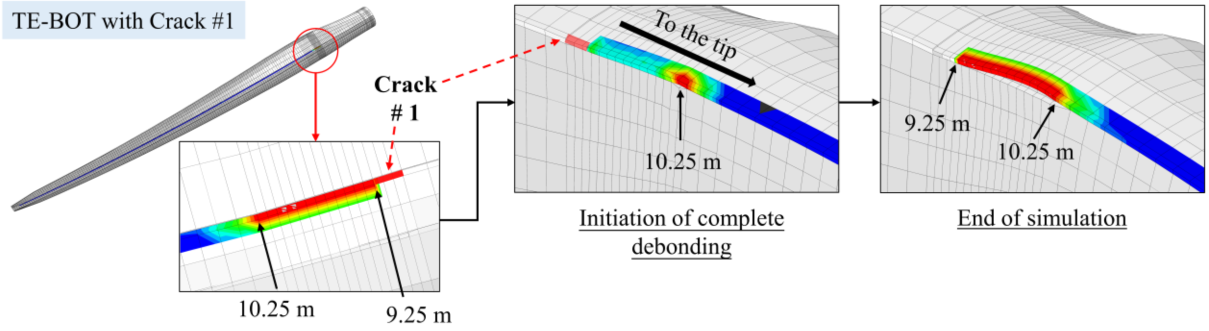

(b) On the tip side of the pre-existing crack #1, including hotspot (9 m – 10.25 m)

Figure 4-10: Debonding propagation of WTB with a pre-existing crack #1 for TE-BOT

TE-TOP with crack #1

The eventual crack size of the WTB with a pre-existing crack at TE-TOP is larger than LE-TOP but smaller than the other two cases (TE-BOT, LE-BOT). For the root-oriented side beyond 9 m, the detachment/separation can not be triggered (Figure 4-11 (a)). The debonding grows from 9.25 m and finally extends to 9.75 m (Figure 4-11 (b)).

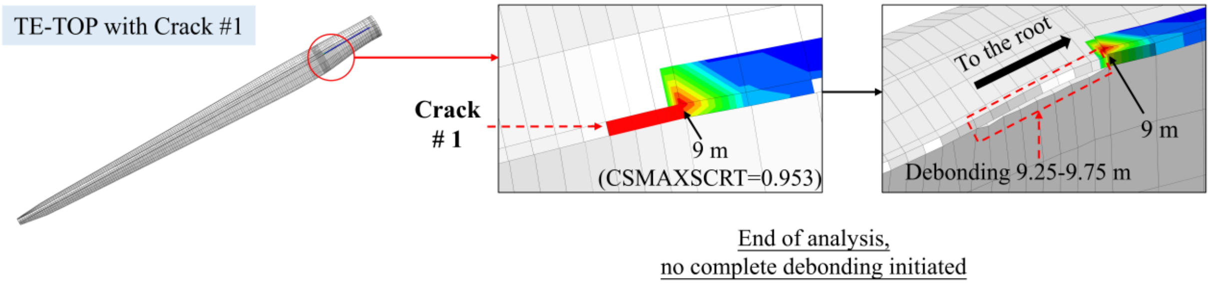

(a) On the root side of the pre-existing crack #1

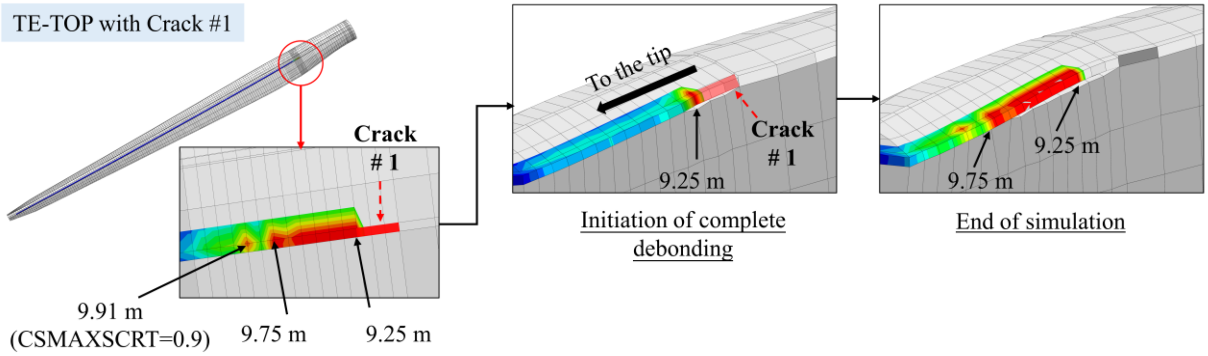

(b) On the tip side of the pre-existing crack #1, including hotspot (9 m – 10.25 m)

Figure 4-11: Debonding propagation of WTB with a pre-existing crack #1 for TE-TOP

4.2.1.2 Debonding propagation with crack #5 (10-10.25 m) pre-defined

LE-BOT with crack #5

Compared with crack #1, crack #5 gives rise to more dramatic debonding propagation. The crack propagates from 10 m to 9.08 m on the root-oriented side and extents until 10.78 m on the tip-oriented side (Figure 4-12 (a)). Hence, the total crack is from 9.08 to 10.78 m in a spanwise direction. According to Figure 4-12, the damaged configuration is likely the debonding in a normal direction combined with slight in-plane shear damage.

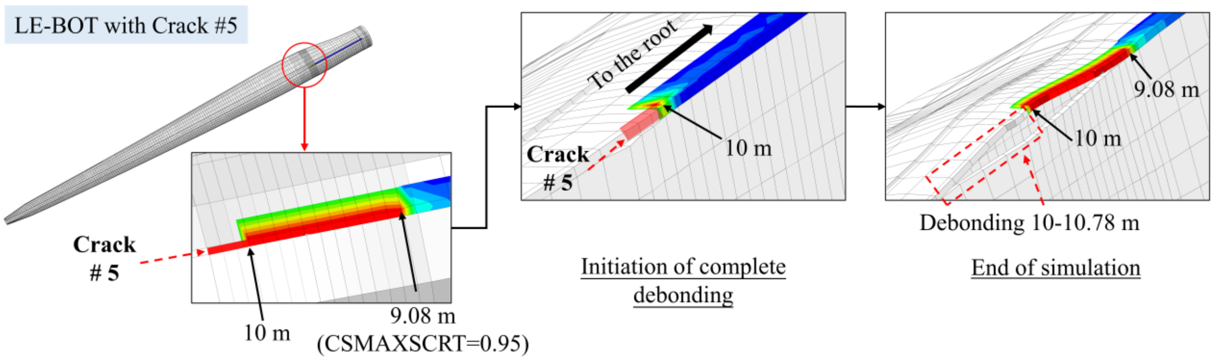

(a) On the root side of the pre-existing crack #5, including hotspot (9 m – 10.25 m)

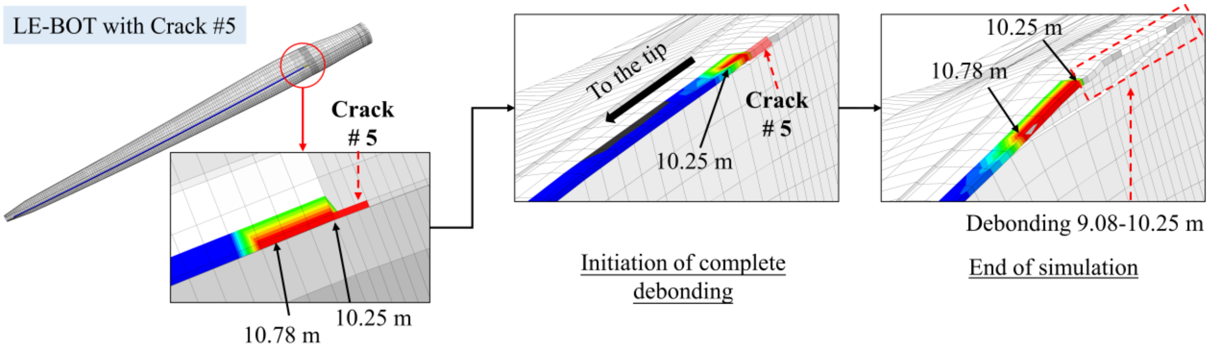

(b) On the tip side of the pre-existing crack #5

Figure 4-12: Debonding propagation of WTB with a pre-existing crack #5 for LE-BOT

LE-TOP with crack #5

Among the results of four cases with crack #1, the LE-TOP case shows the least debonding growth. With pre-existing crack #5 in the hotspot area, local buckling of the web near the 10.25 m span (Figure 4-13) occurs. Thus the debonding behavior is not well captured due to the non-convergence or numerical instability caused by local buckling.

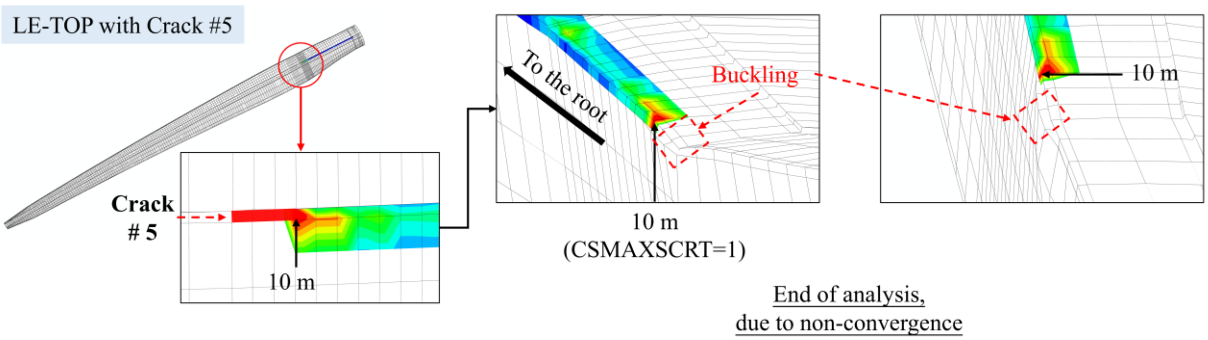

(a) On the root side of the pre-existing crack #5, including hotspot (9 m – 10.25 m)

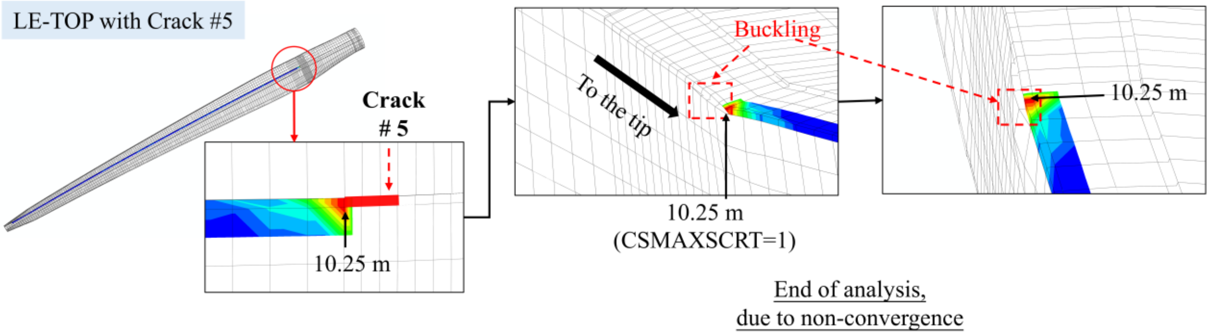

(b) On the tip side of the pre-existing crack #5

Figure 4-13: Debonding propagation of WTB with a pre-existing crack #5 for LE-TOP

TE-BOT with crack #5

In this case, the pre-existing crack #5 leads the crack propagation to the root-oriented side until 9.08 m (Figure 4-14 (a)). No further debonding is observed beyond 10.25 m toward the tip (Figure 4-14 (b)).

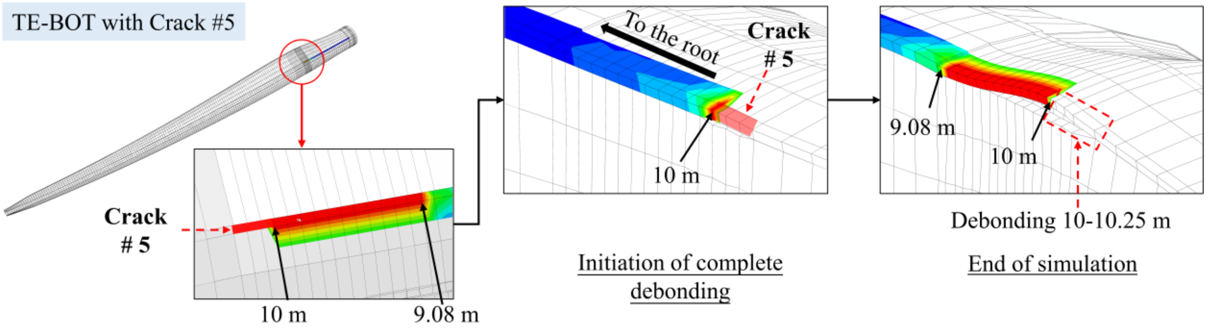

(a) On the root side of the pre-existing crack #5, including hotspot (9 m – 10.25 m)

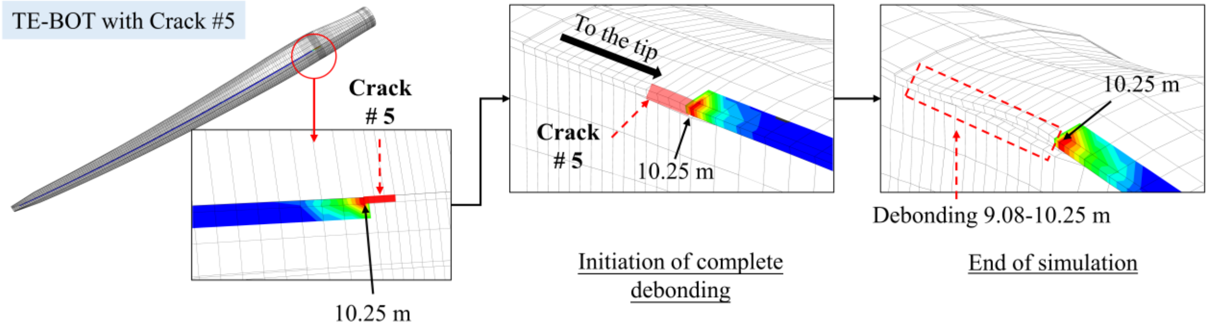

(b) On the tip side of the pre-existing crack #5

Figure 4-14: Debonding propagation of WTB with a pre-existing crack #5 for TE-BOT

TE-TOP with crack #5

With pre-defined crack #5, the detachment at TE-TOP is initially triggered at the spanwise positions of 9.08 m, 9.25 m, and 9.5 m simultaneously (Figure 4-15 (a)), and no propagation beyond the hotspot area identified under the aerodynamic load considered

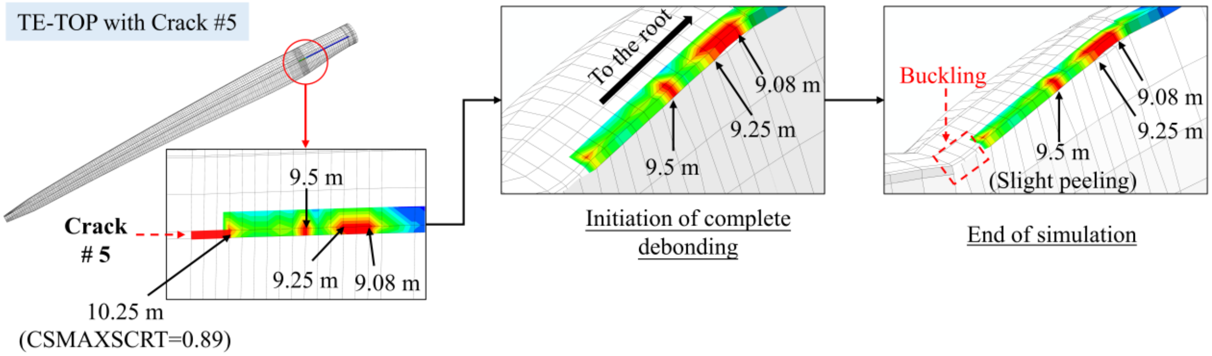

(a) On the root side of the pre-existing crack #5, including hotspot (9 m – 10.25 m)

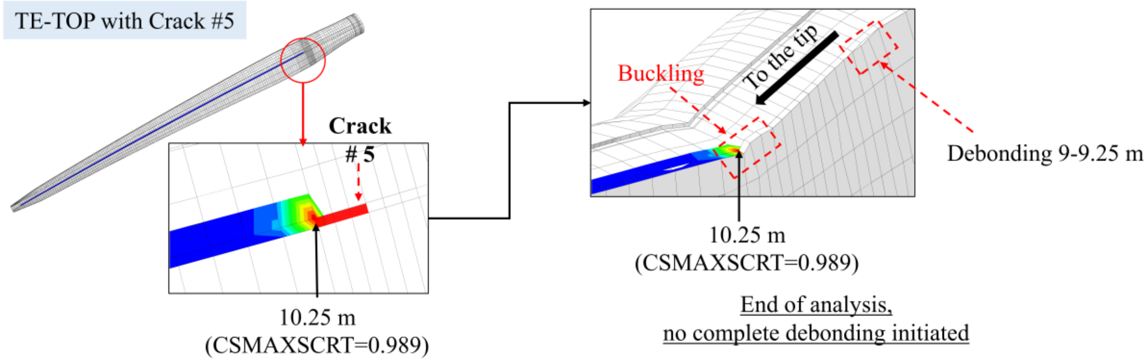

(b) On the tip side of the pre-existing crack #5

Figure 4-15: Debonding propagation of WTB with a pre-existing crack #5 for TE-TOP

4.3 Discussion

Among these 8 study cases, the cases with pre-existing cracks for LE-BOT are considered most susceptible to debonding growth. Figure 4-8 and Figure 4-12 present the debonding propagation for the WTB with pre-existing crack #1 and crack #5 at LE-BOT, respectively. The pre-existing crack #1 grew to form a longer crack (9 m-10.78 m) due to complete debonding. This means that debonding is prone to propagate mainly toward the hotspot area. Similarly, the pre-existing crack #5 grew to a longer crack (9.08 m-10.78 m). Note that under the extreme loading considered in the simulation, only the two cases related to LE-BOT revealed that the pre-existing crack extended beyond the hotspot 9 m-10.25 m; while the other 6 cases (related to LE-TOP, TE-BOT, TE-TOP) all revealed that the pre-existing crack grew within the hotspot area (9 m-10.25 m).

Table 4-7 summarizes the debonding propagation results for all 8 study cases considered. Following LE-BOT, which is the most susceptible to debonding, the second to the most vulnerable part is found to be TE-BOT. In contrast, the crack growth at LE-TOP and TE-TOP is limited on a relatively small scale under the same level of aerodynamic loading. Hence, cohesive damage is more likely to occur at the bottom side of the turbine blade. Under aerodynamic load, the blade is mainly bent in a flapwise direction, leading to compression for the top blade surface and tension for the bottom blade surface. As such, due to debonding, the local buckling of the web is observed for the cases with pre-existing crack #5 for LE-TOP and TE-TOP. Compared with the cases with pre-existing crack #1 for LE-TOP and TE-TOP, no buckling is observed, indicating that crack #5 is more critical than crack #1.

Table 4-7: Summary of debonding propagation with pre-existing crack #1 or crack #5

Term	Crack #1 (9-9.25 m)		Crack #5 (10-10.25 m)	
	Root side (0-9 m)	Tip side (9.25-61.5 m)	Root side (0-10 m)	Tip side (10.25-61.5 m)
LE-BOT	No debonding	9.25-10.78 m	9.08-10 m	10.25-10.78 m
LE-TOP	Around at edge of 9 m	9.25-9.33 m	Local buckling occurred	Local buckling occurred
TE-BOT	No debonding	9.25-10.25 m	9.08-10 m	Around at edge of 10.25 m
TE-TOP	No debonding	9.25-9.75 m	9.08-9.25 m & Around at edge of 9.5 m	No debonding

CHAPTER 5: DYNAMIC ANALYSIS OF WTBS WITH AND WITHOUT DEBONDING

After confirming the most vulnerable debonding areas in the WTB considered, this section aims to simulate the dynamic behavior of the WTB with different debonding conditions in the hotspot, compared to the counterpart of WTB without debonding damage. The ultimate goal is to consolidate instructional information to enhance the effectiveness of practical debonding inspection and inference. To be specific, two types of vibration tests (e.g., free vibration test, impact load test) are simulated, and complete debonding scenarios with different debonding crack lengths, i.e., 1.25 m (9 m to 10.25 m) and 5.35 m (9 m to 14.35 m), located in LE-BOT, LE-TOP, TE-BOT, and TE-TOP, are considered.

5.1 Dynamic properties of the 5-MW blade

In the previous 5-MW blade modeling work performed by NREL [84], [219], a structural damping ratio of 1.5% was applied to all modes in FAST [289] for aerodynamic simulation. However, the damping ratio input is different in ABAQUS compared to FAST. In ABAQUS, the general damping techniques include Rayleigh damping, composite modal damping, and structural damping, and the damping ratio for each mode also can be specified during modal analysis. However, the ABAQUS structural damping ratio only works for sinusoidal stimulation [215]. Thus, the damping should be converted to Rayleigh damping, with reference to the following equations (Eq. 5-1) and (Eq. 5-2):

$$\xi_1 = \frac{1}{2}\left(\alpha\omega_1 + \frac{\beta}{\omega_1}\right) \qquad \text{(Eq. 5-1)}$$

$$\xi_2 = \frac{1}{2}\left(\alpha\omega_2 + \frac{\beta}{\omega_2}\right) \qquad \text{(Eq. 5-2)}$$

where:

ξ_i : Conversed structural damping in ABAQUS

α, β : Rayleigh damping factors

ω_i: Natural frequencies of selected modes

Accordingly, only two modes are needed to determine the damping ratio, and thus required structural damping ratio of 1.5% will be exact for only two chosen modes; the remaining modes will have damping ratios different from the targeted damping. A similar issue occurs in several study fields. Song [290] revealed that the first two vibration modes were often chosen when converting to Rayleigh damping since they might reflect the most important structural features. When Asareh [291] examined the seismic response of wind turbine systems using OpenSees [292] instead of FAST, he also encountered the same issue and chose the first two modes for further dynamic simulation. In this study, different combinations of two modes are considered to determine the best two modes for Raylay damping definition. According to Figure 5-1, the mode 1&7 combination gave the closest damping ratio of 1.5% across different modes. Note that the seventh mode shape, shown in Figure 5-2, included a combination of flapwise translation, edgewise translation, and slight torsional motion. Thus, a structural damping ratio of 1.5% is applied via the Rayleigh damping model based on mode #1 and mode #7 to ensure a close representation of the target damping characteristics of the 5-MW blade, and the following Rayleigh damping factors were derived:

$$\alpha=0.148728$$
$$\beta=0.000496$$

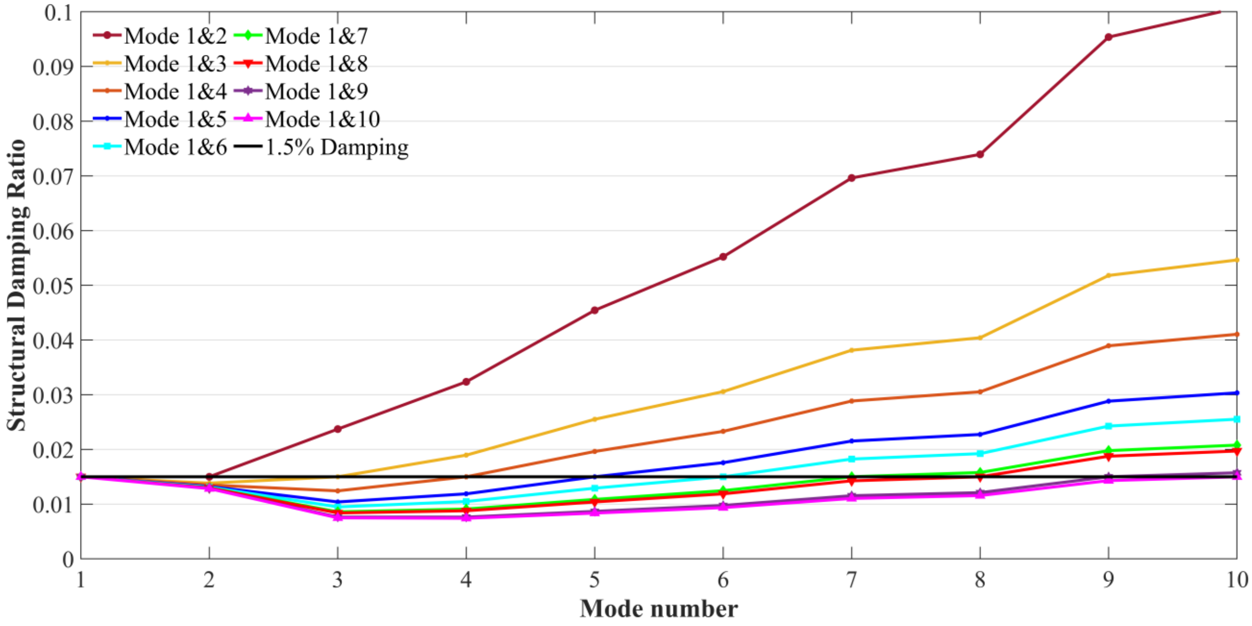

Figure 5-1: Comparison of damping ratios for the first 10 modes when using different pivoting frequencies

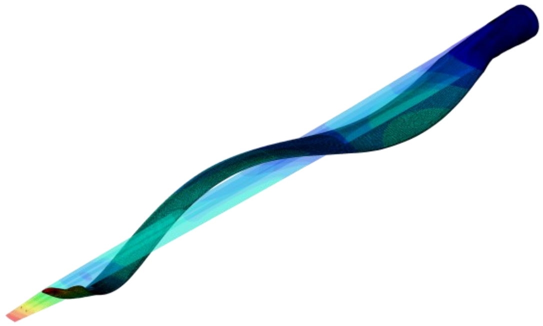

Figure 5-2: The 7th mode shape of the 5-MW blade

5.2 Free vibration analysis (FVA)

5.2.1 Initial conditions and data-collected points

The blade is mounted on the turbine rotor, which can be considered a cantilever. And free vibration analysis is a common damage detection methodology, especially for cantilever cases. This well-developed technique has been verified with satisfactory applicability [293]–[295]. Most researchers have succeeded in monitoring the damage by comparing the natural frequencies and mode shapes. Thus, free vibration analysis is introduced to extract the vibrated responses under two different cap-web debonding sizes, 9-10.25 m, and 9-14.35 m, respectively. Then summarize the characteristics among different responses and help to improve the debonding-detected efficiency.

As sketched in Figure 5-3, an initial displacement will be applied at the blade tip and then released immediately to excite the free vibration. Initial displacements in both flapwise and edgewise directions are considered, with a magnitude of 10 centimeters (around 0.16% of the 5-MW blade span). The free vibration analysis is performed in ABAQUS with a small analysis time increment of 0.01 s.

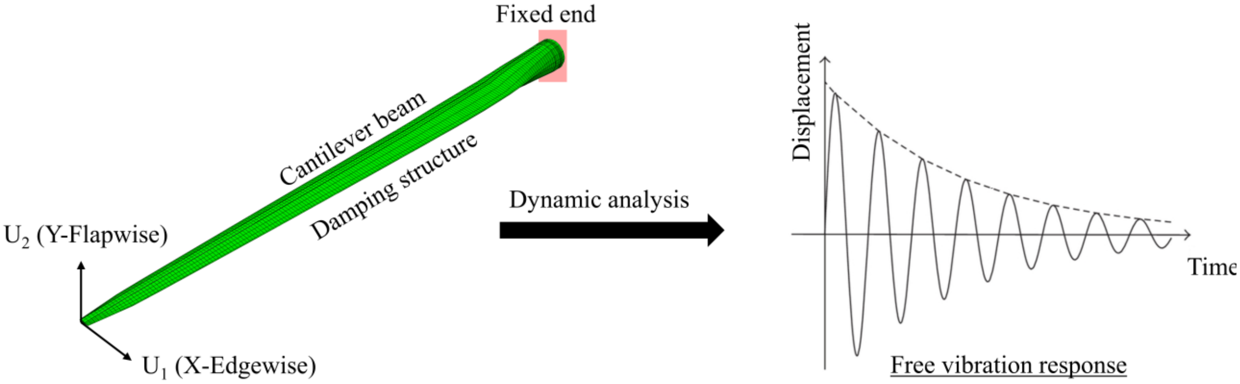

Figure 5-3: Initial displacement and free vibration response

Assume that the WTB can be instrumented differently; oscillation data in X, Y, and Z directions can be collected from sensors at different positions on the WTB. As shown in Figure 5-4, 52 (= 19+7+19+7) signal collection points are considered, which are well distributed at the top surface (TOP), bottom surface (BOT), leading edge (LE), and trailing edge (TE) of the blade. TOP and BOT points located at the margin between the spar cap and adjacent panel, LE and TE points located at the margin of each side edge. Since the most critical region (hotspot) was determined previously as located from 9 to 10.25 meters, relatively more data-collection points are considered around this region (e.g., #3, #4, #5, and #6 of TOP and BOT). Fast Fourier transform (FFT) is applied to convert the time-domain signal to the frequency-domain to better reflect the difference between the intact and damaged 5-MW blade in terms of frequency contents.

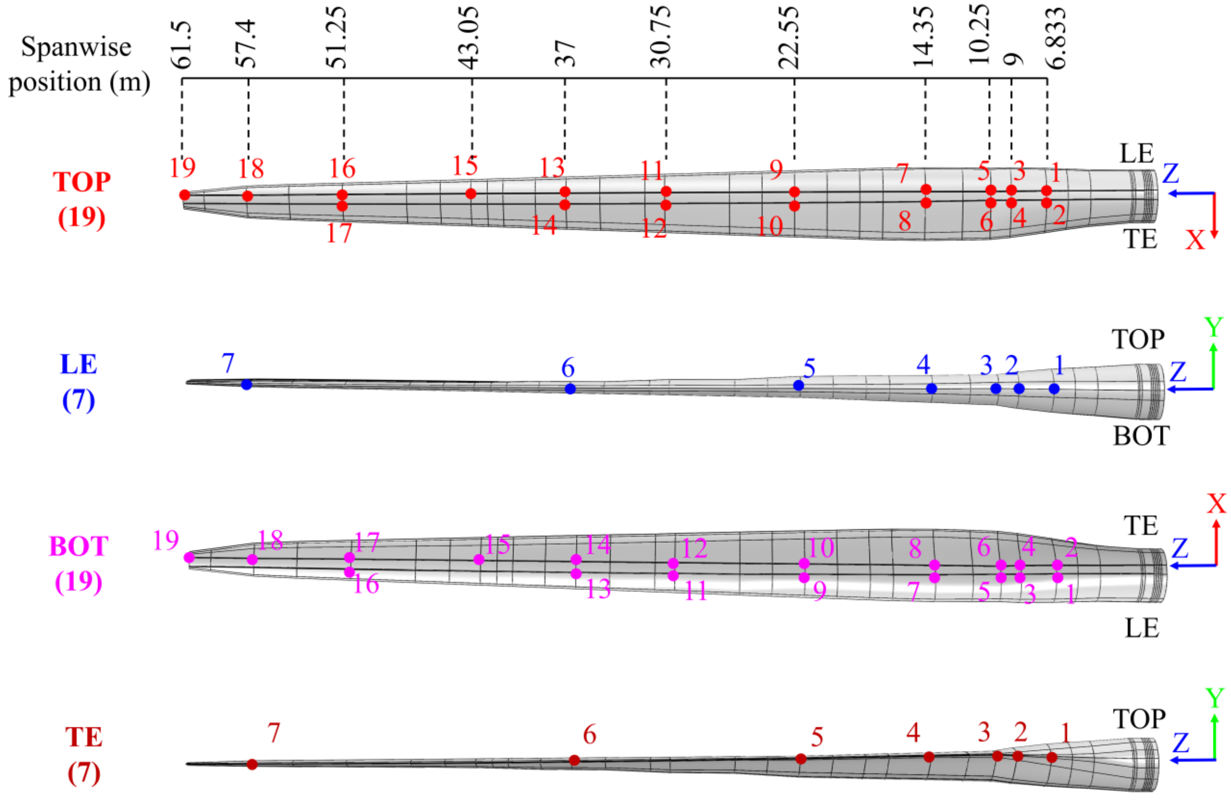

Figure 5-4: Data-collection points to simulate free vibration testing

5.2.2 Time domain results of free vibration analysis

A comprehensive comparison of the time series signals collected for the WTB with and without debonding damage shows that signal separation in the time domain is mainly reflected in the amplitude and only when the debonding crack size is large, as illustrated in Figure 5-5. The amplitude difference from the counterpart of the intact WTB is much more significant when there is a 9 m-14.35 m debonding crack located at LE-TOP. Note that no visible difference in the time series does not mean that there is no debonding damage.

In terms of excitation (i.e., applying the initial displacement) for free vibration testing, both the flapwise (Y) direction and edgewise (X) direction are effective in triggering the significantly-separated displacement signals, where the flapwise excitation performs the best. The vibration signals collected in the flapwise (Y) direction are more likely to be used to inspect debonding damage, compared to the edgewise (X) direction and the axial (Z) direction.

Regarding the signal collection locations for sensor instrumentation, the near-crack points will yield more signal separation between WTBs with and without debonding damage. Regarding the spanwise positions, the signal collection points from #1 to #8 on the BOT and TOP perform much better than distant points #9 to #19. Generally, in the free vibration test, responses collected from a 9 m-10.25 m span near the spar cap and shear web locations reveal damage better than the other locations.

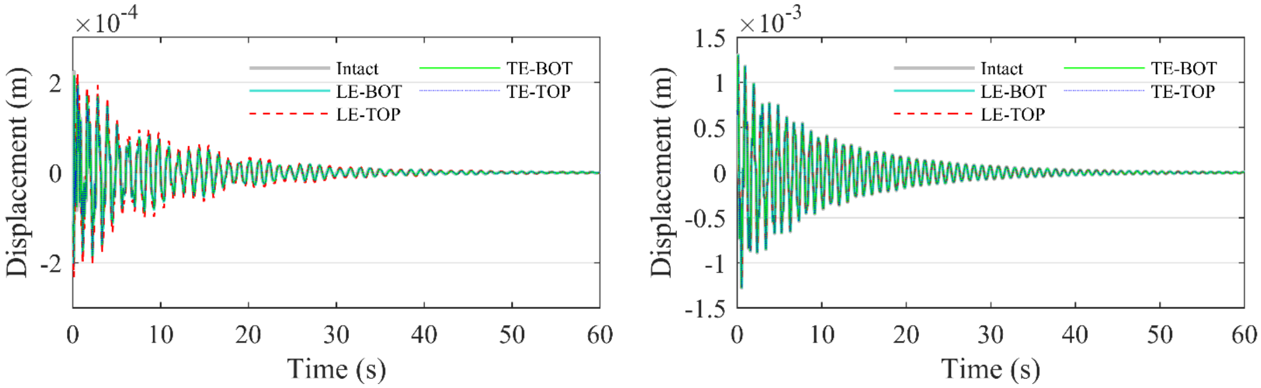

(a) Excite: flapwise (Y) & Collect: flapwise (Y)

(b) Excite: edgewise (X) & Collect: edgewise (X)

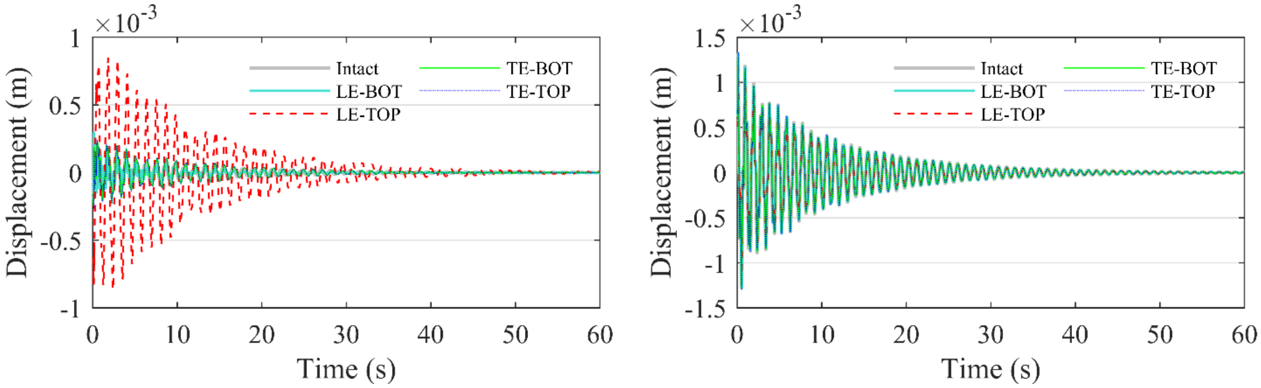

(c) Excite: flapwise (Y) & Collect flapwise (Y)

(d) Excite: edgewise (X) & Collect: edgewise (X)

Figure 5-5: Vibration signal collected at point #5 on the top surface for WTB with a debonding crack between 9 m and 10.25 m for (a) and (b), 9 m and 14.35 m for (c) and (d)

5.2.3 Frequency domain results of free vibration analysis

Fast Fourier transform (FFT) is a widely used algorithm in the engineering industry, which can convert the dynamic signal from the initial domain to the frequency domain [296]. Hence, the collected dynamic information will be significantly simplified and reflected in the selected frequency band. Generally, for many vibration analyses from predecessors' research, FFT is employed to transform the time-or-space domain results to frequency-based curves, which indicate the divergences caused by damages to a more visualized extent [297]–[300]. Based on the FFT of the signals collected, high-frequency components are pretty limited in free-vibration tests, as sketched in Figure 5-6. Free vibration testing likely triggers vibration under 5 Hz. Therefore, the zoom-in plots within the low-frequency range (0-5 Hz) are used hereafter to investigate the vibration responses for free vibration test simulations.

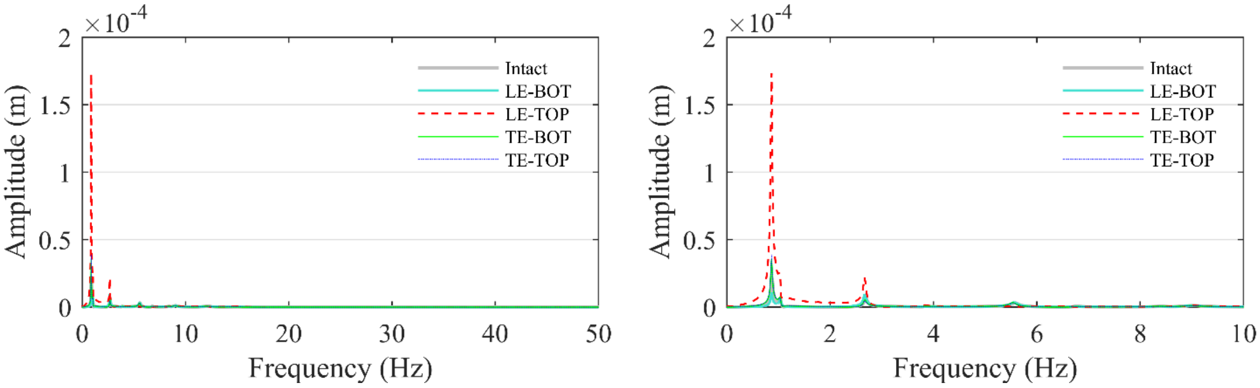

(a) 0-50 Hz (b) 0-10 Hz

Figure 5-6: Results collected from TOP-5 point within high-frequency ranges

(a) and (b) is collected in the Y-direction, with flapwise displacement under 9-14.35 m crack

Figure 5-7 and Figure 5-8 present the FFT results of representative displacements collected from free vibration simulation of the 5-MW blade with short and long pre-existing debonding cracks located in 4 different locations. According to the eigenvalue analysis results presented earlier, the first five modes with modal frequency are 1st flapwise (0.866 Hz), 1st edgewise (1.043 Hz), 2nd flapwise (2.682 Hz), 2nd edgewise (3.89 Hz), and 3rd flapwise (5.63 Hz), respectively. Note that the first two flapwise and edgewise modes are the primary modes excited in the free vibration testing, which is mainly influenced by the initial displacement direction instead of the signal-collection direction. On the other hand, the 1st flapwise or edgewise modes (0.867 Hz & 1.033 Hz) have more differences in the amplitudes at peaks due to the debonding damage than the 2nd flapwise or edgewise modes, as illustrated in Figure 5-8.

Similar to the observations made based on the time-series signal comparison, the debonding crack damage can hardly be detected based on the FFT results, because the debonding damage affects the low mode frequency components to a limited degree. When the crack is between 9 m and 10.25 m, as seen in Figure 5-7, very little difference can be observed in terms of frequency (peak locations). A larger difference can be observed when the crack is between 9 m and 14.35 m, as seen in Figure 5-8. In particular, the flapwise excitation can excite the flapwise vibration (1st mode) more significantly, as shown in Figure 5-8 (a). This is more reflected in the signal collected from the point closer to the damage location. Furthermore, with debonding crack damage, the 1st edgewise motion can be more likely to be excited in the edgewise direction, as illustrated in Figure 5-8 (b).

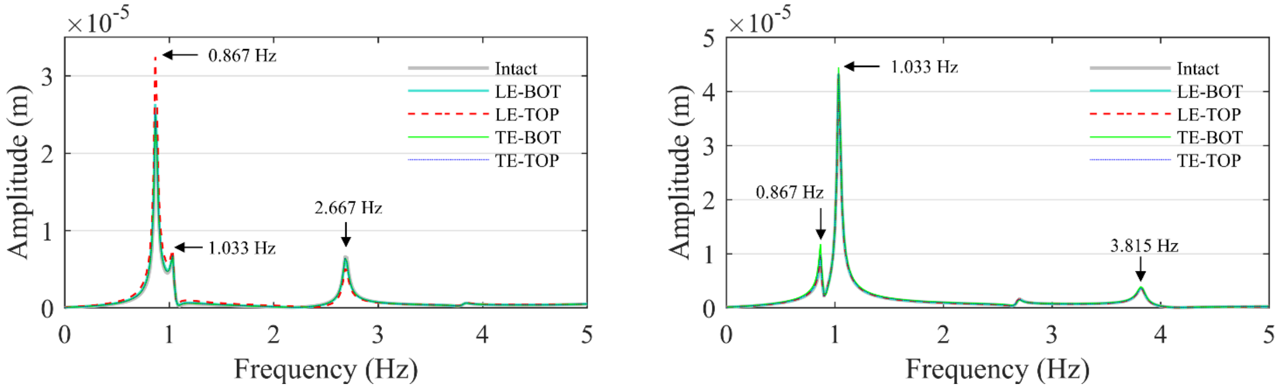

(a) Excite: flapwise & Collect (@Top-5): flapwise

(b) Excite: edgewise & Collect (@BOT-6): flapwise

Figure 5-7: FFT results of representative displacements collected from free vibration simulation of WTB with a pre-existing debonding crack located in 4 different locations between 9 m and 10.25 m

Regarding the relationship between the sensor location and the signal separation between intact and damaged cases, signal collections from the near-crack points perform much better than distant points, and signal collections on the BOT & TOP sets are relatively better than LE & TE sides. However, free vibration testing is ineffective for damage inference based on time series signals or their FFT, which could require advanced algorithms (e.g., using artificial intelligence trained by large amounts of data).

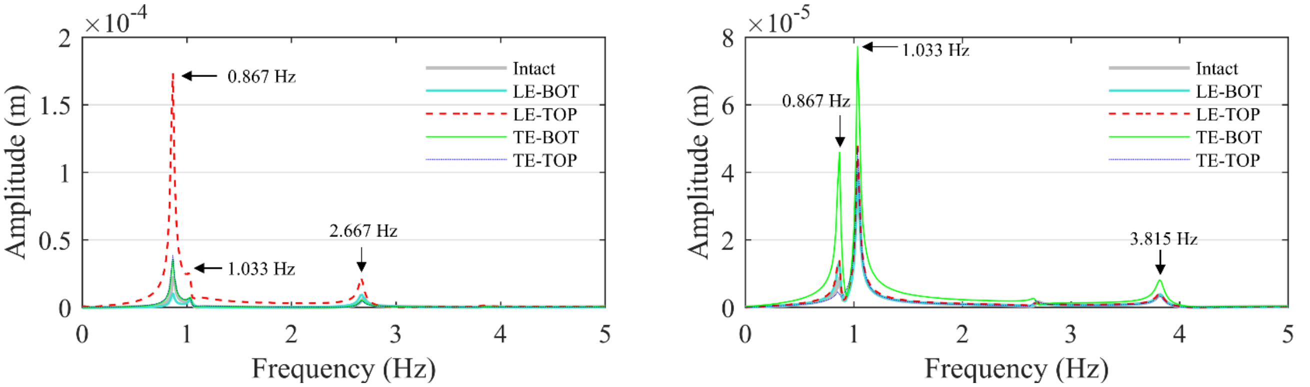

(a) Excite: flapwise & Collect (@TOP-5): flapwise

(b) Excite: edgewise & Collect (@BOT-6): flapwise

Figure 5-8: FFT results of representative displacements collected from free vibration simulation of WTB with a pre-existing debonding crack located in 4 different locations between 9 m and 14.35 m

5.3 Impact load analysis

5.3.1 Impact load analysis setup

To simulate the hammer testing for the 5-MW blade, an impact load analysis is applied to the WTB with the impact load (i.e., amplitude 1.2 kN within 0.2 sec) defined with reference to [301], where the load curve is shown in Figure 5-9.

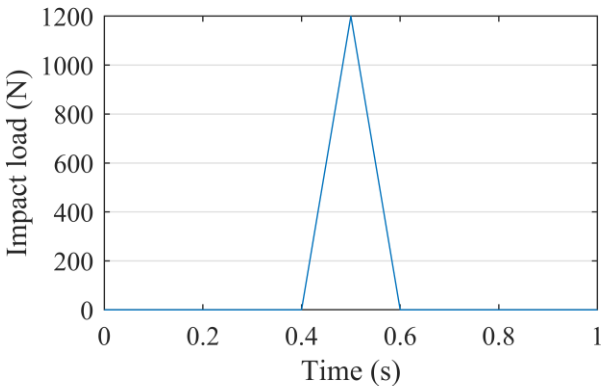

Figure 5-9: Load curve of hammer impact testing for the 5-MW blade

The hitting and sensor installation locations are critical for hammer impact testing. To explore different possibilities, the 18 (= 6+3+6+3) points defined earlier for signal collection in free vibration test simulations are used as hitting points to apply impact loads, see Figure 5-10; 14 (=

7 +7) additional points distributed on the top and bottom surfaces around the critical regions (9-10.25 m) are also considered as hitting points. These hitting points are illustrated in Figure 5-10 with exact spanwise positions indicated. The impact load is applied in the flapwise (Y) direction toward the blade surfaces (TOP and BOT). However, impact load is applied in both flapwise (Y) and edgewise (X) directions for the leading and trailing edges. The dynamic responses triggered by impact load excitation are collected in X, Y, and Z directions for all the 52 signal collection points and newly added 14 (=7+7) hitting points.

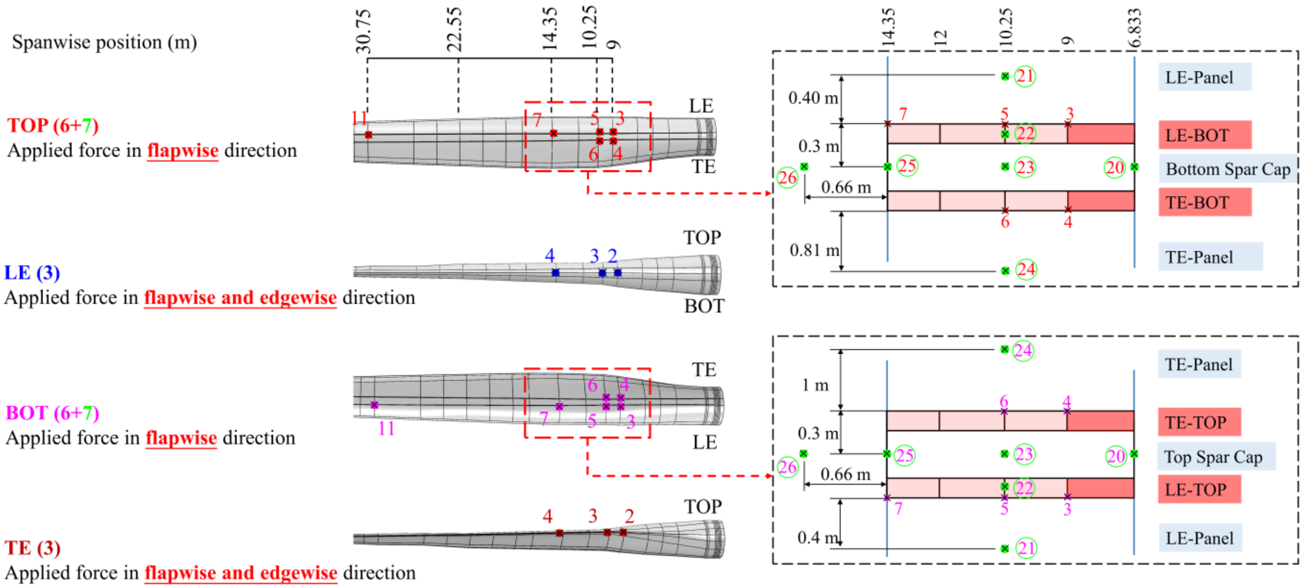

Figure 5-10: Hitting positions for hammer impact tests simulations

5.3.2 Impact load analysis results

In contrast to free vibration test simulations, vibration signals from impact load test simulations contain more high-frequency components. As shown in Figure 5-11, for the WTB with a relatively large debonding crack length (9 m to 14.35 m), higher vibration modes of the WTB are excited based on the responses collected in the flapwise direction.

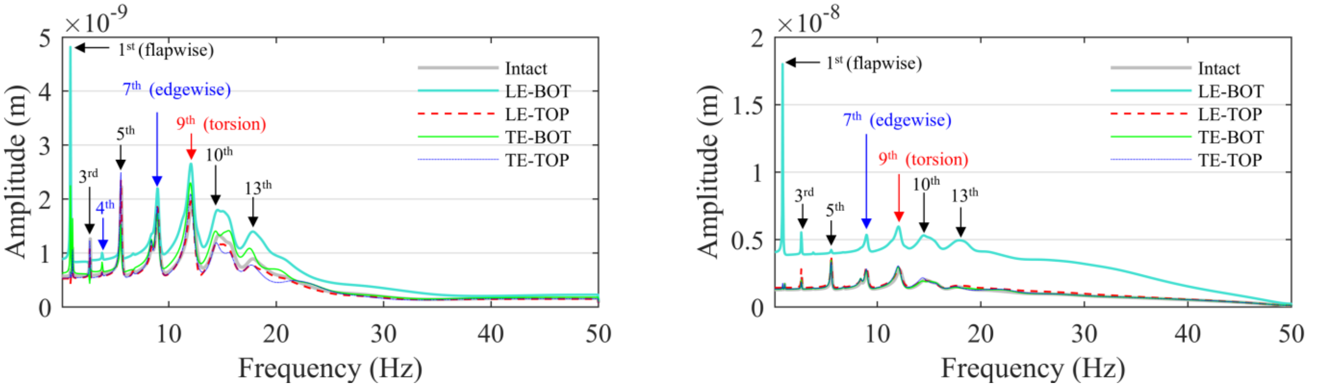

(a) Impact (@BOT-5): flapwise & Collect (@BOT-6): flapwise

(b) Impact (@BOT-5): flapwise & Collect (@BOT-5): flapwise

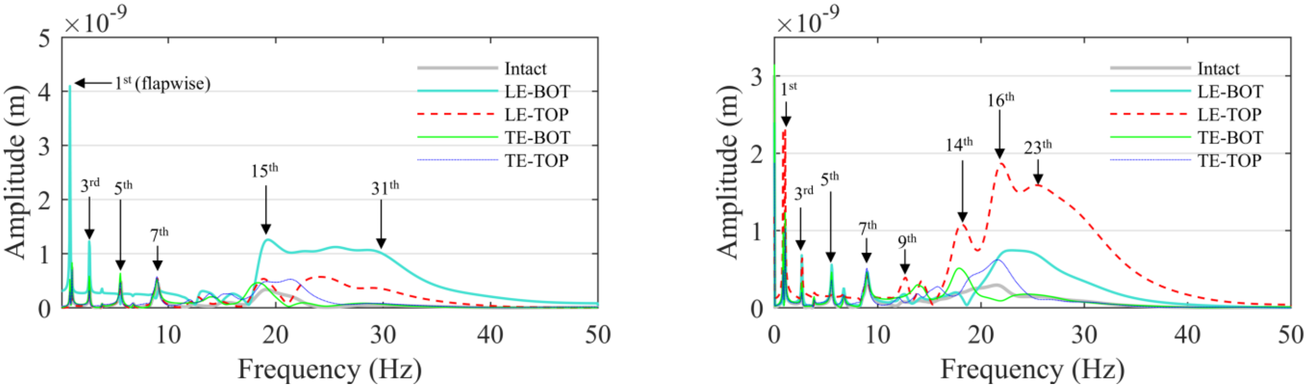

(c) Impact (@LE-3): edgewise & Collect (@BOT-5): flapwise

(d) Impact (@LE-3): edgewise & Collect (@TOP-5): flapwise

Figure 5-11: FFT results of representative displacements collected from impact load simulation of WTB with a pre-existing debonding crack located in 4 different locations between 9 m and 14.35 m

Comparing the signals collected at different points from WTBs without and with debonding cracks at different locations (i.e., LE-BOT, LE-TOP, TE-BOT, TE-TOP), it is found that the closer the hitting point is to the debonding location, the more likely to see the signal discrepancy between the defective WTB and the intact WTB, regardless of the locations of the hitting points and signal collection points. For example, according to Figure 5-11 (a) & (b), when WTB is hit at point #5 in the flapwise direction on the bottom (BOT-5) that is closer to the LE (see Figure 5-10), the WTB with debonding at LE-BOT shows the most different signal from the WTB without debonding. Similarly, according to Figure 5-11 (c) & (d), when WTB is hit at point #3 in the edgewise direction on the leading edge (LE-3) (see Figure 5-10), the WTB with debonding at LE-BOT and LE-TOP shows the most different signal from the WTB without debonding, respectively, depending on the signal collection point (at BOT or TOP). This suggests that in impact load tests, hitting points (e.g., flapwise on the BOT or TOP surfaces, edgewise on the LE or TE) should be located at the following 4 locations in the transverse direction, i.e., LE-BOT, LE-TOP, TE-BOT, TE-TOP. If possible, the signal collection points should be close to the hitting points, as indicated by Figure 5-11 (b).

Furthermore, in the spanwise direction, the hitting point within the debonding area, around 10.25 m (e.g., point 23 on the bottom), is found to be more effective for damage detection. This is because, as shown in Figure 5-12, more different signals can be observed when the hitting point is within the debonding area (@BOT-23) compared with the case when the hitting point is further away (e.g., @BOT-24, which is located at the boundary of the debonding crack in the span-wise direction).

According to Figure 5-11 and Figure 5-12, it can be noticed that the frequency characteristics are similar regardless of the impact applied and the signal collection points. The 1st mode amplitude and the high-frequency range (e.g., > 20Hz) are usually most affected, while it is potential to have the vibration magnitudes magnified at almost all frequency contents due to debonding damage in certain scenarios, see Figure 5-11 (b) and Figure 5-12 (a). In particular, if the impact is applied and data is collected at the same site, which is located at the points of BOT and TOP series with a 10.25 m span, more significant signals will be triggered for specific damage inference, such as BOT-5 for WTB with debonding located in LE-BOT, BOT-6 for WTB with debonding located in TE-BOT, TOP-5 for WTB with debonding located in LE-TOP, and TOP-6 for WTB with debonding located in TE-TOP. These points are located at the most critical span of 10.25 m, as illustrated in Figure 5-13.

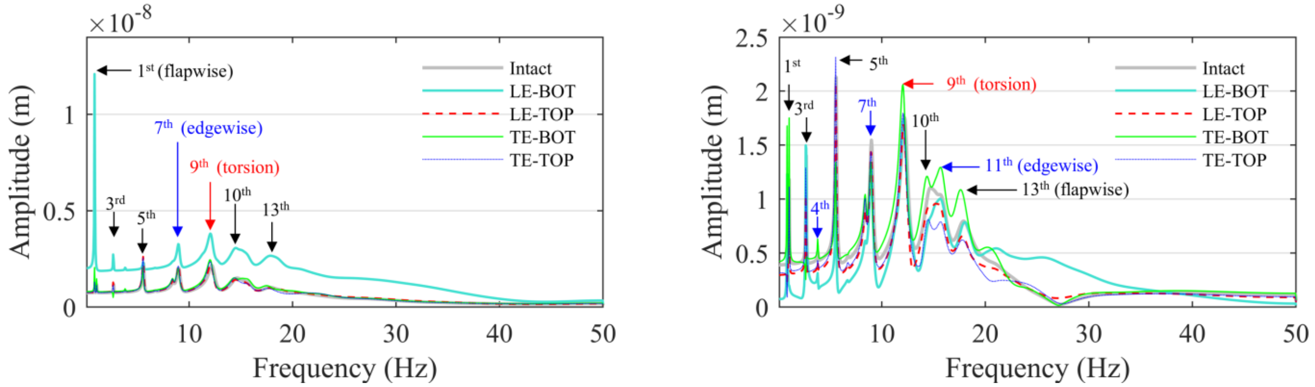

(a) Impact (@BOT-23): flapwise & Collect (@BOT-5): flapwise

(b) Impact (@BOT-24): flapwise & Collect (@BOT-5): flapwise

Figure 5-12: Comparison of the spanwise location of the hitting points for WTB with a pre-existing debonding crack (between 9 m and 14.35 m) located in 4 different locations

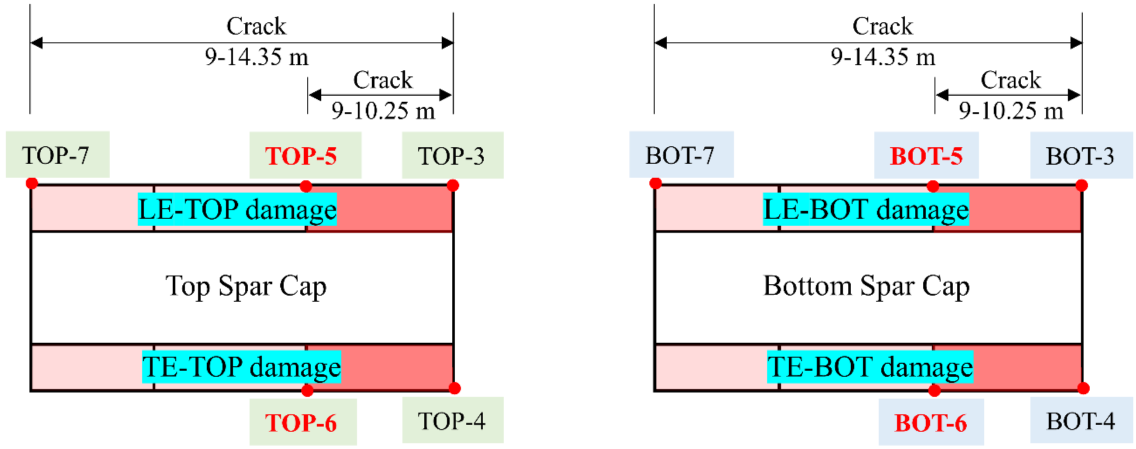

(a) Top side

(b) Bottom side

Figure 5-13: Special damage-detection points illustration

It is worth noting that although impact load testing proves to be more effective for damage inference based on the discrepancy between the vibration signals from the WTB with debonding cracks and the intact WTB, impact load testing for deboning damage inference remains challenging for small debonding crack sizes. For example, similar to free vibration test simulation, the dynamic behavior of WTBs with a relatively smaller debonding crack (9 m-10.25 m) is not much influenced by the debonding damage. But when the debonding crack size is large, vibration-based techniques, particularly impact load testing with appropriate selection of the hitting points and signal collection points, can be potentially used in practice. (give figures with small crack size).

5.4 Discussion

Chapter 5 simulated the WTBs with and without debonding damage for two vibration-based techniques (i.e., free vibration and impact load analysis), aiming to investigate the dynamic behaviors under two sizes of cap-web debonding damage and to provide useful information for the debonding inference in practice.

It is found that free vibration can not reflect the debonding damage in terms of frequency change (as frequently used in structural health monitoring), and it is hard to trigger the responses within a lower frequency component (i.e., 0-5 Hz). Thus, no frequency shifts in the collected signals do not imply no debonding damage in WTBs. Nevertheless, the cap-web debonding damage can lead to the separated amplitude of vibration signals. And the larger debonding size (9-14.35 m) is inclined to have more amplitude separation than the small case (9-10.25 m). This amplitude increment might imply the potential utilization of free vibration for future debonding inference if advanced algorithms are introduced (e.g., machine learning using artificial intelligence trained by large amounts of data). Some beneficial vibrated characteristics are derived from free vibration analysis, which might contribute to further research. For example, the amplitude differences mainly reflect at specific frequency bands, especially the 1st flapwise (0.867 Hz) and 1st edgewise (1.033 Hz) modes rather than the 2nd flapwise or edgewise modes. And the vibration signals in the Y-direction have the best-separated amplitude due to the exiting debonding damage than the other orientations. Furthermore, higher divergent signals are inclined to be triggered by flapwise excitation rather than edgewise, and are more likely collected at crack-nearby sites, especially 9-10.25 m span, the hotspot area in the debonding simulation.

On the other hand, impact load analysis can trigger the vibrational signals within more high-frequency components, and the hidden damage can be revealed based on adequate hitting points and data collection at crack-nearby points. It is discovered that the signal discrepancy between the defective WTB and the intact WTB is more likely to be observed the closer the impact point is to the debonding location, regardless of the locations of the impacting points and signal collection sites. Particularly, the spanwise hitting point within the debonding area around 9-10.25 m from the WTB root is more effective for damage inference than distant points, where the impact applied at 10.25 m performed best. To trigger more divergent signals, the impact hitting on the bottom or top surfaces, and LE or TE sides, should be in flapwise and edgewise directions, respectively. In addition, if the impact application and data collection are conducted at the same location, more significant damage inference signals will be generated. Some notable points located at the 10.25 m span are more significant in the damage inference for specific damage types, such as BOT-5 for LE-BOT damage, BOT-6 for TE-BOT damage, TOP-5 for LE-TOP damage, and TOP-6 for TE-TOP damage. The frequency characteristics derived from impact testing are comparable regardless of the applied force and signal collection points. Due to debonding damage, the 1st mode amplitude and the high-frequency range (e.g., > 20Hz) are typically most affected, whereas the vibration magnitudes may be amplified at nearly all frequency contents in certain circumstances.

To summarize, in impact load tests, hitting points (e.g., flapwise on the BOT or TOP surfaces, edgewise on the LE or TE) should be located at the following 4 locations in the transverse direction, i.e., LE-BOT, LE-TOP, TE-BOT, TE-TOP. In the spanwise direction, the hitting point within the debonding area, around 10.25 m (e.g., point 23 on the bottom), is found to be more effective for damage detection.

CHAPTER 6:CONCLUSIONS AND FUTURE WORK RECOMMENDATIONS

6.1 Summary and conclusions

This study performed debonding and vibration simulations of the NREL 61.5 m 5-MW blade. The pre-knowledge of the hotspot for cap-web debonding is identified, and then the propagation behavior with existing cracks is determined. Also, vibration simulations are conducted to inform two vibration-based techniques (i.e., free vibration and impact load analysis) by comparing the dynamic characteristics of the 5-MW blade with and without debonding damage. Such knowledge will be used to guide the development of vibration-based diagnostic techniques for effective debonding detection and severity assessment of wind turbine blades.

(1) It is found that the cap-web connection within a 9-10.25 m span of the studied WTB is more vulnerable to debonding damage and thus determined as the debonding hotspot. Also, the existing cracks likely propagate mainly within the hotspot area.

(2) The vibration simulation results indicate that the cap-web debonding is less likely to be uncovered by vibration signals, particularly via free vibration testing. Free vibration testing can barely excite high-frequency components of WTBs with and without debonding damage. The cap-web debonding damage can only be reflected in the amplitude of vibration signals. Thus no frequency shifts in the collected signals do not imply no debonding damage in WTBs. However, free vibration of WTB with a larger debonding size will increase amplitude separation, and this implies the potential of the free vibration method for debonding damage inference if more advanced approaches are used (e.g., model updating approach).

(3) When impact load testing is used for WTBs with relatively large debonding cracks, adequate hitting points and signal collection points (i.e., near crack) can reveal the hidden damage. It is found that when the hitting point is closer to the debonding location, more signal discrepancy between the defective WTB and the intact WTB can be observed. Since it is possible to have debonding at the following 4 locations in the transverse direction, i.e., LE-BOT, LE-TOP, TE-BOT, TE-TOP, hitting points in impact load tests (e.g., flapwise on the BOT or TOP surfaces, edgewise on the LE or TE) should be located at those 4 locations in the transverse direction. In the spanwise direction, the hitting point within the debonding area, particularly around 10.25

m from the WTB root, is found to be effective for damage detection. Furthermore, the signal collection points should be as close as possible to the hitting points.

6.2 Limitations and future work recommendations

This thesis work is limited to investigating cap-web debonding inference for vibration techniques. Based on the limitations of this work, the following work is recommended

(1) Further research work is needed to use the amplitude differences in signals collected from free vibration analysis for debonding inference in practice, where some advanced algorithms and data-based machine learning need to be introduced.

(2) The signals simulated are noise-free, while in real engineering practice, signals are contaminated with measurement noise. The effectiveness of vibration-based data for debonding detection needs further analysis using measured signals using accelerometers and velocity sensors.

(3) The small debonding crack size cannot be revealed by vibration methods readily, and other methods need to be studied theoretically and experimentally.

(4) This thesis only focused on debonding damage between shear webs and the spar cap. The effect of other types of damage needs to be studied as well.

REFERENCES

[1] X. Wang, Hasi Eerdun, Z. Zhou, and X. Liu, “Significance of variations in the wind energy environment over the past 50 years with respect to dune activity and desertification in arid and semiarid northern China,” *Geomorphology*, vol. 86, no. 3, pp. 252–266, May 2007, doi: 10.1016/j.geomorph.2006.09.003.

[2] M. Wolsink, “Wind power and the NIMBY-myth: institutional capacity and the limited significance of public support,” *Renew. Energy*, vol. 21, no. 1, pp. 49–64, Sep. 2000, doi: 10.1016/S0960-1481(99)00130-5.

[3] “Advantages and Challenges of Wind Energy,” *Energy.gov*. https://www.energy.gov/eere/wind/advantages-and-challenges-wind-energy (accessed Oct. 24, 2022).

[4] R. H. Barnes and E. V. Morozov, “Structural optimisation of composite wind turbine blade structures with variations of internal geometry configuration,” *Compos. Struct.*, vol. 152, pp. 158–167, Sep. 2016, doi: 10.1016/j.compstruct.2016.05.013.

[5] M. Jureczko, M. Pawlak, and A. Mężyk, “Optimisation of wind turbine blades,” *J. Mater. Process. Technol.*, vol. 167, no. 2, pp. 463–471, Aug. 2005, doi: 10.1016/j.jmatprotec.2005.06.055.

[6] S. Mein, “Top 3 Types of Wind Turbine Failure.” http://www.firetrace.com/fire-protection-blog/wind-turbine-failure (accessed Oct. 27, 2022).

[7] D. Li, S.-C. M. Ho, G. Song, L. Ren, and H. Li, “A review of damage detection methods for wind turbine blades,” *Smart Mater. Struct.*, vol. 24, no. 3, p. 033001, 2015.

[8] A. C. Garolera, S. F. Madsen, M. Nissim, J. D. Myers, and J. Holboell, “Lightning damage to wind turbine blades from wind farms in the US,” *IEEE Trans. Power Deliv.*, vol. 31, no. 3, pp. 1043–1049, 2014.

[9] B. F. Sørensen *et al.*, “Improved design of large wind turbine blade of fibre composites based on studies of scale effects (Phase 1)-Summary Report,” 2004.

[10] N. Beganovic and D. Söffker, “Structural health management utilization for lifetime prognosis and advanced control strategy deployment of wind turbines: An overview and outlook concerning actual methods, tools, and obtained results,” *Renew. Sustain. Energy Rev.*, vol. 64, pp. 68–83, 2016.

[11] C. C. Ciang, J.-R. Lee, and H.-J. Bang, “Structural health monitoring for a wind turbine system: a review of damage detection methods,” *Meas. Sci. Technol.*, vol. 19, no. 12, p. 122001, 2008.

[12] A. Lamarre, “Improved inspection of composite wind turbine blades with accessible advanced ultrasonic phased array technology,” in *15th Asia Pacific Conference for Non-Destructive Testing (APCNDT2017), Singapore*, 2017, pp. 1–8.

[13] J. Tang and X. Chen, “Experimental investigation on ultimate strength and failure response of composite box beams used in wind turbine blades,” *Compos. Struct.*, vol. 198, pp. 19–34, 2018.

[14] Y.-J. Jang, H.-J. Kim, H.-G. Kim, and K.-W. Kang, “Identification of Debonding Damage at Spar Cap-Shear Web Joints by Artificial Neural Network Using Natural Frequency Relevant Key Features of Composite Wind Turbine Blades,” *Appl. Sci.*, vol. 11, no. 12, p. 5327, Jun. 2021, doi: 10.3390/app11125327.

[15] X. Chen *et al.*, "Fatigue testing of a 14.3 m composite blade embedded with artificial defects–damage growth and structural health monitoring," *Compos. Part Appl. Sci. Manuf.*, vol. 140, p. 106189, 2021.

[16] J. Yang *et al.*, "Structural investigation of composite wind turbine blade considering structural collapse in full-scale static tests," *Compos. Struct.*, vol. 97, pp. 15–29, 2013.

[17] X. Chen, W. Zhao, X. L. Zhao, and J. Z. Xu, "Failure test and finite element simulation of a large wind turbine composite blade under static loading," *Energies*, vol. 7, no. 4, pp. 2274–2297, 2014.

[18] F. M. Jensen, B. G. Falzon, J. Ankersen, and H. Stang, "Structural testing and numerical simulation of a 34 m composite wind turbine blade," *Compos. Struct.*, vol. 76, no. 1–2, pp. 52–61, 2006.

[19] Y. Du, S. Zhou, X. Jing, Y. Peng, H. Wu, and N. Kwok, "Damage detection techniques for wind turbine blades: A review," *Mech. Syst. Signal Process.*, vol. 141, p. 106445, 2020.

[20] Ł. Doliński, M. Krawczuk, and A. Żak, "Detection of Delamination in Laminate Wind Turbine Blades Using One-Dimensional Wavelet Analysis of Modal Responses," *Shock Vib.*, vol. 2018, p. e4507879, Mar. 2018, doi: 10.1155/2018/4507879.

[21] S. Hoell and P. Omenzetter, "Optimal selection of autoregressive model coefficients for early damage detectability with an application to wind turbine blades," *Mech. Syst. Signal Process.*, vol. 70–71, pp. 557–577, Mar. 2016, doi: 10.1016/j.ymssp.2015.09.007.

[22] M. D. Ulriksen, D. Tcherniak, P. H. Kirkegaard, and L. Damkilde, "Operational modal analysis and wavelet transformation for damage identification in wind turbine blades," *Struct. Health Monit.*, vol. 15, no. 4, pp. 381–388, 2016.

[23] "What Is the Future of Wind Energy?," *Caltech Science Exchange*. http://scienceexchange.caltech.edu/topics/sustainability/wind-energy-advantages-disadvantages (accessed Oct. 24, 2022).

[24] "Global Electricity Review 2022," *Ember*, Mar. 29, 2022. https://ember-climate.org/insights/research/global-electricity-review-2022/ (accessed Oct. 24, 2022).

[25] P. Sadorsky, "Wind energy for sustainable development: Driving factors and future outlook," *J. Clean. Prod.*, vol. 289, p. 125779, Mar. 2021, doi: 10.1016/j.jclepro.2020.125779.

[26] S. Williams, T. Acker, M. Goldberg, and M. Greve, "Estimating the economic benefits of wind energy projects using Monte Carlo simulation with economic input/output analysis," *Wind Energy*, vol. 11, pp. 397–414, Jul. 2008, doi: 10.1002/we.273.

[27] "Wind Vision," *Energy.gov*. https://www.energy.gov/eere/wind/wind-vision-1 (accessed Oct. 24, 2022).

[28] "Canadian Renewable Energy Association - Wind. Solar. Storage." https://renewablesassociation.ca/ (accessed Oct. 24, 2022).

[29] "Comprehensive Renewable Energy," *ScienceDirect*. http://www.sciencedirect.com:5070/referencework/9780080878737/comprehensive-renewable-energy (accessed Oct. 24, 2022).

[30] T. Price, "James Blyth — Britain's First Modern Wind Power Pioneer," *Wind Eng.*, vol. 29, pp. 191–200, May 2005, doi: 10.1260/030952405774354921.

[31] U. authorUnknown author, *English: Charles F. Brush's 60 foot, 80,000 pound turbine that supplied 12kW of power to 350 incandescent lights, 2 arc lights, and a number of motors at his home for 20 years. It today is believed to be the first automatically operating wind turbine for electricity generation and was built in the winter of 1887 - 1888 in his back yard. Its rotor*

was 17 meters in diameter. The large rectangular shape to the left of the rotor is the vane, used to move the blades into the wind. The dynamo turned 50 times for every revolution of the blades and charged a dozen batteries each with 34 cells. For scale, note gardener pushing lawnmower underneath and to right of the turbine. 1888. Accessed: Oct. 24, 2022. [Online]. Available: https://commons.wikimedia.org/wiki/File:Wind_turbine_1888_Charles_Brush.jpg

[32] "Smith–Putnam wind turbine," *Wikipedia*. Aug. 27, 2022. Accessed: Oct. 24, 2022. [Online]. Available: https://en.wikipedia.org/w/index.php?title=Smith%E2%80%93Putnam_wind_turbine&oldid=1106965595

[33] Z. Shahan, "History of Wind Turbines," *Renewable Energy World*, Nov. 21, 2014. https://www.renewableenergyworld.com/storage/history-of-wind-turbines/ (accessed Oct. 24, 2022).

[34] "Accelerating Scotland's leadership in floating offshore wind," *https://www.carbontrust.com/our-work-and-impact/impact-stories/accelerating-scotlands-leadership-in-floating-offshore-wind*, Dec. 07, 2020. https://www.carbontrust.com/our-work-and-impact/impact-stories/accelerating-scotlands-leadership-in-floating-offshore-wind (accessed Apr. 09, 2023).

[35] R. (Denmark) BTM Consult ApS, "International wind energy development World market update 2000 Forecast 2001-2005," Denmark, 87-987788-1–1, 2001.

[36] "Wind power generation," *Our World in Data*. https://ourworldindata.org/grapher/wind-generation (accessed Oct. 24, 2022).

[37] J. Dorrell and K. Lee, "The Cost of Wind: Negative Economic Effects of Global Wind Energy Development," *Energies*, vol. 13, no. 14, Art. no. 14, Jan. 2020, doi: 10.3390/en13143667.

[38] P. Beiter, J. T. Rand, J. Seel, E. Lantz, P. Gilman, and R. Wiser, "Expert perspectives on the wind plant of the future," *Wind Energy*, vol. 25, no. 8, pp. 1363–1378, Aug. 2022, doi: 10.1002/we.2735.

[39] R. Wiser *et al.*, "Expert elicitation survey predicts 37% to 49% declines in wind energy costs by 2050," *Nat. Energy*, vol. 6, no. 5, pp. 555–565, May 2021, doi: 10.1038/s41560-021-00810-z.

[40] J. C. Bean, "Betz's law - Wikipedia," p. 8.

[41] T. Burton, Ed., *Wind energy: handbook*. Chichester ; New York: J. Wiley, 2001.

[42] "Wind Turbines | SpringerLink." https://link.springer.com/book/10.1007/3-540-29284-5 (accessed Oct. 24, 2022).

[43] "Power Conversion and Control of Wind Energy Systems | Wiley," *Wiley.com*. https://www.wiley.com/en-ca/Power+Conversion+and+Control+of+Wind+Energy+Systems-p-9780470593653 (accessed Sep. 13, 2022).

[44] "Wind Turbines: Fundamentals, Technologies, Application, Economics: Hau, Erich, Renouard, Horst: 9783642271502: Books - Amazon.ca." https://www.amazon.ca/Wind-Turbines-Fundamentals-Technologies-Application/dp/3642271502 (accessed Oct. 25, 2022).

[45] P. J. Schubel and R. J. Crossley, "Wind Turbine Blade Design," *Energies*, vol. 5, no. 9, pp. 3425–3449, Sep. 2012, doi: 10.3390/en5093425.

[46] J. Bukała *et al.*, "Small Wind Turbines: Specification, Design, and Economic Evaluation," 2016. doi: 10.5772/62821.

[47] E. I. Konstantinidis and P. N. Botsaris, “Wind turbines: current status, obstacles, trends and technologies,” *IOP Conf. Ser. Mater. Sci. Eng.*, vol. 161, no. 1, p. 012079, Nov. 2016, doi: 10.1088/1757-899X/161/1/012079.

[48] A. & B. LLP, “Ontario to Cancel White Pines Wind Project,” *Aird & Berlis LLP*, Jul. 11, 2018. https://www.airdberlis.com/insights/blogs/energyinsider/post/ei-item/ontario-to-cancel-white-pines-wind-project (accessed Feb. 27, 2023).

[49] “Wind power | Capacity & Facts | Britannica,” Feb. 15, 2023. https://www.britannica.com/science/wind-power (accessed Feb. 27, 2023).

[50] J. F. Manwell, “Wind Energy Explained: Theory, Design and Application,” p. 705.

[51] F. Castellani, D. Astolfi, M. Peppoloni, F. Natili, D. Buttà, and A. Hirschl, “Experimental Vibration Analysis of a Small Scale Vertical Wind Energy System for Residential Use,” *Machines*, vol. 7, no. 2, Art. no. 2, Jun. 2019, doi: 10.3390/machines7020035.

[52] L. Battisti, A. Brighenti, E. Benini, and M. R. Castelli, “Analysis of Different Blade Architectures on small VAWT Performance,” *J Phys Conf Ser*, vol. 753, 2016, Accessed: Oct. 25, 2022. [Online]. Available: https://cyberleninka.org/article/n/1441871

[53] L. Battisti *et al.*, “Experimental benchmark data for H-shaped and troposkien VAWT architectures,” *Renew. Energy*, vol. 125, no. C, pp. 425–444, 2018.

[54] R. Gupta, A. Biswas, and K. K. Sharma, “Comparative study of a three-bucket Savonius rotor with a combined three-bucket Savonius–three-bladed Darrieus rotor,” *Renew. Energy*, vol. 33, no. 9, p. 1974, 2008.

[55] M. A. Hyams, “20 - Wind energy in the built environment,” in *Metropolitan Sustainability*, F. Zeman, Ed., in Woodhead Publishing Series in Energy. Woodhead Publishing, 2012, pp. 457–499. doi: 10.1533/9780857096463.3.457.

[56] J. W. Burchell, “Advancement of Direct Drive Generator Systems for Offshore Renewable Energy Production,” p. 276.

[57] “UGE raises the bar for vertical axis micro wind turbines with launch of new VisionAIR3 turbine. | Micro wind turbine, Wind power generator, Wind turbine,” *Pinterest*. https://www.pinterest.com/pin/394276142378835936/ (accessed Oct. 25, 2022).

[58] “Vertical-axis wind turbine,” *Wikipedia*. Feb. 15, 2023. Accessed: Feb. 27, 2023. [Online]. Available: https://en.wikipedia.org/w/index.php?title=Vertical-axis_wind_turbine&oldid=1139450079

[59] W. Musial and S. Butterfield, “Future for Offshore Wind Energy in the United States: Preprint,” National Renewable Energy Lab., Golden, CO (US), NREL/CP-500-36313, Jun. 2004. Accessed: Oct. 25, 2022. [Online]. Available: https://www.osti.gov/biblio/15007876

[60] M. S. Mayeed and A. Khalid, “Optimization of the Wind Turbine Designs for Areas With Low Wind Speeds,” presented at the ASME 2015 9th International Conference on Energy Sustainability collocated with the ASME 2015 Power Conference, the ASME 2015 13th International Conference on Fuel Cell Science, Engineering and Technology, and the ASME 2015 Nuclear Forum, American Society of Mechanical Engineers Digital Collection, Oct. 2015. doi: 10.1115/ES2015-49052.

[61] R. Gasch and J. Twele, *Wind Power Plants: Fundamentals, Design, Construction and Operation*. Springer Science & Business Media, 2011.

[62] J. Widén *et al.*, “Variability assessment and forecasting of renewables: A review for solar, wind, wave and tidal resources,” *Renew. Sustain. Energy Rev.*, vol. 44, pp. 356–375, Apr. 2015, doi: 10.1016/j.rser.2014.12.019.

[63] “UK governments boost to renewable energy sector | Freedomsat,” *Freedomsat A Bentley Walker Service - Delivering Fibre, 4G & Satellite Broadband Internet To The UK & Europe*, Jan. 29, 2021. https://www.freedomsat.co.uk/news/wind-farm-internet-solutions (accessed Feb. 27, 2023).

[64] I. CORPORATIVA, “Vineyard Wind 1, our first offshore wind farm in the United States,” *Iberdrola*. https://www.iberdrola.com/about-us/what-we-do/offshore-wind-energy/vineyard-wind-offshore-wind-farm (accessed Feb. 27, 2023).

[65] F. Khater, *Development in wind energy technology: an update*. 2012, p. 105.

[66] E. Tohme, “Report About Wind Turbines Prepared by 4 th year Mechanical Engineering Students Lebanese University Faculty of Engineering Roomieh,” Apr. 2014. doi: 10.13140/2.1.2534.6241.

[67] N. N. UpWind, “Design limits and solutions for very large wind turbines,” *EWEA Bruss. Belg.*, 2011.

[68] P. E. Morthorst and L. Kitzing, “2 - Economics of building and operating offshore wind farms,” in *Offshore Wind Farms*, C. Ng and L. Ran, Eds., Woodhead Publishing, 2016, pp. 9–27. doi: 10.1016/B978-0-08-100779-2.00002-7.

[69] “The European offshore wind industry - key trends and statistics 2016,” *WindEurope*, Jan. 26, 2017. https://windeurope.org/about-wind/statistics/offshore/european-offshore-wind-industry-key-trends-and-statistics-2016/ (accessed Oct. 25, 2022).

[70] “World’s Most Powerful Offshore Wind Platform: Haliade-X | GE Renewable Energy.” https://www.ge.com/renewableenergy/wind-energy/offshore-wind/haliade-x-offshore-turbine (accessed Oct. 25, 2022).

[71] “MINGYANG SMART ENERGY.” http://www.myse.com.cn/en/jtxw/info.aspx?itemid=825 (accessed Oct. 25, 2022).

[72] R. Wiser, M. Hand, J. Seel, and B. Paulos, “Reducing wind energy costs through increased turbine size: Is the sky the limit,” *Rev Berkeley Natl. Lab. Electr. Mark. Policy Group*, vol. 121, 2016.

[73] R. Wiser *et al.*, “2016 Wind Technologies Market Report,” p. 95.

[74] R. H. Wiser and M. Bolinger, “2018 wind technologies market report,” 2019.

[75] M. Bolinger, E. Lantz, R. Wiser, B. Hoen, J. Rand, and R. Hammond, “Opportunities for and challenges to further reductions in the ‘specific power’ rating of wind turbines installed in the United States,” *Wind Eng.*, vol. 45, no. 2, pp. 351–368, Apr. 2021, doi: 10.1177/0309524X19901012.

[76] P. Malhotra, “Advanced Blade Testing Methods for Wind Turbines,” p. 89.

[77] M. Peeters, G. Santo, J. Degroote, and W. Paepegem, “The Concept of Segmented Wind Turbine Blades: A Review,” *Energies*, vol. 10, no. 8, p. 1112, Jul. 2017, doi: 10.3390/en10081112.

[78] “Solving the Problem with Wind Turbine Blade Disposal,” *AZoCleantech.com*, Apr. 08, 2021. https://www.azocleantech.com/article.aspx?ArticleID=1209 (accessed Mar. 04, 2023).

[79] “Structural reuse of wind turbine blades through segmentation | Elsevier Enhanced Reader.” https://reader.elsevier.com/reader/sd/pii/S2666682021000323?token=3B65E3BB0B36FDBC334C4F6609E6D5708B193D956A4617CFC060B9AD5015DE34E48DA1E8C7427EE7DBE5249D8C6B824C&originRegion=us-east-1&originCreation=20220927165350 (accessed Sep. 27, 2022).

[80] X. Huang, S. M. Alavi Moghadam, P. Meysonnat, M. Meinke, and W. Schröder, “Numerical analysis of the effect of flaps on the tip vortex of a wind turbine blade,” *Int. J. Heat Fluid Flow*, vol. 77, pp. 336–351, May 2019, doi: 10.1016/j.ijheatfluidflow.2019.05.004.

[81] J. Thirstrup Petersen *et al.*, “Prediction of dynamic loads and induced vibrations in stall,” 1998.

[82] K. A. Braun, A. Gordner, F. Hailer, B. Huurdeman, H. Arnold, and M. Müller, “Some blade tip modifications and their influence on aeroacoustics,” 1996.

[83] K. Dykes *et al.*, “Effect of Tip-Speed Constraints on the Optimized Design of a Wind Turbine,” NREL/TP-5000-61726, 1159782, Oct. 2014. doi: 10.2172/1159782.

[84] B. Resor, “Definition of a 5MW/61.5m wind turbine blade reference model.,” SAND2013-2569, 1095962, 463454, Apr. 2013. doi: 10.2172/1095962.

[85] R. Chow, *Computational investigations of inboard flow separation and mitigation techniques on multi-megawatt wind turbines*. University of California, Davis, 2011.

[86] C. Arakawa, O. Fleig, M. Iida, and M. Shimooka, “Numerical approach for noise reduction of wind turbine blade tip with earth simulator,” *J. Earth Simulator*, vol. 2, no. 3, pp. 11–33, 2005.

[87] J. Johansen and N. N. Sørensen, “Numerical investigation of three wind turbine blade tips,” 2002.

[88] E. Ferrer and X. Munduate, “Wind turbine blade tip comparison using CFD,” in *Journal of Physics: Conference Series*, IOP Publishing, 2007, p. 012005.

[89] P. H. Nielsen *et al.*, “Design and test of box girder for a large wind turbine blade,” 2012, doi: 10.13140/RG.2.2.10871.21925.

[90] K. M. A. Rafiuddin and N. N. Deshmukh, “Identification of Chord Wise Location of Shear Web for Wind Turbine Blade,” in *2019 International Conference on Nascent Technologies in Engineering (ICNTE)*, Navi Mumbai, India: IEEE, Jan. 2019, pp. 1–5. doi: 10.1109/ICNTE44896.2019.8946070.

[91] F. Sayer, A. Antoniou, and A. van Wingerde, “Investigation of structural bond lines in wind turbine blades by sub-component tests,” *Int. J. Adhes. Adhes.*, vol. 37, pp. 129–135, 2012.

[92] F. M. Jensen, P. M. Weaver, L. S. Cecchini, H. Stang, and R. F. Nielsen, “The Brazier effect in wind turbine blades and its influence on design,” *Wind Energy*, vol. 15, no. 2, pp. 319–333, 2012.

[93] J. Zhu, X. Cai, D. Ma, J. Zhang, and X. Ni, “Improved structural design of wind turbine blade based on topology and size optimization,” *Int. J. Low-Carbon Technol.*, vol. 17, pp. 69–79, Feb. 2022, doi: 10.1093/ijlct/ctab087.

[94] D. T. Griffith and T. D. Ashwill, “The Sandia 100-meter All-glass Baseline Wind Turbine Blade: SNL100-00,” p. 67.

[95] D.-K. Choi, B.-D. Pyeon, S.-Y. Lee, H.-G. Lee, and J.-S. Bae, “Structural Design, Analysis, and Testing of a 10 kW Fabric-Covered Wind Turbine Blade,” *Energies*, vol. 13, no. 12, p. 3276, 2020.

[96] K. van Rijswijk, “Thermoplastic composite wind turbine blades: vacuum infusion technology for anionic polyamide-6 composites,” 2007.

[97] F. Mølholt Jensen and K. Branner, “1 - Introduction to wind turbine blade design,” in *Advances in Wind Turbine Blade Design and Materials*, P. Brøndsted and R. P. L. Nijssen, Eds., in Woodhead Publishing Series in Energy. Woodhead Publishing, 2013, pp. 3–28. doi: 10.1533/9780857097286.1.3.

[98] A. E. Albanesi, I. Peralta, F. Bre, B. A. Storti, and V. D. Fachinotti, “An optimization method based on the evolutionary and topology approaches to reduce the mass of composite wind turbine blades,” *Struct. Multidiscip. Optim.*, vol. 62, no. 2, pp. 619–643, 2020.

[99] M. Ragheb, “Optimal rotor tip speed ratio,” *Lect. Notes Course No NPRE*, vol. 475, 2014.

[100] E. Hau, *Wind turbines: fundamentals, technologies, application, economics*. Springer Science & Business Media, 2013.

[101] J. R. P. Vaz, J. T. Pinho, and A. L. A. Mesquita, “An extension of BEM method applied to horizontal-axis wind turbine design,” *Renew. Energy*, vol. 36, no. 6, pp. 1734–1740, 2011.

[102] Z. C. He, G. R. Liu, Z. H. Zhong, G. Y. Zhang, and A. G. Cheng, “A coupled ES-FEM/BEM method for fluid–structure interaction problems,” *Eng. Anal. Bound. Elem.*, vol. 35, no. 1, pp. 140–147, 2011.

[103] M. A. Golberg, C. S. Chen, and H. Bowman, “Some recent results and proposals for the use of radial basis functions in the BEM,” *Eng. Anal. Bound. Elem.*, vol. 23, no. 4, pp. 285–296, 1999.

[104] H. Glauert, “Airplane propellers,” in *Aerodynamic theory*, Springer, 1935, pp. 169–360.

[105] J.-J. Chattot, “Optimization of wind turbines using helicoidal vortex model,” *J Sol Energy Eng*, vol. 125, no. 4, pp. 418–424, 2003.

[106] M. M. Duquette and K. D. Visser, “Numerical implications of solidity and blade number on rotor performance of horizontal-axis wind turbines,” *J Sol Energy Eng*, vol. 125, no. 4, pp. 425–432, 2003.

[107] M. A. Kotb and M. A. Haq, “A rigid wake model for a horizontal axis wind turbine,” *Wind Eng.*, pp. 95–108, 1992.

[108] P. Fuglsang and H. A. Madsen, “Optimization method for wind turbine rotors,” *J. Wind Eng. Ind. Aerodyn.*, vol. 80, no. 1–2, pp. 191–206, 1999.

[109] W. Xudong, W. Z. Shen, W. J. Zhu, J. N. Sørensen, and C. Jin, “Shape optimization of wind turbine blades,” *Wind Energy Int. J. Prog. Appl. Wind Power Convers. Technol.*, vol. 12, no. 8, pp. 781–803, 2009.

[110] H. Yang, J. Chen, X. Pang, and G. Chen, “A new aero-structural optimization method for wind turbine blades used in low wind speed areas,” *Compos. Struct.*, vol. 207, pp. 446–459, 2019.

[111] R. T. Griffiths, “The effect of aerofoil characteristics on windmill performance,” *Aeronaut. J.*, vol. 81, no. 799, pp. 322–326, 1977.

[112] E. Kulunk, “Aerodynamics of wind turbines,” in *Fundamental and Advanced Topics in Wind Power*, IntechOpen, 2011.

[113] Skill-Lync, “Week 7 - Mini project - Flow over an Airfoil,” *Skill-Lync*. https://skill-lync.com/student-projects/week-7-mini-project-flow-over-an-airfoil-9 (accessed Feb. 27, 2023).

[114] K. Y. Maalawi and M. A. Badr, “A practical approach for selecting optimum wind rotors,” *Renew. Energy*, vol. 28, no. 5, pp. 803–822, 2003.

[115] A. Sullivan, “Aerodynamic forces acting on an airfoil,” *Phys. Dep. Coll. Wooster Ohio USA*, 2010.

[116] I. H. Abbott and A. E. Von Doenhoff, *Theory of wing sections: including a summary of airfoil data*. Courier Corporation, 2012.

[117] M. Drela and H. Youngren, “XFOIL 6.94 user guide.” MIT Aero & Astro, 2001.

[118] D. Marten, J. Wendler, G. Pechlivanoglou, C. N. Nayeri, and C. O. Paschereit, “QBLADE: an open source tool for design and simulation of horizontal and vertical axis wind turbines,” *Int. J. Emerg. Technol. Adv. Eng.*, vol. 3, no. 3, pp. 264–269, 2013.

[119] M. Hansen, *Aerodynamics of wind turbines*. Routledge, 2015.

[120] X. Liu, L. Wang, and X. Tang, “Optimized linearization of chord and twist angle profiles for fixed-pitch fixed-speed wind turbine blades,” *Renew. Energy*, vol. 57, pp. 111–119, 2013.

[121] K. Yang, “Geometry design optimization of a wind turbine blade considering effects on aerodynamic performance by linearization,” *Energies*, vol. 13, no. 9, p. 2320, 2020.

[122] A. Alkhabbaz, H.-S. Yang, A. S. Weerakoon, and Y.-H. Lee, “A novel linearization approach of chord and twist angle distribution for 10 kW horizontal axis wind turbine,” *Renew. Energy*, vol. 178, pp. 1398–1420, 2021.

[123] M. Tahani, G. Kavari, M. Masdari, and M. Mirhosseini, “Aerodynamic design of horizontal axis wind turbine with innovative local linearization of chord and twist distributions,” *Energy*, vol. 131, pp. 78–91, 2017.

[124] M. S. Selig and V. L. Coverstone-Carroll, “Application of a genetic algorithm to wind turbine design,” 1996.

[125] M. A. Yurdusev, R. Ata, and N. S. Çetin, “Assessment of optimum tip speed ratio in wind turbines using artificial neural networks,” *Energy*, vol. 31, no. 12, pp. 2153–2161, 2006.

[126] X. Liu, Y. Chen, and Z. Ye, “Optimization model for rotor blades of horizontal axis wind turbines,” *Front. Mech. Eng. China*, vol. 2, no. 4, pp. 483–488, 2007.

[127] P. Fuglsang and C. Bak, “Development of the Risø wind turbine airfoils,” *Wind Energy*, vol. 7, no. 2, pp. 145–162, 2004, doi: 10.1002/we.117.

[128] R. Van Rooij and W. A. Timmer, “Roughness sensitivity considerations for thick rotor blade airfoils,” *J Sol Energy Eng*, vol. 125, no. 4, pp. 468–478, 2003.

[129] T. Barlas and M. Lackner, “The Application of Smart Structures for Large Wind Turbine Rotor Blades,” in *Proceedings of the Iea Topical Expert Meeting*, Delft University of Technology Delft, The Netherlands, 2006.

[130] A. Ahlström, “Emergency stop simulation using a finite element model developed for large blade deflections,” *Wind Energy Int. J. Prog. Appl. Wind Power Convers. Technol.*, vol. 9, no. 3, pp. 193–210, 2006.

[131] S. M. Habali and I. A. Saleh, “Local design, testing and manufacturing of small mixed airfoil wind turbine blades of glass fiber reinforced plastics: part I: design of the blade and root,” *Energy Convers. Manag.*, vol. 41, no. 3, pp. 249–280, 2000.

[132] P. Brøndsted, H. Lilholt, and A. Lystrup, “Composite materials for wind power turbine blades,” *Annu Rev Mater Res*, vol. 35, pp. 505–538, 2005.

[133] A. S. KS, “STRUCTURAL AND MODAL ANALYSIS OF WIND TURBINE BLADES,” 2021.

[134] U. E. Y. Gómez, Z. J. A. López, R. A. Jimenez, G. V. López, and L. J. J. Villalon, “Design and Manufacturing of Wind Turbine Blades of Low Capacity Using CAD/CAM Techniques and Composite Materials,” *Energy Procedia*, vol. 57, pp. 682–690, 2014, doi: 10.1016/j.egypro.2014.10.223.

[135] M. Adaramola, *Wind Turbine Technology: Principles and Design*. CRC Press, 2014.

[136] P. J. Moriarty and A. C. Hansen, “AeroDyn theory manual,” National Renewable Energy Lab., Golden, CO (US), 2005.

[137] M. M. Shokrieh and R. Rafiee, “Simulation of fatigue failure in a full composite wind turbine blade,” *Compos. Struct.*, vol. 74, no. 3, pp. 332–342, 2006.

[138] W. Y. Liu, B. P. Tang, J. G. Han, X. N. Lu, N. N. Hu, and Z. Z. He, “The structure healthy condition monitoring and fault diagnosis methods in wind turbines: A review,” *Renew. Sustain. Energy Rev.*, vol. 44, pp. 466–472, 2015.

[139] W. Wang, Y. Xue, C. He, and Y. Zhao, “Review of the typical damage and damage-detection methods of large wind turbine blades,” *Energies*, vol. 15, no. 15, p. 5672, 2022.

[140] B. Lu, Y. Li, X. Wu, and Z. Yang, “A review of recent advances in wind turbine condition monitoring and fault diagnosis,” *2009 IEEE Power Electron. Mach. Wind Appl.*, pp. 1–7, 2009.

[141] P. U. Haselbach, R. D. Bitsche, and K. Branner, “The effect of delaminations on local buckling in wind turbine blades,” *Renew. Energy*, vol. 85, pp. 295–305, 2016.

[142] N. N. Davis, Ø. Byrkjedal, A. N. Hahmann, N.-E. Clausen, and M. Žagar, “Ice detection on wind turbines using the observed power curve,” *Wind Energy*, vol. 19, no. 6, pp. 999–1010, 2016.

[143] T. Ackermann and L. Söder, “Wind energy technology and current status: a review,” *Renew. Sustain. Energy Rev.*, vol. 4, no. 4, pp. 315–374, 2000.

[144] W. Qiao and D. Lu, “A survey on wind turbine condition monitoring and fault diagnosis—Part I: Components and subsystems,” *IEEE Trans. Ind. Electron.*, vol. 62, no. 10, pp. 6536–6545, 2015.

[145] W. Qiao and D. Lu, “A survey on wind turbine condition monitoring and fault diagnosis—Part II: Signals and signal processing methods,” *IEEE Trans. Ind. Electron.*, vol. 62, no. 10, pp. 6546–6557, 2015.

[146] G. Fiore and M. S. Selig, “Simulation of damage progression on wind turbine blades subject to particle erosion,” in *54th AIAA Aerospace Sciences Meeting*, 2016, p. 0813.

[147] E. S. Hire, “Non-recyclable wind turbine blades ending up in landfill,” *Expert Skip Hire Sussex*. https://www.expertskiphire.co.uk/wind-turbine-blades-recycling (accessed Oct. 27, 2022).

[148] B. Park, Y.-K. An, and H. Sohn, “Visualization of hidden delamination and debonding in composites through noncontact laser ultrasonic scanning,” *Compos. Sci. Technol.*, vol. 100, pp. 10–18, 2014.

[149] N. Myrent, D. E. Adams, and D. T. Griffith, “Wind turbine blade shear web disbond detection using rotor blade operational sensing and data analysis,” *Philos. Trans. R. Soc. Math. Phys. Eng. Sci.*, vol. 373, no. 2035, p. 20140345, Feb. 2015, doi: 10.1098/rsta.2014.0345.

[150] R. Rafiee and M. R. Hashemi-Taheri, “Failure analysis of a composite wind turbine blade at the adhesive joint of the trailing edge,” *Eng. Fail. Anal.*, vol. 121, p. 105148, 2021.

[151] A. Kling and J. D. Sørensen, “Scale-up of wind turbine blades-changes in failure type,” in *European Wind Energy Conference and Exhibition 2012, EWEC 2012*, 2012, pp. 41–46.

[152] K. Wetzel, “Defect-tolerant structural design of wind turbine blades,” in *50th AIAA/ASME/ASCE/AHS/ASC Structures, Structural Dynamics, and Materials Conference 17th AIAA/ASME/AHS Adaptive Structures Conference 11th AIAA No*, 2009, p. 2409.

[153] R. E. Murray, J. Roadman, and R. Beach, “Fusion joining of thermoplastic composite wind turbine blades: Lap-shear bond characterization,” *Renew. Energy*, vol. 140, pp. 501–512, 2019.

[154] A. Kusiak, Z. Zhang, and A. Verma, “Prediction, operations, and condition monitoring in wind energy,” *Energy*, vol. 60, pp. 1–12, Oct. 2013, doi: 10.1016/j.energy.2013.07.051.

[155] M. Awadallah and A. El-Sinawi, “Effect and detection of cracks on small wind turbine blade vibration using special Kriging analysis of spectral shifts,” *Measurement*, vol. 151, p. 107076, 2020.

[156] Y. Wang, M. Liang, and J. Xiang, “Damage detection method for wind turbine blades based on dynamics analysis and mode shape difference curvature information,” *Mech. Syst. Signal Process.*, vol. 48, no. 1–2, pp. 351–367, 2014.

[157] M. Damiano, A. Russo, A. Sellitto, E. Vecchio, T. Stellato, and A. Riccio, “Design of a composite wind turbine blade manufactured with the ONE SHOT BLADE® technology,” *Mater. Today Proc.*, vol. 34, pp. 103–105, 2021.

[158] A. Sellitto, A. Russo, A. Riccio, and M. Damiano, “Fibreglass wind turbine blades: Damage tolerant design and verification,” in *AIP Conference Proceedings*, AIP Publishing LLC, 2020, p. 020032.

[159] P. J. Schubel, R. J. Crossley, E. K. G. Boateng, and J. R. Hutchinson, “Review of structural health and cure monitoring techniques for large wind turbine blades,” *Renew. Energy*, vol. 51, pp. 113–123, 2013.

[160] J. Wu, C. Song, H. S. Saleem, A. Downey, and S. Laflamme, “Network of flexible capacitive strain gauges for the reconstruction of surface strain,” *Meas. Sci. Technol.*, vol. 26, no. 5, p. 055103, 2015.

[161] S. Tian, Z. Yang, X. Chen, and Y. Xie, “Damage detection based on static strain responses using FBG in a wind turbine blade,” *Sensors*, vol. 15, no. 8, pp. 19992–20005, 2015.

[162] K. Lee, A. Aihara, G. Puntsagdash, T. Kawaguchi, H. Sakamoto, and M. Okuma, “Feasibility study on a strain based deflection monitoring system for wind turbine blades,” *Mech. Syst. Signal Process.*, vol. 82, pp. 117–129, 2017.

[163] M. Naderhirn and P. Langthaler, “Method and system for inspecting a surface area for material defects,” May 19, 2020

[164] J. Yang, C. Peng, J. Xiao, J. Zeng, and Y. Yuan, “Application of videometric technique to deformation measurement for large-scale composite wind turbine blade,” *Appl. Energy*, vol. 98, pp. 292–300, 2012.

[165] B. Yang, L. Zhang, W. Zhang, and Y. Ai, “Non-destructive testing of wind turbine blades using an infrared thermography: A review,” in *2013 International Conference on Materials for Renewable Energy and Environment*, IEEE, 2013, pp. 407–410.

[166] H. F. Zhou, H. Y. Dou, L. Z. Qin, Y. Chen, Y. Q. Ni, and J. M. Ko, “A review of full-scale structural testing of wind turbine blades,” *Renew. Sustain. Energy Rev.*, vol. 33, pp. 177–187, May 2014, doi: 10.1016/j.rser.2014.01.087.

[167] R. Yang, Y. He, A. Mandelis, N. Wang, X. Wu, and S. Huang, “Induction infrared thermography and thermal-wave-radar analysis for imaging inspection and diagnosis of blade composites,” *IEEE Trans. Ind. Inform.*, vol. 14, no. 12, pp. 5637–5647, 2018.

[168] M. Doroshtnasir, T. Worzewski, R. Krankenhagen, and M. Röllig, “On-site inspection of potential defects in wind turbine rotor blades with thermography,” *Wind Energy*, vol. 19, no. 8, pp. 1407–1422, 2016.

[169] R. Raišutis, E. Jasiūnienė, R. Šliteris, and A. Vladišauskas, “The review of non-destructive testing techniques suitable for inspection of the wind turbine blades,” *Ultragarsas/Ultrasound*, vol. 63, no. 2, pp. 26–30, 2008.

[170] H. Alian, S. Konforty, U. Ben-Simon, R. Klein, M. Tur, and J. Bortman, "Bearing fault detection and fault size estimation using fiber-optic sensors," *Mech. Syst. Signal Process.*, vol. 120, pp. 392–407, Apr. 2019, doi: 10.1016/j.ymssp.2018.10.035.

[171] F. P. G. Márquez, A. M. Tobias, J. M. P. Pérez, and M. Papaelias, "Condition monitoring of wind turbines: Techniques and methods," *Renew. Energy*, vol. 46, pp. 169–178, 2012.

[172] Z. Hameed, Y. S. Hong, Y. M. Cho, S. H. Ahn, and C. K. Song, "Condition monitoring and fault detection of wind turbines and related algorithms: A review," *Renew. Sustain. Energy Rev.*, vol. 13, no. 1, pp. 1–39, 2009.

[173] X. W. Ye, Y. H. Su, and J. P. Han, "Structural Health Monitoring of Civil Infrastructure Using Optical Fiber Sensing Technology: A Comprehensive Review," *Sci. World J.*, vol. 2014, p. e652329, Jul. 2014, doi: 10.1155/2014/652329.

[174] J. Wei and J. McCarty, "Acoustic emission evaluation of composite wind turbine blades during fatigue testing," *Wind Eng.*, pp. 266–274, 1993.

[175] A. Nair and C. S. Cai, "Acoustic emission monitoring of bridges: Review and case studies," *Eng. Struct.*, vol. 32, no. 6, pp. 1704–1714, 2010.

[176] B.-H. Han, D.-J. Yoon, Y.-H. Huh, and Y.-S. Lee, "Damage assessment of wind turbine blade under static loading test using acoustic emission," *J. Intell. Mater. Syst. Struct.*, vol. 25, no. 5, pp. 621–630, 2014.

[177] Y. J. Yan, L. Cheng, Z. Y. Wu, and L. H. Yam, "Development in vibration-based structural damage detection technique," *Mech. Syst. Signal Process.*, vol. 21, no. 5, pp. 2198–2211, 2007.

[178] P. Cawley and R. D. Adams, "The location of defects in structures from measurements of natural frequencies," *J. Strain Anal. Eng. Des.*, vol. 14, no. 2, pp. 49–57, 1979.

[179] O. S. Salawu, "Detection of structural damage through changes in frequency: a review," *Eng. Struct.*, vol. 19, no. 9, pp. 718–723, 1997.

[180] B. Fitzgerald, J. Arrigan, and B. Basu, "Damage detection in wind turbine blades using time-frequency analysis of vibration signals," in *The 2010 International Joint Conference on Neural Networks (IJCNN)*, IEEE, 2010, pp. 1–5.

[181] K. Y. Dai and G. R. Liu, "Free and forced vibration analysis using the smoothed finite element method (SFEM)," *J. Sound Vib.*, vol. 301, no. 3–5, pp. 803–820, 2007.

[182] W.-H. Hu, S. Thöns, R. G. Rohrmann, S. Said, and W. Rücker, "Vibration-based structural health monitoring of a wind turbine system Part II: Environmental/operational effects on dynamic properties," *Eng. Struct.*, vol. 89, pp. 273–290, 2015.

[183] H. Sohn, "Effects of environmental and operational variability on structural health monitoring," *Philos. Trans. R. Soc. Math. Phys. Eng. Sci.*, vol. 365, no. 1851, pp. 539–560, 2007.

[184] G. Ye, B. Neal, A. Boot, V. Kappatos, C. Selcuk, and T.-H. Gan, "Development of an ultrasonic NDT system for automated in-situ inspection of wind turbine blades," in *EWSHM-7th European Workshop on Structural Health Monitoring*, 2014.

[185] I. Amenabar, A. Mendikute, A. López-Arraiza, M. Lizaranzu, and J. Aurrekoetxea, "Comparison and analysis of non-destructive testing techniques suitable for delamination inspection in wind turbine blades," *Compos. Part B Eng.*, vol. 42, no. 5, pp. 1298–1305, 2011.

[186] B. Yang and D. Sun, "Testing, inspecting and monitoring technologies for wind turbine blades: A survey," *Renew. Sustain. Energy Rev.*, vol. 22, pp. 515–526, Jun. 2013, doi: 10.1016/j.rser.2012.12.056.

[187] M. A. Rumsey and W. Musial, “Application of infrared thermography nondestructive testing during wind turbine blade tests,” *J Sol Energy Eng*, vol. 123, no. 4, pp. 271–271, 2001.

[188] P. Tchakoua, R. Wamkeue, M. Ouhrouche, F. Slaoui-Hasnaoui, T. A. Tameghe, and G. Ekemb, “Wind turbine condition monitoring: State-of-the-art review, new trends, and future challenges,” *Energies*, vol. 7, no. 4, pp. 2595–2630, 2014.

[189] A. Summers, Q. Wang, N. Brady, and R. Holden, “Investigating the measurement of offshore wind turbine blades using coherent laser radar,” *Robot. Comput.-Integr. Manuf.*, vol. 41, pp. 43–52, 2016.

[190] L. Colone, M. K. Hovgaard, L. Glavind, and R. Brincker, “Mass detection, localization and estimation for wind turbine blades based on statistical pattern recognition,” *Mech. Syst. Signal Process.*, vol. 107, pp. 266–277, 2018.

[191] X. W. Ye, C. Z. Dong, and T. Liu, “A Review of Machine Vision-Based Structural Health Monitoring: Methodologies and Applications,” *J. Sens.*, vol. 2016, p. e7103039, Nov. 2016, doi: 10.1155/2016/7103039.

[192] D. Y. Kim, H.-B. Kim, W. S. Jung, S. Lim, J.-H. Hwang, and C.-W. Park, “Visual testing system for the damaged area detection of wind power plant blade,” in *IEEE ISR 2013*, IEEE, 2013, pp. 1–5.

[193] G. Lloyd and G. Hamburg, “Guideline for the certification of wind turbines,” *July 1st*, 2010.

[194] E. R. Jørgensen, K. K. Borum, M. McGugan, C. L. Thomsen, and F. M. Jensen, “Full scale testing of wind turbine blade to failure - flapwise loading,” p. 31.

[195] F. M. Jensen, A. S. Puri, J. P. Dear, K. Branner, and A. Morris, “Investigating the impact of non-linear geometrical effects on wind turbine blades—Part 1: Current status of design and test methods and future challenges in design optimization,” *Wind Energy*, vol. 14, no. 2, pp. 239–254, 2011.

[196] L. C. T. Overgaard and E. Lund, “Structural collapse of a wind turbine blade. Part B: Progressive interlaminar failure models,” *Compos. Part Appl. Sci. Manuf.*, vol. 41, no. 2, pp. 271–283, Feb. 2010, doi: 10.1016/j.compositesa.2009.10.012.

[197] P. Pratumnopharat, P. S. Leung, and R. S. Court, “Extracting fatigue damage parts from the stress–time history of horizontal axis wind turbine blades,” *Renew. Energy*, vol. 58, pp. 115–126, 2013.

[198] J. C. Marin, A. Barroso, F. Paris, and J. Canas, “Study of damage and repair of blades of a 300 kW wind turbine,” *Energy*, vol. 33, no. 7, pp. 1068–1083, 2008.

[199] J. S. Rajadurai and G. Thanigaiyarasu, “Structural analysis, failure prediction, and cost analysis of alternative material for composite wind turbine blades,” *Mech. Adv. Mater. Struct.*, vol. 16, no. 6, pp. 467–487, 2009.

[200] A. Aihara, T. Kawaguchi, N. Miki, T. Azami, H. Sakamoto, and M. Okuma, “A vibration estimation method for wind turbine blades,” *Exp. Mech.*, vol. 57, pp. 1213–1224, 2017.

[201] M. Ramakrishnan, G. Rajan, Y. Semenova, and G. Farrell, “Overview of fiber optic sensor technologies for strain/temperature sensing applications in composite materials,” *Sensors*, vol. 16, no. 1, p. 99, 2016.

[202] J. Tang, S. Soua, C. Mares, and T.-H. Gan, “A pattern recognition approach to acoustic emission data originating from fatigue of wind turbine blades,” *Sensors*, vol. 17, no. 11, p. 2507, 2017.

[203] W. Zhou, Y. Li, Z. Li, X. Liang, Y. Pang, and F. Wang, “Interlaminar shear properties and acoustic emission monitoring of the delaminated composites for wind turbine blades,” in

Advances in Acoustic Emission Technology: Proceedings of the World Conference on Acoustic Emission–2013, Springer, 2015, pp. 557–566.

[204] Z. Bo, Z. Yanan, and C. Changzheng, “Acoustic emission detection of fatigue cracks in wind turbine blades based on blind deconvolution separation,” *Fatigue Fract. Eng. Mater. Struct.*, vol. 40, no. 6, pp. 959–970, 2017.

[205] K. A. Tiwari and R. Raisutis, “Refinement of defect detection in the contact and non-contact ultrasonic non-destructive testing of wind turbine blade using guided waves,” *Procedia Struct. Integr.*, vol. 13, pp. 1566–1570, 2018.

[206] K. A. Tiwari and R. Raisutis, “Post-processing of ultrasonic signals for the analysis of defects in wind turbine blade using guided waves,” *J. Strain Anal. Eng. Des.*, vol. 53, no. 8, pp. 546–555, 2018.

[207] Q. X. Liu *et al.*, “Research on automatic positioning system of ultrasonic testing of wind turbine blade flaws,” in *IOP Conference Series: Earth and Environmental Science*, IOP Publishing, 2017, p. 012074.

[208] B. Park, H. Sohn, P. Malinowski, and W. Ostachowicz, “Delamination localization in wind turbine blades based on adaptive time-of-flight analysis of noncontact laser ultrasonic signals,” *Nondestruct. Test. Eval.*, vol. 32, no. 1, pp. 1–20, 2017.

[209] A. Ghoshal, M. J. Sundaresan, M. J. Schulz, and P. Frank Pai, “Structural health monitoring techniques for wind turbine blades,” *J. Wind Eng. Ind. Aerodyn.*, vol. 85, no. 3, pp. 309–324, Apr. 2000, doi: 10.1016/S0167-6105(99)00132-4.

[210] G. A. Skrimpas, K. Kleani, N. Mijatovic, C. W. Sweeney, B. B. Jensen, and J. Holboell, “Detection of icing on wind turbine blades by means of vibration and power curve analysis,” *Wind Energy*, vol. 19, no. 10, pp. 1819–1832, 2016.

[211] “Developments in Large Wind Turbine Modal Analysis... - Google 学术搜索.” https://scholar.google.com.hk/scholar?hl=zh-CN&as_sdt=0%2C5&q=Developments+in+Large+Wind+Turbine+Modal+Analysis+Using+Point+Tracking+Videogrammetry&btnG= (accessed Mar. 19, 2023).

[212] “Excitation Methods for a 60 kW Vertical Axis Wind Turbine - Google 学术搜索.” https://scholar.google.com.hk/scholar?hl=zh-CN&as_sdt=0%2C5&q=Excitation+Methods+for+a+60+kW+Vertical+Axis+Wind+Turbine&btnG= (accessed Mar. 19, 2023).

[213] “Analysis of free and forced vibration of a cracked cantilever beam - ScienceDirect.” https://www.sciencedirect.com/science/article/pii/S0963869507000229?casa_token=FPwBSs7gDtMAAAAA:Yb00RTbfP3zqR5o7PvS39PeaT4m9oVQpVxG89ZP61Cz0ihjzlbGbjetiqDAMZ9UDoN9VJqi7QGc8 (accessed Mar. 13, 2023).

[214] B. O. Baba, “Free Vibration Analysis of Curved Sandwich Beams with Face/Core Debond Using Theory and Experiment,” *Mech. Adv. Mater. Struct.*, vol. 19, no. 5, pp. 350–359, Jul. 2012, doi: 10.1080/15376494.2010.528163.

[215] “Abaqus Analysis User’s Guide (2016).” http://130.149.89.49:2080/v2016/books/usb/default.htm (accessed Sep. 03, 2022).

[216] A. F. U. Guide, “Release 14.0, ANSYS,” *Inc USA Novemb.*, 2011.

[217] D. Caous, N. Lavauzelle, J. Valette, and J.-C. Wahl, “Load application method for shell finite element model of wind turbine blade,” *Wind Eng.*, vol. 42, no. 5, pp. 467–482, Oct. 2018, doi: 10.1177/0309524X18759897.

[218] J. C. Berg and B. R. Resor, “Numerical manufacturing and design tool (NuMAD v2.0) for wind turbine blades : user’s guide.,” SAND2012-7028, 1051715, Aug. 2012. doi: 10.2172/1051715.

[219] J. Jonkman, S. Butterfield, W. Musial, and G. Scott, “Definition of a 5-MW Reference Wind Turbine for Offshore System Development,” NREL/TP-500-38060, 947422, Feb. 2009. doi: 10.2172/947422.

[220] J. Tang, X. Chen, and K. Yang, “Evaluating Structural Failure of Load-Carrying Composite Box Beams with Different Geometries and Load Conditions,” *Appl. Compos. Mater.*, vol. 26, no. 4, pp. 1151–1161, Aug. 2019, doi: 10.1007/s10443-019-09776-4.

[221] Y. Hua, A. R. M. Kasavajhala, and L. Gu, “Elastic–plastic analysis and strength evaluation of adhesive joints in wind turbine blades,” *Compos. Part B Eng.*, vol. 44, no. 1, pp. 650–656, Jan. 2013, doi: 10.1016/j.compositesb.2012.02.001.

[222] D. Aikhuele, “Evaluation of Adhesive Materials Used in Wind Turbine Blades,” *Erzincan Üniversitesi Fen Bilim. Enstitüsü Derg.*, Dec. 2019, doi: 10.18185/erzifbed.456945.

[223] J. B. Jørgensen, “Adhesive Joints in Wind Turbine Blades,” 2017, doi: 10.11581/DTU:00000027.

[224] A. Akhavan-Safar, E. A. S. Marques, R. J. C. Carbas, and L. F. M. da Silva, *Cohesive Zone Modelling for Fatigue Life Analysis of Adhesive Joints*. in SpringerBriefs in Applied Sciences and Technology. Cham: Springer International Publishing, 2022. doi: 10.1007/978-3-030-93142-1.

[225] “Standard Practice for Classifying Failure Modes in Fiber-Reinforced-Plastic (FRP) Joints.” https://www.astm.org/d5573-99r19.html (accessed Mar. 17, 2023).

[226] “The science and art of structural adhesive bonding - Google 学术搜索.” https://scholar.google.com.hk/scholar?hl=zh-CN&as_sdt=0%2C5&q=The+science+and+art+of+structural+adhesive+bonding&btnG= (accessed Mar. 17, 2023).

[227] L. F. M. Da Silva, R. D. Campilho, L. F. da Silva, and R. D. Campilho, *Advances in numerical modelling of adhesive joints*. Springer, 2012.

[228] D. C. Noorman, “Cohesive Zone Modelling in Adhesively Bonded Joints,” p. 172.

[229] “M. L. Williams, The stresses around a fault or crack... - Google 学术搜索.” https://scholar.google.com.hk/scholar?hl=zh-CN&as_sdt=0%2C5&q=M.+L.+Williams%2C+The+stresses+around+a+fault+or+crack+in+dissimilar+media.+Bulletin+of+the+Seismological+Society+of+America.+49%2C+199+%281959%29.&btnG= (accessed Mar. 18, 2023).

[230] “S. J. John, A. J. Kinoch, and F. L. Matthews, Measuring... - Google 学术搜索.” https://scholar.google.com.hk/scholar?hl=zh-CN&as_sdt=0%2C5&q=S.+J.+John%2C+A.+J.+Kinoch%2C+and+F.+L.+Matthews%2C+Measuring+and+predicting+the+durability+of+bonded+fibre%2F+epoxy+composite+joints.+Composites.+22%2C+121+%281991%29.&btnG= (accessed Mar. 18, 2023).

[231] “R. D. Adams and J. A. Harris, Strength prediction... - Google 学术搜索.” https://scholar.google.com.hk/scholar?hl=zh-CN&as_sdt=0%2C5&q=R.+D.+Adams+and+J.+A.+Harris%2C+Strength+prediction+of+bonded+single+lap+joints+by+nonlinear+finite+element+methods.+Int.+J.+Adhesion+and+Adhesives.+7%2C+55+%281984%29.&btnG= (accessed Mar. 18, 2023).

[232] X. Zhao, R. D. Adams, and L. F. M. Da Silva, "Single lap joints with rounded adherend corners: experimental results and strength prediction," *J. Adhes. Sci. Technol.*, vol. 25, no. 8, pp. 837–856, 2011.

[233] R. D. Adams, R. D. Adams, J. Comyn, W. C. Wake, and W. C. Wake, *Structural adhesive joints in engineering*. Springer Science & Business Media, 1997.

[234] "A. A. Griffith, The phenomena of rupture and flow... - Google 学术搜索." https://scholar.google.com.hk/scholar?hl=zh-CN&as_sdt=0%2C5&q=A.+A.+Griffith%2C+The+phenomena+of+rupture+and+flow+in+solids.+Philiosophical+Transaction+of+the+Royal+Society+of+London.+221%2C+163+%281921%29.&btnG= (accessed Mar. 18, 2023).

[235] G. R. Irwin, "Analysis of stresses and strains near the end of a crack traversing a plate," 1957.

[236] "Mixed-mode bending method for delamination testing - Google 学术搜索." https://scholar.google.com.hk/scholar?hl=zh-CN&as_sdt=0%2C5&q=Mixed-mode+bending+method+for+delamination+testing&btnG= (accessed Mar. 18, 2023).

[237] "Cohesive zone with continuum damage properties for... - Google 学术搜索." https://scholar.google.com.hk/scholar?hl=zh-CN&as_sdt=0%2C5&q=Cohesive+zone+with+continuum+damage+properties+for+simulation+of+delamination+development+in+fibre+composites+and+failure+of+adhesive+joints&btnG= (accessed Mar. 18, 2023).

[238] "A. A. Wells, Application of fracture mechanics at... - Google 学术搜索." https://scholar.google.com.hk/scholar?hl=zh-CN&as_sdt=0%2C5&q=A.+A.+Wells%2C+Application+of+fracture+mechanics+at+and+beyond+general+yielding.+British+Welding+Research+Association.+%281963%29.&btnG= (accessed Mar. 18, 2023).

[239] D. S. Dugdale, "Yielding of steel sheets containing slits," *J. Mech. Phys. Solids*, vol. 8, no. 2, pp. 100–104, 1960.

[240] "J. R. Rice and G. F. Rosengren, Plane strain deformation... - Google 学术搜索." https://scholar.google.com.hk/scholar?hl=zh-CN&as_sdt=0%2C5&q=J.+R.+Rice+and+G.+F.+Rosengren%2C+Plane+strain+deformation+near+a+crack+tip+in+a+powerlaw+hardening+material.+J.+theMechanics+and+Physics+of+Solids.+16%2C+1+%281968%29.&btnG= (accessed Mar. 18, 2023).

[241] N. Choupani, "Interfacial mixed-mode fracture characterization of adhesively bonded joints," *Int. J. Adhes. Adhes.*, vol. 28, no. 6, pp. 267–282, 2008.

[242] Z. Chen, R. D. Adams, and L. F. Da Silva, "The use of the J-integral vector to analyse adhesive bonds with and without a crack," *Int. J. Adhes. Adhes.*, vol. 31, no. 1, pp. 48–55, 2011.

[243] E. F. Rybicki and M. F. Kanninen, "A finite element calculation of stress intensity factors by a modified crack closure integral," *Eng. Fract. Mech.*, vol. 9, no. 4, pp. 931–938, 1977.

[244] "The virtual crack closure technique: history, approach... - Google 学术搜索." https://scholar.google.com.hk/scholar?hl=zh-CN&as_sdt=0%2C5&q=The+virtual+crack+closure+technique%3A+history%2C+approach+and+applications&btnG= (accessed Mar. 18, 2023).

[245] M. A. Eder and R. D. Bitsche, "Fracture analysis of adhesive joints in wind turbine blades," *Wind Energy*, vol. 18, no. 6, pp. 1007–1022, 2015.

[246] A. Turon Travesa, *Simulation of delamination in composites under quasi-static and fatigue loading using cohesive zone models*. Universitat de Girona, 2006.

[247] O. R. Shah and M. Tarfaoui, "The identification of structurally sensitive zones subject to failure in a wind turbine blade using nodal displacement based finite element sub-modeling," *Renew. Energy*, vol. 87, pp. 168–181, 2016.

[248] R. Krueger, "Virtual crack closure technique: History, approach, and applications," *Appl Mech Rev*, vol. 57, no. 2, pp. 109–143, 2004.

[249] T. Belytschko and T. Black, "Elastic crack growth in finite elements with minimal remeshing," *Int. J. Numer. Methods Eng.*, vol. 45, no. 5, pp. 601–620, 1999.

[250] S. Mohammadi, *Extended finite element method: for fracture analysis of structures*. John Wiley & Sons, 2008.

[251] M. Sabsabi, E. Giner, and F. J. Fuenmayor, "Experimental fatigue testing of a fretting complete contact and numerical life correlation using X-FEM," *Int. J. Fatigue*, vol. 33, no. 6, pp. 811–822, 2011.

[252] Y. Xu and H. Yuan, "Computational analysis of mixed-mode fatigue crack growth in quasi-brittle materials using extended finite element methods," *Eng. Fract. Mech.*, vol. 76, no. 2, pp. 165–181, 2009.

[253] "R. Talreja and C. V. Singh, Damage and Failure of... - Google 学术搜索." https://scholar.google.com.hk/scholar?hl=zh-CN&as_sdt=0,5&q=R.+Talreja+and+C.+V.+Singh,+Damage+and+Failure+of+Composite+Materials.+(Cambridge+University+Press,+2012). (accessed Mar. 18, 2023).

[254] J. L. R. Desmorat and J. Lemaitre, "„Engineering Damage Mechanics"." Springer-Verlag Berlin Heidelberg, 2005.

[255] H. Khoramishad, A. D. Crocombe, K. B. Katnam, and I. A. Ashcroft, "Predicting fatigue damage in adhesively bonded joints using a cohesive zone model," *Int. J. Fatigue*, vol. 32, no. 7, pp. 1146–1158, Jul. 2010, doi: 10.1016/j.ijfatigue.2009.12.013.

[256] M. Elices, G. V. Guinea, J. Gomez, and J. Planas, "The cohesive zone model: advantages, limitations and challenges," *Eng. Fract. Mech.*, vol. 69, no. 2, pp. 137–163, 2002.

[257] H. Ullah, B. Ullah, and V. V. Silberschmidt, "Structural integrity analysis and damage assessment of a long composite wind turbine blade under extreme loading," *Compos. Struct.*, vol. 246, p. 112426, 2020.

[258] Y. Zuo, J. Montesano, and C. V. Singh, "Assessing progressive failure in long wind turbine blades under quasi-static and cyclic loads," *Renew. Energy*, vol. 119, pp. 754–766, 2018.

[259] H. Hosseini-Toudeshky, M. Jahanmardi, and M. S. Goodarzi, "Progressive debonding analysis of composite blade root joint of wind turbines under fatigue loading," *Compos. Struct.*, vol. 120, pp. 417–427, Feb. 2015, doi: 10.1016/j.compstruct.2014.10.025.

[260] M. De Moura and J. P. M. Gonçalves, "Cohesive zone model for high-cycle fatigue of adhesively bonded joints under mode I loading," *Int. J. Solids Struct.*, vol. 51, no. 5, pp. 1123–1131, 2014.

[261] A. Hillerborg, M. Modéer, and P.-E. Petersson, "Analysis of crack formation and crack growth in concrete by means of fracture mechanics and finite elements," *Cem. Concr. Res.*, vol. 6, no. 6, pp. 773–781, 1976.

[262] G. I. Barenblatt, "The mathematical theory of equilibrium cracks in brittle fracture," *Adv. Appl. Mech.*, vol. 7, pp. 55–129, 1962.

[263] N. Chandra, H. Li, C. Shet, and H. Ghonem, "Some issues in the application of cohesive zone models for metal–ceramic interfaces," *Int. J. Solids Struct.*, vol. 39, no. 10, pp. 2827–2855, 2002.

[264] A. Riccio, S. Saputo, A. Raimondo, and A. Sellitto, "Modeling low velocity impact phenomena on composite structures," in *Dynamic Response and Failure of Composite Materials and Structures*, Elsevier, 2017, pp. 129–158.

[265] W. C. Cui, M. R. Wisnom, and M. Jones, "A comparison of failure criteria to predict delamination of unidirectional glass/epoxy specimens waisted through the thickness," *Composites*, vol. 23, no. 3, pp. 158–166, 1992.

[266] M. A. Al-Saawani, A. I. Al-Negheimish, A. K. El-Sayed, and A. M. Alhozaimy, "Finite Element Modeling of Debonding Failures in FRP-Strengthened Concrete Beams Using Cohesive Zone Model," *Polymers*, vol. 14, no. 9, p. 1889, 2022.

[267] J. Chen, E. Ravey, S. Hallett, M. Wisnom, and M. Grassi, "Prediction of delamination in braided composite T-piece specimens," *Compos. Sci. Technol.*, vol. 69, no. 14, pp. 2363–2367, Nov. 2009, doi: 10.1016/j.compscitech.2009.01.027.

[268] Y. Feng, X. Li, and K. E. Gray, "Development of a 3D numerical model for quantifying fluid-driven interface debonding of an injector well," *Int. J. Greenh. Gas Control*, vol. 62, pp. 76–90, 2017.

[269] E. Choi, N. Utui, and H. S. Kim, "Experimental and analytical investigations on debonding of hybrid FRPs for flexural strengthening of RC beams," *Compos. Part B Eng.*, vol. 45, no. 1, pp. 248–256, Feb. 2013, doi: 10.1016/j.compositesb.2012.06.022.

[270] Y. Feng, E. Podnos, and K. E. Gray, "Well Integrity Analysis: 3D Numerical Modeling of Cement Interface Debonding," presented at the 50th U.S. Rock Mechanics/Geomechanics Symposium, OnePetro, Jun. 2016. Accessed: Oct. 18, 2022. [Online]. Available: https://onepetro.org/ARMAUSRMS/proceedings/ARMA16/All-ARMA16/ARMA-2016-246/125326

[271] P. P. Camanho, C. G. Davila, and M. F. De Moura, "Numerical simulation of mixed-mode progressive delamination in composite materials," *J. Compos. Mater.*, vol. 37, no. 16, pp. 1415–1438, 2003.

[272] M. Kenane and M. L. Benzeggagh, "Mixed-mode delamination fracture toughness of unidirectional glass/epoxy composites under fatigue loading," *Compos. Sci. Technol.*, vol. 57, no. 5, pp. 597–605, 1997.

[273] Q. Sun *et al.*, "A combined experimental and computational analysis of failure mechanisms in open-hole cross-ply laminates under flexural loading," *Compos. Part B Eng.*, vol. 215, p. 108803, Jun. 2021, doi: 10.1016/j.compositesb.2021.108803.

[274] M. Pagani and U. Perego, "Explicit dynamics simulation of blade cutting of thin elastoplastic shells using 'directional' cohesive elements in solid-shell finite element models," *Comput. Methods Appl. Mech. Eng.*, vol. 285, pp. 515–541, Mar. 2015, doi: 10.1016/j.cma.2014.11.027.

[275] J. Zhi and T.-E. Tay, "Explicit modeling of matrix cracking and delamination in laminated composites with discontinuous solid-shell elements," *Comput. Methods Appl. Mech. Eng.*, vol. 351, pp. 60–84, Jul. 2019, doi: 10.1016/j.cma.2019.03.041.

[276] X. Xu, D. Wang, M. Zang, and S. Chen, “Development of an intrinsic solid-shell cohesive zone model for impact fracture of windshield laminated glass,” *Int. J. Impact Eng.*, vol. 163, p. 104187, May 2022, doi: 10.1016/j.ijimpeng.2022.104187.

[277] X. Xu, S. Chen, D. Wang, and M. Zang, “An efficient solid-shell cohesive zone model for impact fracture analysis of laminated glass,” *Theor. Appl. Fract. Mech.*, vol. 108, p. 102660, Aug. 2020, doi: 10.1016/j.tafmec.2020.102660.

[278] A. J. Herrema, J. Kiendl, and M.-C. Hsu, “A framework for isogeometric-analysis-based design and optimization of wind turbine blade structures,” p. 19.

[279] A. J. Herrema, N. M. Wiese, C. N. Darling, B. Ganapathysubramanian, A. Krishnamurthy, and M.-C. Hsu, “A framework for parametric design optimization using isogeometric analysis,” *Comput. Methods Appl. Mech. Eng.*, vol. 316, pp. 944–965, Apr. 2017, doi: 10.1016/j.cma.2016.10.048.

[280] “(PDF) QBlade Guidelines v0.9.” https://www.researchgate.net/publication/280097378_QBlade_Guidelines_v09 (accessed Sep. 05, 2022).

[281] W. Miao, C. Li, Y. Wang, B. Xiang, Q. Liu, and Y. Deng, “Study of adaptive blades in extreme environment using fluid–structure interaction method,” *J. Fluids Struct.*, vol. 91, p. 102734, Nov. 2019, doi: 10.1016/j.jfluidstructs.2019.102734.

[282] L. Gu, A. R. M. Kasavajhala, and S. Zhao, “Finite element analysis of cracks in aging aircraft structures with bonded composite-patch repairs,” *Compos. Part B Eng.*, vol. 42, no. 3, pp. 505–510, Apr. 2011, doi: 10.1016/j.compositesb.2010.11.014.

[283] O. Rajad, M. Hamid, S. ed-Dîn Fertahi, and A. E. Marjani, “Fiber Orientation Effect on the Behavior of the Composite Materials of the Horizontal Axis Wind Turbine Blade (HAWTB),” in *2018 6th International Renewable and Sustainable Energy Conference (IRSEC)*, 2018, pp. 1–6. doi: 10.1109/IRSEC.2018.8702930.

[284] K. Cox and A. Echtermeyer, “Effects of composite fiber orientation on wind turbine blade buckling resistance: Composite fiber orientation on blade buckling resistance,” *Wind Energy*, vol. 17, no. 12, pp. 1925–1943, Dec. 2014, doi: 10.1002/we.1681.

[285] C. Berggreen, K. Branner, J. F. Jensen, and J. P. Schultz, “Application and Analysis of Sandwich Elements in the Primary Structure of Large Wind Turbine Blades,” *J. Sandw. Struct. Mater.*, vol. 9, no. 6, pp. 525–552, Nov. 2007, doi: 10.1177/1099636207069071.

[286] N. Buckney, S. Green, A. Pirrera, and P. M. Weaver, “On the structural topology of wind turbine blades,” *Wind Energy*, vol. 16, no. 4, pp. 545–560, 2013, doi: 10.1002/we.1504.

[287] D. Wu, “The Effect of Blade Aeroelasticity and Turbine Parameters on Wind Turbine Noise,” PhD Thesis, Virginia Tech, 2017.

[288] D. Systemes, “ABAQUS/CAE user’s guide,” *Dassault Syst. Simulia Corp Provid. RI USA*, 2014.

[289] “FAST user guide.pdf.”

[290] Z. Song and C. Su, “Computation of Rayleigh Damping Coefficients for the Seismic Analysis of a Hydro-Powerhouse,” *Shock Vib.*, vol. 2017, pp. 1–11, 2017, doi: 10.1155/2017/2046345.

[291] M. A. Asareh and I. Prowell, “A Simplified Approach for Implicitly Considering Aerodynamics in the Seismic Response of Utility Scale Wind Turbines,” in *53rd AIAA/ASME/ASCE/AHS/ASC Structures, Structural Dynamics and Materials Conference
20th AIAA/ASME/AHS Adaptive Structures*

*Conference
14th AIAA*, Honolulu, Hawaii: American Institute of Aeronautics and Astronautics, Apr. 2012. doi: 10.2514/6.2012-1829.

[292] "Open System for Earthquake Engineering Simulation - Home Page." https://opensees.berkeley.edu/ (accessed Sep. 07, 2022).

[293] A. Labib, D. Kennedy, and C. Featherston, "Free vibration analysis of beams and frames with multiple cracks for damage detection," *J. Sound Vib.*, vol. 333, no. 20, pp. 4991–5003, 2014.

[294] Z. A. Jassim, N. N. Ali, F. Mustapha, and N. A. Jalil, "A review on the vibration analysis for a damage occurrence of a cantilever beam," *Eng. Fail. Anal.*, vol. 31, pp. 442–461, 2013.

[295] H. Hu, B.-T. Wang, C.-H. Lee, and J.-S. Su, "Damage detection of surface cracks in composite laminates using modal analysis and strain energy method," *Compos. Struct.*, vol. 74, no. 4, pp. 399–405, 2006.

[296] F.-L. Zhang, Y.-C. Ni, S.-K. Au, and H.-F. Lam, "Fast Bayesian approach for modal identification using free vibration data, Part I–Most probable value," *Mech. Syst. Signal Process.*, vol. 70, pp. 209–220, 2016.

[297] W. L. Li, "Free vibrations of beams with general boundary conditions," *J. Sound Vib.*, vol. 237, no. 4, pp. 709–725, 2000.

[298] T. Itoh, "Damped vibration mode superposition method for dynamic response analysis," *Earthq. Eng. Struct. Dyn.*, vol. 2, no. 1, pp. 47–57, 1973.

[299] F. Magalhães, E. Caetano, Á. Cunha, O. Flamand, and G. Grillaud, "Ambient and free vibration tests of the Millau Viaduct: Evaluation of alternative processing strategies," *Eng. Struct.*, vol. 45, pp. 372–384, 2012.

[300] K. S. Kumar, I. Siva, P. Jeyaraj, J. W. Jappes, S. C. Amico, and N. Rajini, "Synergy of fiber length and content on free vibration and damping behavior of natural fiber reinforced polyester composite beams," *Mater. Des. 1980-2015*, vol. 56, pp. 379–386, 2014.

[301] G. C. Larsen, M. H. Hansen, A. Baumgart, and I. Carlen, "Modal analysis of wind turbine blades," Feb. 2002, Accessed: Dec. 19, 2022. [Online]. Available: https://www.osti.gov/etdeweb/biblio/20303832